ANALYTICAL AND NUMERICAL SOLUTIONS FOR THE CASE OF A HORIZONTAL WELL WITH A RADIAL POWER-LAW PERMEABILITY DISTRIBUTION—COMPARISON TO THE MULTI-FRACTURE HORIZONTAL WELL CASE

A Thesis

by

RYAN SAWYER BROUSSARD

Submitted to the Office of Graduate Studies of
Texas A&M University
in partial fulfillment of the requirements for the degree of

MASTER OF SCIENCE

Approved by:

Chair of Committee,	Thomas A. Blasingame
Co-Chair of Committee,	George J. Moridis
Committee Members,	Eduardo Gildin
	Andreas Kronenberg
	Peter P. Valko
Head of Department,	A. Daniel Hill

May 2013

Major Subject: Petroleum Engineering

ABSTRACT

In this work, I present the development of analytical solutions in the Laplace domain for a fully-penetrating, horizontal well producing at a constant flow rate or constant wellbore pressure in the center of a composite, cylindrical reservoir system with an impermeable outer boundary. The composite reservoir consists of two regions. The cylindrical region closest to the wellbore is stimulated, and the permeability within this region follows a power-law function of the radial distance from the wellbore. The unstimulated outer region has homogeneous reservoir properties.

The current norm for successful stimulation of low permeability reservoir rocks is multi-stage hydraulic fracturing. The process of hydraulic fracturing creates thin, high permeability fractures that propagate deep into the reservoir, increasing the area of the rock matrix that is exposed to this low-resistance flow pathway. The large surface area of the high conductivity fracture is what makes hydraulic fracturing so successful. Unfortunately, hydraulic fracturing is often encumbered by problems such as high capital costs and a need for large volumes of water. Therefore, I investigate a new stimulation concept based upon the alteration of the permeability of a large volume around the producing well assembly from its original regime to that following a power-law function. I evaluate the effectiveness of the new concept by comparing it to conventional multi-stage hydraulic fracturing.

The results of this investigation show that the power-law permeability reservoir (PPR) has a performance advantage over the multi-fractured horizontal treatment (MFH) only when the fracture conductivity and fracture half-length are small. Most importantly, the results demonstrate that the PPR can provide respectable flow rates and recovery factors, thus making it a viable stimulation concept for ultra-low permeability reservoirs, especially under conditions that may not be conducive to a conventional MHF treatment.

DEDICATION

This thesis is dedicated to my mother and father for their unconditional love and support.

If you can't explain something simply, you don't understand it well.

— *Albert Einstein*

ACKNOWLEDGEMENTS

I would like to thank Dr. Tom Blasingame for his mentorship, his encouragement and demand for perfection. I will always have the upmost respect for him. I thank Dr. George Moridis for his willingness to dedicate so much time for my benefit and his words of encouragement. I have learned so much from him and have gained tremendous confidence in myself because of him. I thank Dr. Peter Valko for his assistance with my research and being an excellent educator during both my undergraduate and graduate careers. I really enjoyed his classes. I thank Dr. Eduardo Gildin for being an excellent educator and for serving on my committee. I thank Dr. Andreas Kronenberg for serving on my committee. I thank Dr. Maria Barrufet for acting as substitute during my thesis defense and being an excellent educator.

TABLE OF CONTENTS

LIST OF FIGURES

FIGURE Page

FIGURE Page

FIGURE Page

LIST OF TABLES

1. INTRODUCTION

1.1 Statement of the Problem

Unconventional plays (e.g., shale, tight sands, and coalbeds) contain vast volumes of hydrocarbon resources. Shale plays alone are estimated to contain 500 to 1,000 Trillion cubic feet (Tcf) of recoverable reserves of natural gas (Arthur et al. 2008). Until the 1990's, these hydrocarbon resources remained locked and unattainable beneath the surface, confined by the low permeability rock matrix and a lack of natural fracture networks that precluded recovery using conventional methods. The advent of hydraulic fracturing, coupled with advances in horizontal drilling, unlocked this vital energy resource, achieving economical flow rates in low and ultra-low permeability rock media. In fact, as a direct result of applying hydraulic fracturing and horizontal drilling technologies, U.S. proved reserves have risen from 166.474 Tcf of natural gas and 22.017 billion barrels of crude oil in 1996 to 304.625 Tcf of natural gas and 23.267 billion barrels of crude oil in 2010 (US EIA 2012).

The tremendous success of hydraulic fracturing as an effective means of stimulating low permeability reservoirs does not come without significant drawbacks. First, hydraulic fracturing is expensive. For a typical Marcellus shale well, hydraulic fracturing can constitute one third of the entire well's drilling and completion costs (Hefley et al. 2011). Second, the process of hydraulic fracturing requires billions of gallons of water, which is often a limited and valuable resource. The EPA estimates that 35,000 wells are hydraulically fractured each year in the U.S. (ORD 2011). If a majority of these wells are horizontal, the annual water requirements could range from 70 to 140 billion gallons, which is equivalent to the annual water use of one or two cities with populations of over 2.5 million people (ORD 2011).

Consequently, industry and academia have been evaluating less expensive and more water conservative stimulation techniques, such as the slot-drill technique proposed by Carter (2009) or the Repeated Electro Dynamic Stimulation (REDStim) method currently being investigated by researchers at Texas Tech University (TTU 2011). In this thesis, I do not present a new, alternative stimulation technique that will rival the success of hydraulic fracturing or that will cost less, or that will use less water. Rather, I solve

analytically and assess an alternative stimulation *concept* or stimulation *outcome* that has not yet been attempted or realized in the field. This new concept presumes the technology exists (or will exist) to create an extensive altered permeability zone that follows a power-law function of the radial distance from a horizontal wellbore. I do not suggest any mechanism that might create a power-law permeability distribution. My primary goal is to evaluate the performance of this conceptual approach in low permeability reservoirs by comparing its productivity to that corresponding to the current stimulation practice (i.e. hydraulic fracturing).

1.2 Research Objectives

The focus of my work is the study of a composite, cylindrical reservoir with a horizontal well at its center, and with a power-law permeability distribution in the inner cylindrical subdomain (i.e., the altered permeability zone or stimulated zone) that surrounds the well. Such a reservoir will be hereafter referred to as a PPR (Power-law Permeability Reservoir). The primary objectives of this work are:

- To develop an analytical expression describing the spatial and temporal distribution of pressure in a PPR with the horizontal well at its center producing at a constant flow rate.
- To develop an analytical equation describing the rate behavior in time for a PPR with the horizontal well producing at a constant bottom-hole pressure.
- To validate the analytical solutions by comparing their results to numerical simulation predictions.
- To compare the productivity of a PPR to that of a reservoir stimulated by multiple vertical fractures along a horizontal wellbore.

2. LITERATURE REVIEW

2.1 Cylindrical Composite Model

The term, cylindrical composite reservoir, describes a cylindrical reservoir volume comprised of multiple concentric "rings". Each "ring" defines a "zone" (or "region") with physical properties (i.e., fluid and/or rock properties) different than those of the adjacent volume(s) (**Fig. 2.1**).

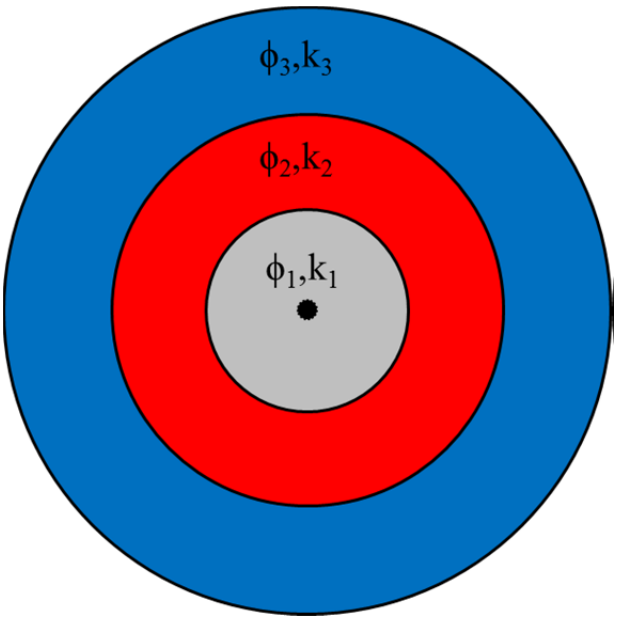

Figure 2.1 — Radial composite reservoir

A homogeneous, isotropic model can rarely (if ever) adequately represent natural reservoirs. Natural heterogeneities may exist because of the vagaries of the depositional environment or from the variability of diagenetic processes. They may also result from the interference of drilling and production operations (e.g., drilling fluid invasion, the injection of fluids during enhanced oil recovery processes or the precipitation of condensates in gas condensate reservoirs).

The cylindrical composite models were developed to describe radial heterogeneities created by well-related operations, including damaging (e.g., drilling fluid invasion) and stimulating (e.g., matrix

acidizing) processes. One of the first solutions was presented by Hurst (1960), who considered an infinite reservoir composed of two sands in series with different peremabilities as part of an interference study between two oil fields. Mortada (1960), also interested in the interference between oil fields, presented an analytical solution for a similar reservoir system, but avoided the point-source limitation. Loucks and Guerrero (1961) studied a two-zone infinite reservoir, anticipating that an understanding of the pressure drop behavior in composite reservoirs would assist in the interpretation of some pressure build-up curves that deviated from homogenous reservoir solutions. Carter (1966) focused on solutions for a finite cylindrical composite reservoir. He also sought to develop solutions that could help explain the abnormal behavior of some pressure transients, and expected his results to be particularly useful in the interpretation of reservoir limit tests. Satman et al. (1980) developed a solution for a two-zone cylindrical composite reservoir with different permeabilities, porosities, and fluid compressibilities in the two regions. Their study focused on the analysis of the characteristics of injection/falloff tests to detect the swept volume during thermal oil recovery processes (e.g., in-situ combustion and steam injection).

All of the analytical solutions mentioned thus far utilize the Laplace transform method. It is the most common approach found in the literature to solve cylindrical composite systems. The method produces rigorous analytical solutions in the Laplace domain but is based on the assumption of linear or linearized processes and requires numerical inversion to obtain solutions in the time domain. Given today's computing capabilities, the numerical inversion is relatively easy to compute. Although there are approaches that do not use the Laplace transform, such as the numerical approach utilized by Bixel and Van Poolen (1967) and the approximate analytical approach presented by Ramey (1970), and thus avoid complex Bessel functions (often found in Laplace transform solutions to radial flow problems) and Laplace space inversion, the availability of literature using the Laplace transform method and the rigorousness of the solutions make it ideal for this work.

2.2 Permeability Distributions

Several studies have considered cylindrical composite models with homogeneous, isotropic properties within each region. In this study, I examine a two-zone cylindrical composite model with a variable

permeability distribution in the inner region and constant properties in the outer region. Therefore, I present literature that also focused on systems (though not all composite systems) with variable permeability distributions that are directly relevant to this work, and perhaps useful for later studies.

Zhang et al. (2006) and Mursal (2002) investigated power-law permeability distributions in an infinite cylindrical composite system and a single cylindrical finite volume, respectively. Both studies explored means to improve well test analysis for a well surrounded by an altered permeability zone. Their power-law permeability distribution in the altered zone is similar to what I present in this work and is given by:

$$k_r(r) = k_w\left[\frac{r}{r_w}\right]^n \quad \text{.....(2.1)}$$

k_r (md) is the reservoir permeability as a function of radial distance, r (ft). k_w (md) is the permeability at the wellbore radius, r_w (ft). n is the power-law exponent. In the Zhang et al. (2006) study, Eq. 2.1 applies only to the inner region. In the infinite outer region, the permeability is constant. This permeability model permits a significant permeability discontinuity at the interface between the two regions. My power-law model constrains the permeability to exactly equal the original reservoir permeability at the interface, and unlike Mursal (2002), the distribution does not extend to the edge of the reservoir but only to the edge of the stimulated region. Because of the similarity in permeability distributions, boundary conditions, and Laplace transform approach, Mursal (2002) provided an excellent resource for the derivation and organization of my solution.

El-Khatib (2009) used an inverse-square permeability distribution (i.e., with the permeability proportional to the inverse of the square of radial distance from the wellbore) for the inner region that would avoid a discontinuity across the interface in a finite cylindrical composite model. This permeability model is described as follows:

$$k_{rD}(r_D) = a - \frac{b}{r_D^2} \quad \text{.....(2.2)}$$

a and b are dimensionless constants defined by the permeability ratio and depth of invasion, and k_{rD} is the dimensionless permeability as a function of the dimensionless radius, r_D. This choice of permeability

model was also guided by the fact that it permits an analytical solution in the Laplace domain, in addition to appropriately describing the formation alteration caused by the invasion of drilling fluids and particles. El-Khatib (2009) applied the solution to examine the effect of the permeability ratio (of the altered permeability at the wellbore to the original reservoir permeability), depth of invasion and reservoir size on the pressure response.

Wilson (2003) used a variable permeability model to predict the spatial and temporal gas permeability behavior in a gas condensate reservoir. Liquid condensates precipitate as a result of the pressure drop close to the wellbore, forming a "condensate bank" that reduces the effective permeability. His permeability distribution is given by:

$$k(r,t) = k_{\min} + (k_{\max} - k_{\min})\left[1 - \exp\left[\frac{-1}{\alpha}\frac{r^2}{t}\right]\right] \quad \text{.....(2.3)}$$

k (md) is the reservoir permeability as a function of time, t (s), and radial distance, r (ft); α ((cp-psi^{-1})/md) is an empirical constant related to the reservoir fluid and rock properties; k_{min} (md) is the minimum effective permeability to gas (or the permeability at the wellbore), and k_{max} (md) is the maximum effective permeability to gas. Wilson (2003) does not utilize a radial composite model. His solution domain involves an infinite reservoir volume, the permeability of which increases exponentially from the wellbore permeability k_{min} to a constant value, k_{max}, at infinity. Wilson (2003) used the Boltzmann transformation to develop an analytical solution, eliminating the need to develop Laplace-space solutions that would need numerical inversion. Nevertheless, the "pressure" form of his solution cannot be resolved as a closed form solution and requires numerical evaluation.

2.3 Hydraulic Fracturing Stimulation Concept

In this section, I briefly review the hydraulic fracturing stimulation concept, to which I will be comparing the power-law permeability stimulation concept. Hydraulic fracture treatments involve pumping large volumes of fluids (liquids) at high rates and pressures into the formation at specific predetermined locations along the wellbore. These fluids are often water-based, usually consisting of a gelling agent, a proppant at an appropriate (carefully designed) concentration, and various other additives like friction

reducers, gel breakers, biocides, oxygen scavengers and other stabilizers. The high pressure of the fracturing fluid "breaks down" the formation at the perforations, creating fractures that propagate outward until its energy is depleted. The gelling of the fracturing fluid allows the proppant to remain suspended for efficient transport into the created fracture. Natural tectonic forces tend to force the fracture to close, but the proppant is designed to withstand the stress and keep the fracture open (Freeman 2010). The final result is a large area of the low-permeability rock matrix exposed to a high conductivity pathway that leads directly to the wellbore.

If the horizontal wellbore is drilled parallel to the least principal tectonic stress direction, and is sufficiently deep so that the greatest principal tectonic stress is in the vertical direction, then a vertical fracture will propagate perpendicular to the wellbore (Freeman 2010). In reality, hydraulically-induced fractures in MHF treatments are likely to have the irregular shape and geometry shown in the simulation-derived figure in **Fig. 2.2**; however, in my simulations (see SECTION 4) I use a simple disk (circular) geometry to represent the fractures.

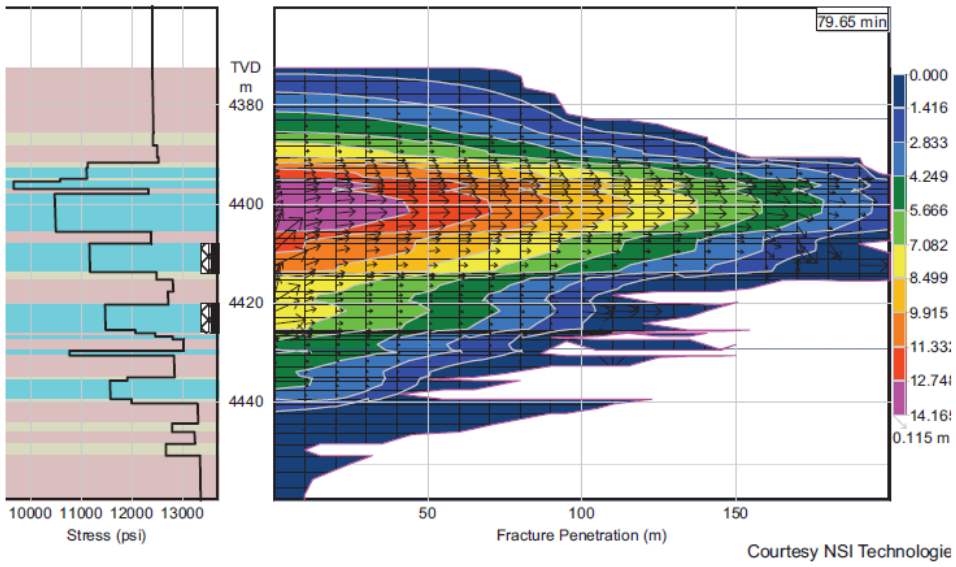

Figure 2.2 — Fracture geometry created by a fully-gridded finite element simulation (Montgomery and Smith 2010)

Repeating the fracturing process in stages along the horizontal length of the wellbore creates what is called a "multiple-fractured horizontal well" (**Fig. 2.3**). This is the stimulation practice that the industry employs in ultra-low permeability reservoirs, and is the standard to which I will compare the power-law permeability stimulation concept.

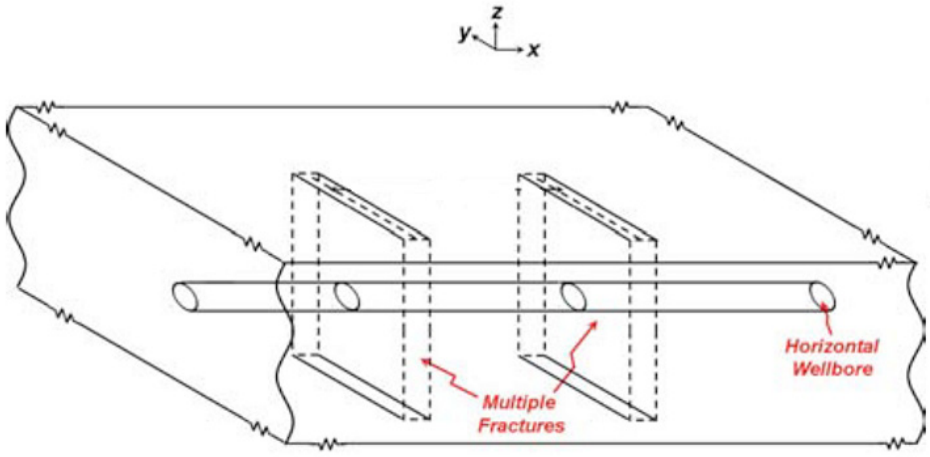

Figure 2.3 — Diagram of multiple-fractured horizontal wellbore (Freeman 2010)

3. DEVELOPMENT OF THE PRESSURE AND RATE SOLUTIONS

3.1 The Concept of the Power-Law Permeability System

I chose the "power-law" permeability distribution to represent this new conceptual stimulation approach because this type of profile seems feasible given that hydraulic, sonic, or electromagnetic pulse energy would be expended mostly near the wellbore. I could also expect this kind of distribution from chemical alteration such as the injection of acid, but I recognize that acidizing would not be viable for such a long exposure as an impractically large volume of acid would be required to substantially alter the native state permeability in a shale. I believe that the "power-law" permeability distribution should be the most conservative permeability profile (i.e., the permeability declines very quickly from the maximum permeability at the wellbore) that can be achieved by hydraulic, mechanical, or chemical mechanisms. Consequently, I assume a stimulation process that alters the original reservoir permeability so that the resulting permeability distribution follows a power-law function of radial distance from a horizontal wellbore. Mathematically, the permeability distribution is expressed as:

$$k_r(r) = k_o\left[\frac{r}{r_s}\right]^n \quad \text{.....(3.1)}$$

k_o (md) is the original reservoir permeability; r_s (ft) is the stimulation zone radius and n is the dimensionless power-law exponent that controls how quickly the permeability declines from the wellbore. The stimulated volume spans the entire length of the horizontal wellbore, and its inner boundary is defined by r_s. Outside the stimulated zone, the permeability is constant and equal to k_o. The reservoir has a finite cylindrical volume defined by the reservoir radius, r_e (ft) and by the wellbore length, L_w (ft) in the z-direction. It is represented by the two-zone cylindrical composite model depicted in **Fig. 3.1**.

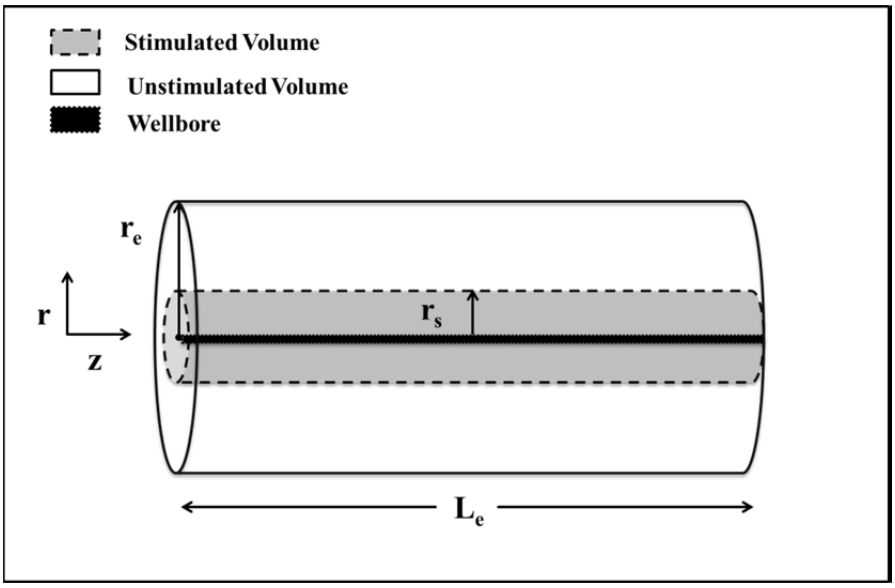

Figure 3.1 — The physical model

Fig. 3.1 shows that the reservoir length coincides with the wellbore length. Although in reality this is rarely, if ever the case, this simplification reduces the problem to a single dimension (the radial direction).

To repeat, at the risk of redundancy, I am comparing two stimulation approaches. The first stimulation approach is at the conceptual stage, and revolves around the idea of altering the permeability of a cylindrical subdomain of rock with a significant volume. I assume that the permeability declines with distance in a power-law manner from its highest level at the wellbore (the center of the stimulated region) to its lowest level (i.e., the original reservoir permeability at some radial distance from the wellbore). The second stimulation approach is the standard practice of multi-stage hydraulic fracturing.

3.2 Development of the Analytical Solutions in the Laplace Domain

In this section I first derive the Laplace space analytical solution of spatial pressure distribution in the composite domain depicted in Fig. 3.1. Then, using the Van Everdingen and Hurst (1949) relationship between constant rate and constant pressure solutions, I derive analytical expressions for the rate and cumulative production in the Laplace domain.

3.2.1 Development of the Pressure Solution in the Laplace Domain

The equations governing fluid flow in the two porous media of the cylindrical composite system are the well-known diffusivity equations. A detailed derivation of the diffusivity equations in dimensionless form is given in Appendix A. The equations for these two regions are:

- Stimulated Zone

$$\frac{1}{r_{sD}^{n}}\frac{1}{r_D}\frac{\partial}{\partial r_D}\left[r_D^{n+1}\frac{\partial p_{D1}}{\partial r_D}\right]=\frac{\partial p_{D1}}{\partial t_D},\quad 1\le r_D<r_{sD} \qquad (3.2)$$

- Unstimulated Zone

$$\frac{1}{r_D}\frac{\partial}{\partial r_D}\left[r_D\frac{\partial p_{D2}}{\partial r_D}\right]=\frac{\partial p_{D2}}{\partial t_D},\quad r_{sD}\le r_D\le r_{eD} \qquad (3.3)$$

Where subscripts 1 and 2 denote the stimulated zone and unstimulated zone respectively. r_D is the dimensionless radius; r_{sD} is the dimensionless stimulation radius; r_{eD} is the dimensionless reservoir radius; t_D is the dimensionless time and p_D is the dimensionless pressure. All dimensionless variables in Eqs. 3.2 and 3.3 are defined by the following expressions:

$$r_D=\frac{r}{r_w} \qquad (3.4)$$

$$r_{sD}=\frac{r_s}{r_w} \qquad (3.5)$$

$$r_{eD}=\frac{r_e}{r_w} \qquad (3.6)$$

$$p_D=2\pi\frac{k_o L_e}{qB\mu}\left(p_i-p\right) \qquad (3.7)$$

$$t_D=\frac{k_o t}{\phi\mu c_t r_w^2} \qquad (3.8)$$

r_w (ft) is the wellbore radius; r_e (ft) is the reservoir radius; L_e (ft) is the length of the reservoir (equivalent to the wellbore length in this case); q (bbl/day) is the liquid flow rate; B (RB/STB) is the liquid formation volume factor; μ (cp) is the liquid viscosity; ϕ (fraction) is the formation porosity; c_t (1/psi) is the total compressibility; p (psi) is the reservoir pressure, and p_i (psi) is the initial reservoir pressure. The power-

law permeability function can also be rewritten in dimensionless form. First, I define the dimensionless permeability as:

$$k_D = \frac{k_r}{k_o} \quad \text{.....(3.9)}$$

k_D is the dimensionless permeability. Then, replacing r, r_s and k_r in the power-law permeability function (Eq. 3.1) with their dimensionless forms (Eqs. 3.4, 3.5 and 3.9 respectively) gives the following dimensionless expression:

$$k_D = \left[\frac{r_D}{r_{sD}}\right]^n \quad \text{.....(3.10)}$$

The derivation of Eqs. 3.2 and 3.3 involved the following significant assumptions:

- The liquid is slightly compressible
- There is only single-phase Darcy flow
- The formation porosity and liquid viscosity are constant
- Gravity effects are neglected
- The horizontal wellbore penetrates and produces along the entire length of the reservoir (radial flow only)

The outer boundaries of the reservoir are all impermeable, and the well produces at a constant rate. The pressure before the onset of production ($t_D=0$) in the stimulated and unstimulated volume is uniform. Additionally, the pressure and flux across the interface between the stimulated and unstimulated volumes are continuous at all times. A detailed derivation of the initial and boundary conditions in dimensionless form is given in Appendix A. Mathematically, the aforementioned boundary and initial conditions are represented by the following equations:

- Initial Conditions (uniform pressure at time zero)

$$p_{D1}(r_D, t_D)\big|_{t_D=0} = p_{D2}(r_D, t_D)\big|_{t_D=0} = 0 \quad \text{.....(3.11)}$$

- Outer Boundary Condition (no-flow outer boundary)

$$\left[r_D \frac{\partial p_{D2}}{\partial r_D} \right]_{r_D = r_{eD}} = 0 \quad \text{..... (3.12)}$$

- Inner Boundary Condition (constant flow rate)

$$\left[r_D \frac{\partial p_{D1}}{\partial r_D} \right]_{r_D = 1} = -r_{sD}^{n} \quad \text{..... (3.13)}$$

- Interface Condition (continuous pressure across the interface)

$$\left[p_{D1} \right]_{r_D = r_{sD}} = \left[p_{D2} \right]_{r_D = r_{sD}} \quad \text{..... (3.14)}$$

- Interface Condition (continuous flux across the interface)

$$\left[\frac{\partial p_{D1}}{\partial r_D} \right]_{r_D = r_{sD}} = \left[\frac{\partial p_{D2}}{\partial r_D} \right]_{r_D = r_{sD}} \quad \text{..... (3.15)}$$

Transforming the dimensionless diffusivity equations into the Laplace domain and inserting the initial condition, Eq. 3.11, into the transformed Eqs. 3.2 and 3.3 gives:

- Stimulated Zone

$$\frac{1}{r_{sD}^{n}} \frac{1}{r_D} \frac{\partial}{\partial r_D} \left[r_D^{n+1} \frac{d\bar{p}_{D1}}{dr_D} \right] = s\bar{p}_{D1} \quad \text{..... (3.16)}$$

- Unstimulated Zone

$$\frac{1}{r_D} \frac{\partial}{\partial r_D} \left[r_D \frac{d\bar{p}_{D2}}{dr_D} \right] = s\bar{p}_{D2} \quad \text{..... (3.17)}$$

s is the Laplace transform variable and $\bar{p}_D$ represents p_D in the Laplace domain. Then, transforming the boundary conditions into the Laplace domain (see derivation details in Appendix A) yields:

- Outer Boundary Condition (no flow outer boundary)

$$\left[r_D \frac{\partial \bar{p}_{D2}}{\partial r_D} \right]_{r_D = r_{eD}} = 0 \quad \text{..... (3.18)}$$

- Inner Boundary Condition (constant flowrate)

$$\left[r_D \frac{\partial \bar{p}_{D1}}{\partial r_D} \right]_{r_D=1} = -\frac{r_{sD}^n}{s} \quad \text{..... (3.19)}$$

- Interface Condition (continuous pressure across the interface)

$$\left[\bar{p}_{D1} \right]_{r_D=r_{sD}} = \left[\bar{p}_{D2} \right]_{r_D=r_{sD}} \quad \text{..... (3.20)}$$

- Interface Condition (continuous flux across the interface)

$$\left[\frac{\partial \bar{p}_{D1}}{\partial r_D} \right]_{r_D=r_{sD}} = \left[\frac{\partial \bar{p}_{D2}}{\partial r_D} \right]_{r_D=r_{sD}} \quad \text{..... (3.21)}$$

Expansion of the radial partial derivative term in Eq. 3.16 with some additional rearrangement results in a Bessel differential equation (derivation details in Appendix A) :

- Stimulated Zone

$$r_D^2 \frac{d^2 \bar{p}_{D1}}{dr_D^2} + (n+1) r_D \frac{d\bar{p}_{D1}}{dr_D} = \frac{r_{sD}^n}{r_D^{n-2}} s \bar{p}_{D1} \quad \text{..... (3.22)}$$

The general solution of which was provided by Bowman (1958).

- Stimulated Zone

$$\bar{p}_{D1} = \frac{1}{s^{3/2}} \sqrt{\frac{r_{sD}^n}{r_D^n}} \left[c_1 I_{\frac{n}{n-2}} \left[\frac{-2 r_D^{\frac{2-n}{2}} \sqrt{s r_{sD}^n}}{n-2} \right] + c_2 I_{\frac{-n}{n-2}} \left[\frac{-2 r_D^{\frac{2-n}{2}} \sqrt{s r_{sD}^n}}{n-2} \right] \right] \quad \text{..... (3.23)}$$

$I_{n/(n-2)}$ is the modified Bessel function of the first kind of order (n/(n-2)) and c_1 and c_2 are two unknown, dimensionless constants. The general solution to Eq. 3.17 is well known (Van Everdingen and Hurst 1949) and given by:

- Unstimulated Zone

$$\bar{p}_{D2} = \frac{1}{s^{3/2}} \left[c_3 I_0 \left[\sqrt{s} r_D \right] + c_4 K_0 \left[\sqrt{s} r_D \right] \right] \quad \text{..... (3.24)}$$

where K_0 is the modified Bessel function of the second kind of order zero and c_3 and c_4 are two unknown, dimensionless constants. Eq. 3.23 describes the pressure behavior for r varying from r_w to r_s. Eq. 3.24

describes the pressure behavior for r ranging from r_s to r_e. Finally, I determine the four unknown constants (c_1,c_2,c_3,c_4) by substituting Eqs. 3.22 and 3.23 into their corresponding boundary conditions (Eqs. 3.18-3.21) and solving the resulting system of four equations. The resulting expressions for c_1,c_2,c_3, and c_4 are given by:

$$c_1 = \frac{f_0 b_4 - f_1 b_5}{b_1[f_0 b_2 - f_1 b_3] - b_0[f_0 b_4 - f_1 b_5]} \quad \text{.....(3.25)}$$

$$c_2 = -\frac{1}{b_1}\left[1 + \frac{b_0[f_0 b_4 - f_1 b_5]}{[b_1[f_0 b_2 - f_1 b_3] - b_0[f_0 b_4 - f_1 b_5]]}\right] \quad \text{.....(3.26)}$$

$$c_3 = \frac{f_2 K_1[a_5]}{f_3 - f_4 + f_5 - f_6} \quad \text{.....(3.27)}$$

$$c_4 = \frac{f_2 I_1[a_5]}{f_3 - f_4 + f_5 - f_6} \quad \text{.....(3.28)}$$

where:

$$\delta = \frac{2}{n-2}, \quad \beta = \frac{n}{n-2}$$

$$a_0 = \sqrt{s}, \quad a_1 = \sqrt{s r_{sD}^n}, \quad a_2 = -a_1\delta, \quad a_3 = a_2[r_{sD}]^{1-n/2}, \quad a_4 = a_0 r_{sD}, \quad a_5 = a_0 r_{eD}$$

$$b_0 = I_\delta[a_2], \quad b_1 = I_{-\delta}[a_2], \quad b_2 = I_\delta[a_3], \quad b_3 = I_\beta[a_3], \quad b_4 = I_{-\delta}[a_3], \quad b_5 = I_{-\beta}[a_3]$$

$$f_0 = a_0 a_1[I_1[a_5]K_0[a_4] + I_0[a_4]K_1[a_5]]$$

$$f_1 = a_0 a_1[I_1[a_4]K_1[a_5] - I_1[a_5]K_1[a_4]]$$

$$f_2 = a_1[b_2 b_5 - b_4 b_3]$$

$$f_3 = a_1 I_0[a_4]K_1[a_5][b_0 b_4 - b_1 b_2]$$

$$f_4 = a_1 I_1[a_4]K_1[a_5][b_0 b_5 - b_1 b_3]$$

$$f_5 = a_1 b_0 I_1[a_5][b_4 K_0[a_4] + b_5 K_1[a_4]]$$

$$f_6 = a_1 b_1 I_1[a_5][b_2 K_0[a_4] + b_3 K_1[a_4]]$$

I solved the system of equations and verified that the solutions satisfy the boundary conditions and original diffusivity equations in Laplace space using the *Mathematica* (2010) software and employing the code that I list in Appendix B.

3.2.2 Development of the Rate Solution in the Laplace Domain

I compute the dimensionless rate and dimensionless cumulative production for a well producing at a constant bottom-hole pressure from the dimensionless pressure solution (Eq. 3.23). I use the approach of Van Everdingen and Hurst (1949), who established the following relationship between the solutions for a constant wellbore pressure and a constant rate in the Laplace domain:

- Dimensionless Rate

$$\overline{q}_D(s) = \frac{1}{s^2}\frac{1}{\overline{p}_D(s)} \quad \text{..... (3.29)}$$

- Dimensionless Cumulative Production

$$\overline{Q}_D(s) = \frac{1}{s^3}\frac{1}{\overline{p}_D(s)} \quad \text{..... (3.30)}$$

q_D is the dimensionless rate and Q_D is the dimensionless cumulative production. Inserting Eq. 3.23 into Eqs. 3.29 and 3.30 gives:

- Dimensionless Rate

$$\overline{q}_D = \frac{\frac{1}{\sqrt{s}}\sqrt{\frac{r_D^n}{r_{sD}^n}}}{c_1 I_{\frac{n}{n-2}}\left[\frac{-2r_D^{\frac{2-n}{2}}\sqrt{sr_{sD}^n}}{n-2}\right] + c_2 I_{\frac{-n}{n-2}}\left[\frac{-2r_D^{\frac{2-n}{2}}\sqrt{sr_{sD}^n}}{n-2}\right]} \quad \text{..... (3.31)}$$

- Dimensionless Cumulative Production

$$\overline{Q}_D = \frac{\dfrac{1}{s^{3/2}}\sqrt{\dfrac{r_D^n}{r_{sD}^n}}}{c_1 I_{\frac{n}{n-2}}\left[\dfrac{-2r_D^{\frac{2-n}{2}}\sqrt{sr_{sD}^n}}{n-2}\right] + c_2 I_{\frac{-n}{n-2}}\left[\dfrac{-2r_D^{\frac{2-n}{2}}\sqrt{sr_{sD}^n}}{n-2}\right]} \quad \text{..... (3.32)}$$

The *qD* and *QD* variables in Eq. 3.31 and 3.32 are defined by the following expressions (Callard and Schenewerk 1995):

- Dimensionless Rate

$$q_D = \frac{1}{2\pi}\frac{qB\mu}{k_o L_e\left(p_i - p_w\right)} \quad \text{..... (3.33)}$$

- Dimensionless Cumulative Production

$$Q_D = \frac{1}{2\pi}\frac{QB}{\phi c_t r_w^2 L_e\left(p_i - p_w\right)} \quad \text{..... (3.34)}$$

Q (bbl) is the cumulative production, and p_w (psi) is the pressure at the wellbore.

3.3 Graphical Presentation and Discussion of Analytical Solutions

In this section, I will present a variety of results for the analytical p_D, $|r_D\ dp_D/dr_D|$, $t_D\ dp_D/dt_D$ and q_D functions. I obtain the real domain solutions by numerical inversion from the Laplace domain using the Gaver-Wynn-Rho algorithm (Valkó and Abate 2004; Abate and Valkó 2004).

Fig. 3.2 presents an example of the permeability distributions used in the results for r_{sD}=200. Previously, I mentioned the rapidly declining nature of the power-law function. Fig. 3.2 clearly illustrates how the degree of stimulation (and, consequently, the permeability) is greatly reduced at a short distance from the wellbore. Notice that the legend in the graph not only identifies the *n* but also a new parameter which I will call the dimensionless wellbore permeability, k_{wD}. We define it as:

$$k_{wD} = \frac{k_w}{k_o} \quad \text{..... (3.35)}$$

where k_w (md) is the permeability at the wellbore ($r=r_w$). It is related to r_{sD} and n by the following expression:

$$k_{wD} = \left[\frac{1}{r_{sD}}\right]^n \quad \text{.....(3.36)}$$

I use the k_{wD} and not n to identify the permeability distributions in my results because k_{wD} provides a more intuitive perception of the degree of stimulation-induced permeability enhancement than the n and allows for a more attractive graphical presentation.

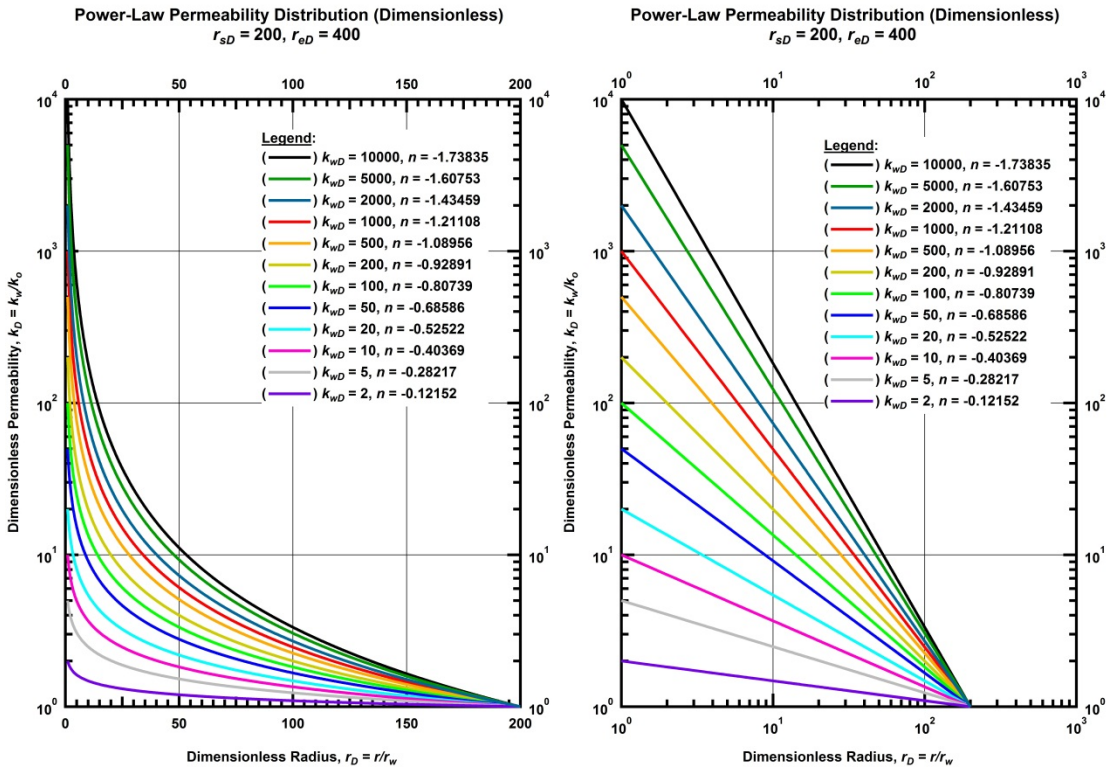

Figure 3.2 — Power-law permeability distributions for r_{sD}=200 (left: semi-log, right: log-log)

Table 3.1 provides all n values corresponding to each pair of r_{sD} and k_{wD} parameters used in the analytical solutions.

Table 3.1 — Power-law permeability parameters used in analytical solutions

		r_{sD}					
	n	300	200	100	50	20	20
k_{wD}	1000	-1.2110825	-1.303764	-1.5000001	-1.7657738	-2.3058654	-2.3058654
	500	-1.0895573	-1.1729398	-1.3494849	-1.5885914	-2.0744872	-2.0744872
	200	-0.92891244	-1	-1.150515	-1.3543665	-1.7686218	-1.7686218
	100	-0.807388	-0.86917582	-1	-1.1771831	-1.5372436	-1.5372436
	50	-0.68586456	-0.73835182	-0.84948507	-1	-1.3058653	-1.3058653
	20	-0.52521819	-0.56541192	-0.65051493	-0.7657756	-1	-1
	10	-0.40369398	-0.43458787	-0.5	-0.58859184	-0.76832176	-1.5372436
	5	-0.28217007	-0.30376361	-0.34948491	-0.41140789	-0.5372436	-1.3058653
	2	-0.12152103	-0.13082287	-0.15051508	-0.17718366	-0.23137841	-0.23137841

Fig. 3.3, which shows the decrease in percent of the maximum permeability with increasing radial distance when r_{sD}=200, presents a more quantitative illustration of the permeability reduction with distance than Fig. 3.2. For $k_{wD} > 100$, the k_D has decayed to 10% of the k_{wD} at or before a distance corresponding to 10% of the r_{sD}. The stimulated radius may be large, but the majority of stimulation-induced permeability increase occurs within a very short distance from the wellbore. The power-law function serves as a very "conservative" stimulation model.

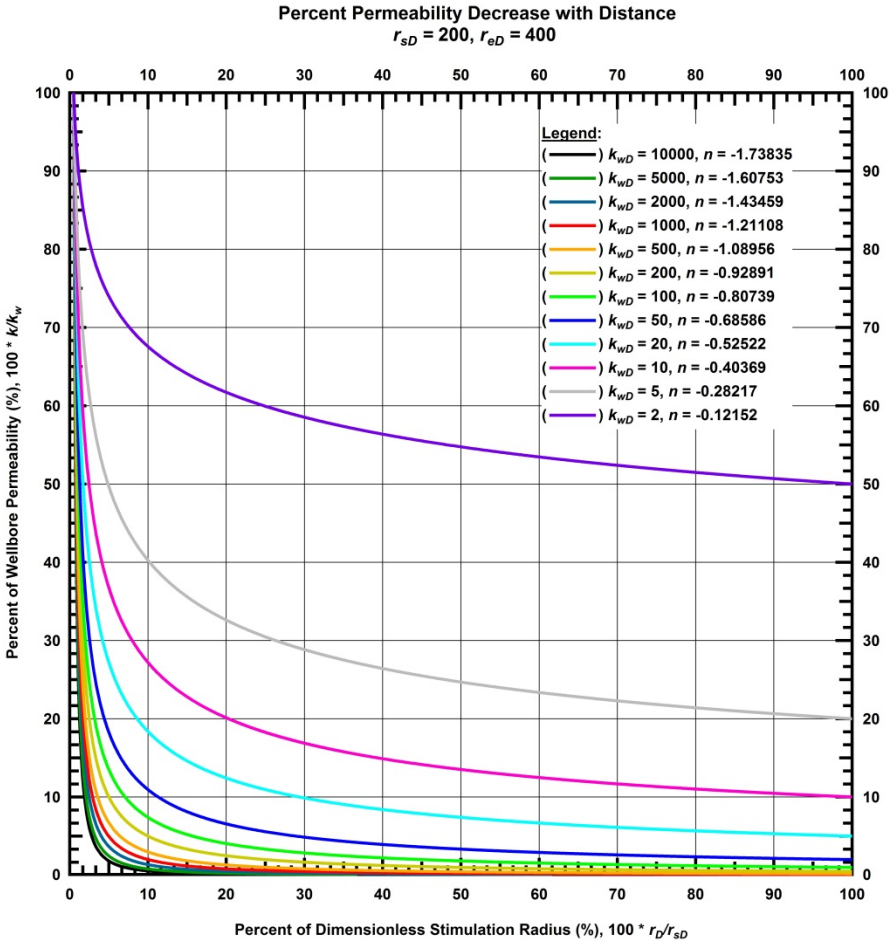

Figure 3.3 — Change in percent of the maximum permeability with radial distance (r_{sD} = 200)

3.3.1 Dimensionless Pressure, Radial Pressure Derivative, and Time Pressure Derivative Solutions

I first present the dimensionless pressure solutions as a function of r_D/r_{sD}, evaluated at specific points in time, i.e., at t_D=1, 10, 100, 10^3, 10^4, 10^5. Unfortunately, the radial composite system utilized to solve my problem does not allow the kind of "type curve" representation presented by Wilson (2003) because my full pressure solution consists of two distinct equations, each valid for a separate region.

Figs. 3.4 – 3.9 display the analytical solutions of the pressure distribution of Eqs. 3.22 and 3.23 at specific times for the cylindrical composite reservoir of Fig. 3.1 with the permeability of the inner (altered)

cylindrical region following a power-law distribution. The permeability distribution controls the pressure response. The p_D values vary considerably depending on the degree of the stimulation-induced permeability enhancement (i.e., k_{wD}) and how quickly the effects of stimulation dissipate (i.e., the magnitudes of r_{sD} and of n) — where larger values of n and smaller r_{sD} correspond to steeper permeability declines. The effect of k_{wD} and r_{sD} on the dimensionless pressure is most pronounced near the wellbore, where the permeability change is the largest. At distances far from the wellbore, close to r_D/r_{sD}=1, where the altered permeability is approaching the native reservoir permeability (as dictated by Eq. 3.10), the dimensionless pressure displays similar behaviors for all cases. For example, notice the r_{sD}=20 cases at t_D=100 in **Fig. 3.6**. In the stimulated region near r_D/r_{sD}=1, there is little divergence in p_D between all cases because there is also little divergence in permeability between all cases. Eventually, the k_{wD} cases for r_{sD}=20 converge at r_D/r_{sD}=1 (see **Fig. 3.7**). They form a single curve (i.e. unable to distinguish one k_{wD} case from another) because the pressure transient has moved beyond the stimulated zone, and the p_D is no longer influenced by the variable permeability.

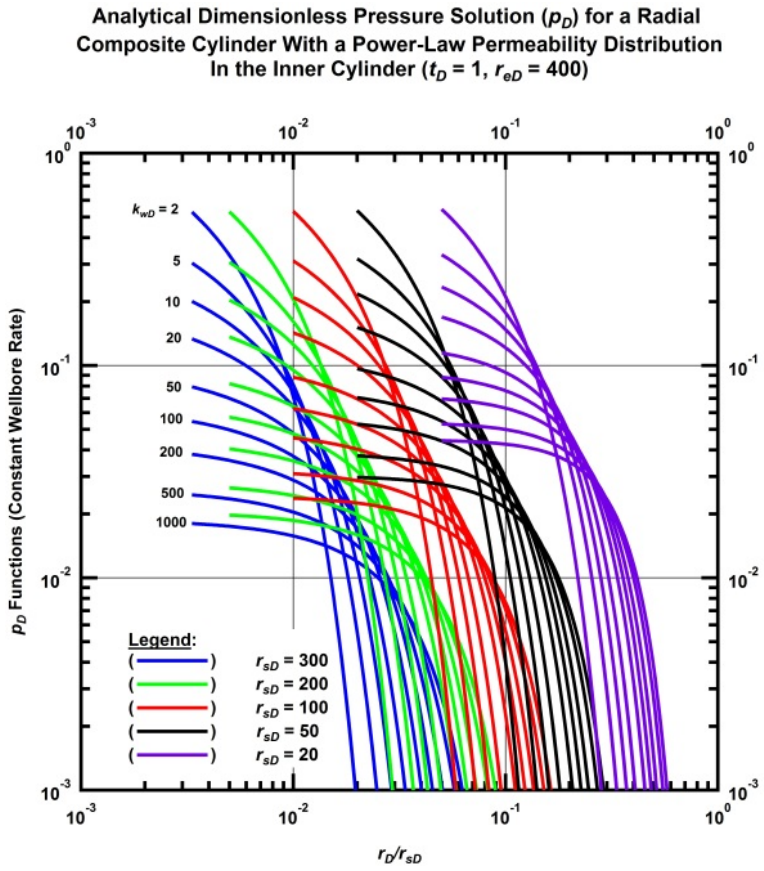

Figure 3.4 — Log-log plot of the analytical p_D solutions at t_D=1 for a horizontal well producing at a constant rate, centered in a radial composite reservoir with a power-law permeability distribution in the inner region

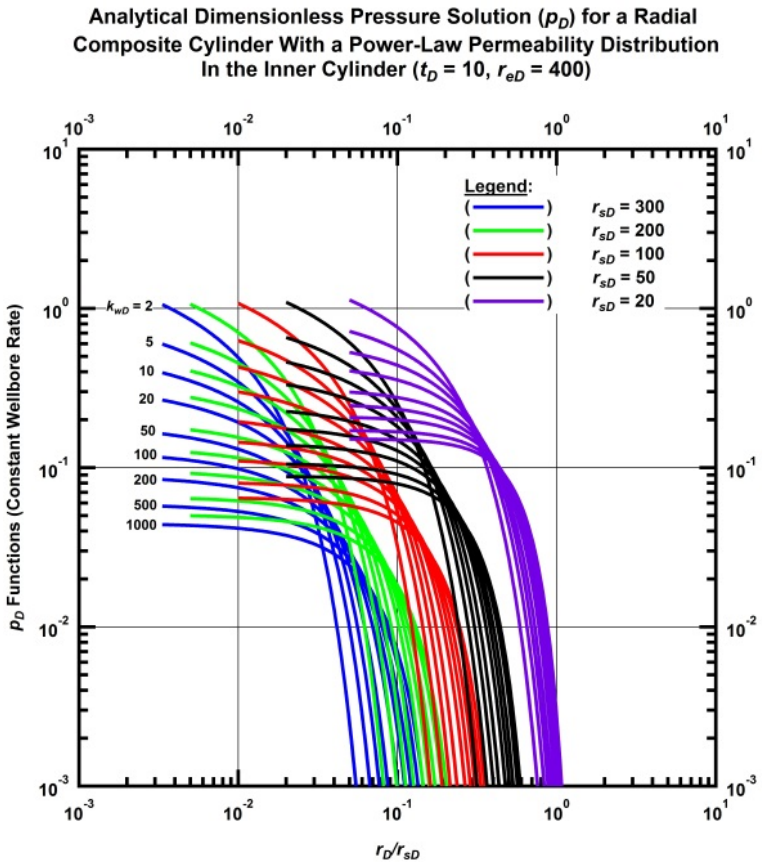

Figure 3.5 — Log-log plot of the analytical p_D solutions at t_D=10 for a horizontal well producing at a constant rate, centered in a radial composite reservoir with a power-law permeability distribution in the inner region

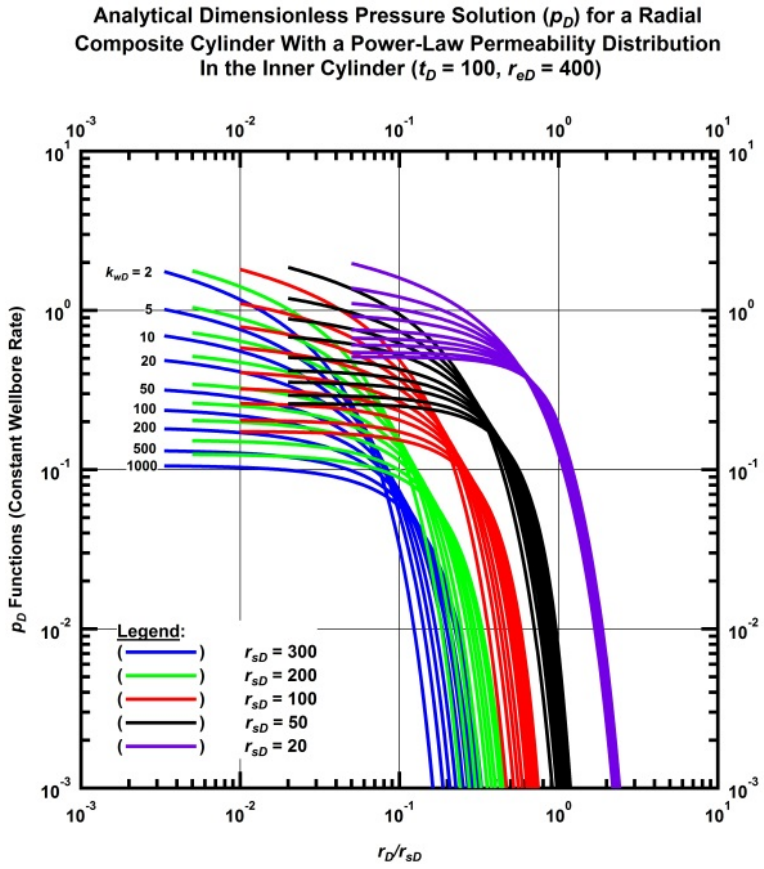

Figure 3.6 — Log-log plot of the analytical p_D solutions at t_D=100 for a horizontal well producing at a constant rate, centered in a radial composite reservoir with a power-law permeability distribution in the inner region

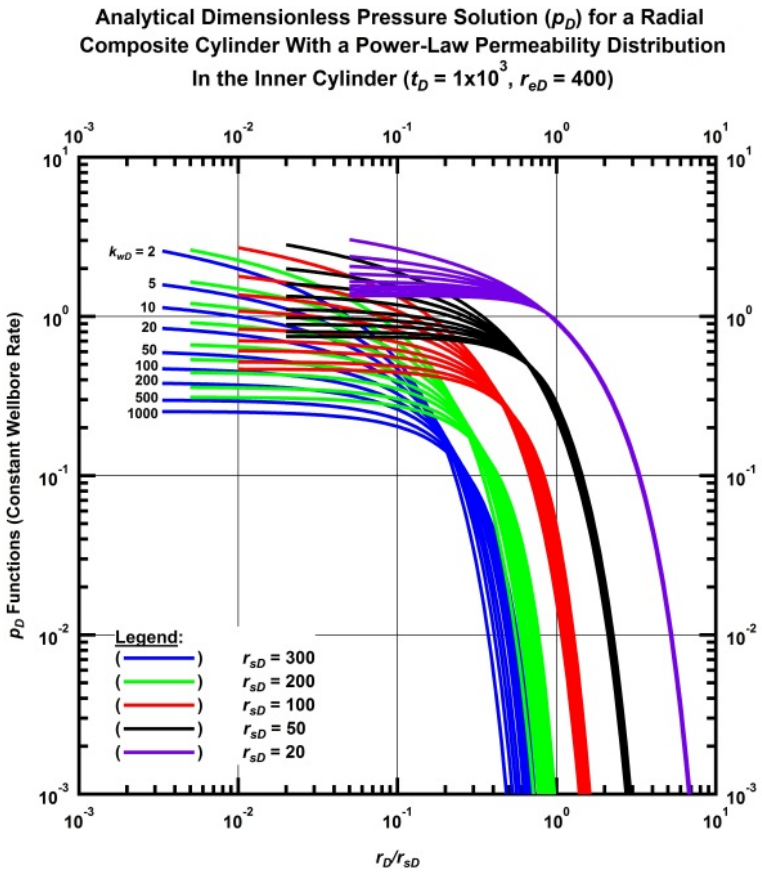

Figure 3.7 — Log-log plot of the analytical p_D solutions at t_D=10^3 for a horizontal well producing at a constant rate, centered in a radial composite reservoir with a power-law permeability distribution in the inner region

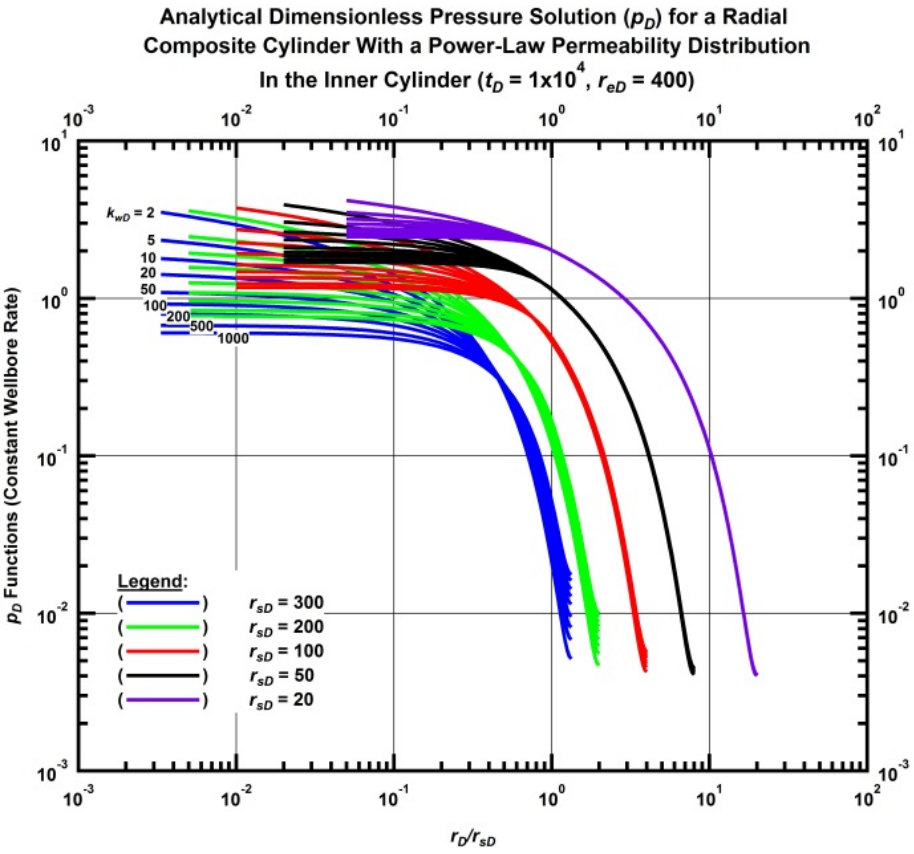

Figure 3.8 — Log-log plot of the analytical p_D solutions at t_D=10^4 for a horizontal well producing at a constant rate, centered in a radial composite reservoir with a power-law permeability distribution in the inner region

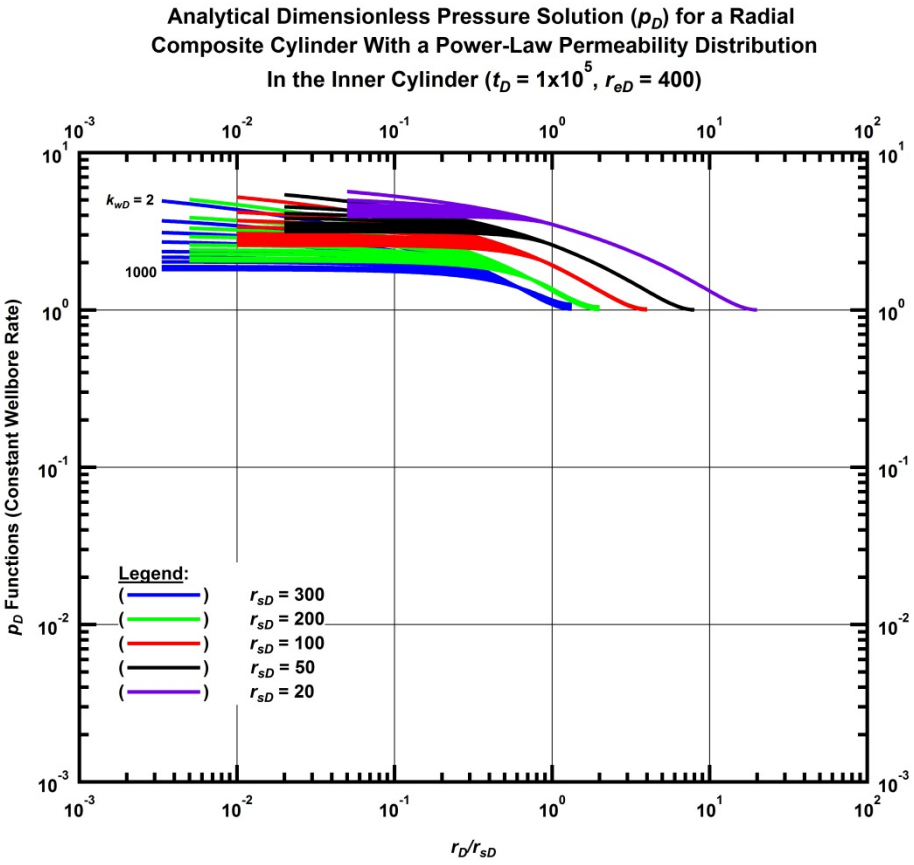

Figure 3.9 — Log-log plot of the analytical p_D solutions at t_D=10^5 for a horizontal well producing at a constant rate, centered in a radial composite reservoir with a power-law permeability distribution in the inner region

The p_D solutions presented above are validated by comparison to numerical simulation results. I present an example for the case of r_{sD}=200 at t_D=10^3 in **Fig. 3.10**. Fig. 3.10 shows that there is excellent agreement between the numerical and analytical solutions. There is a slight divergence in solutions shown in the semi-log graph (right-hand side) at radial distances farther from the wellbore where the reservoir pressure is approaching that of the initial reservoir pressure (p_i). The difference can be considered negligible. The rest of the analytical and numerical comparisons presented in Appendix C confirm that the solutions (Eq. 3.24-3.28) can be considered "analytically" accurate (i.e. near exact).

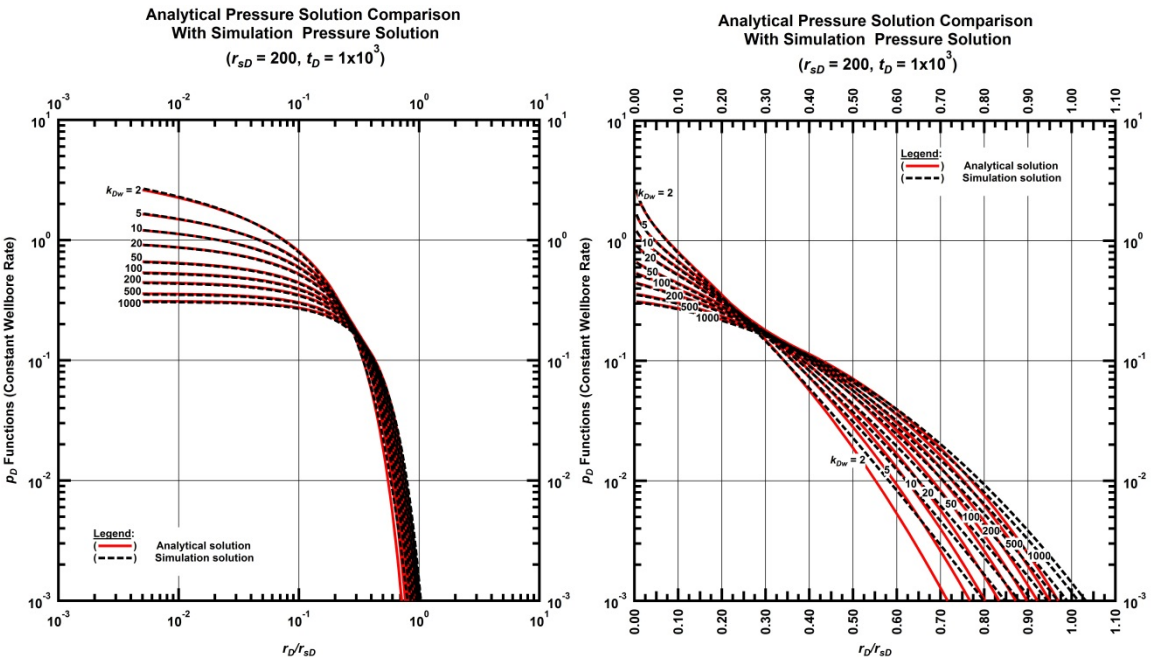

Figure 3.10 — Comparison of analytic p_D solution to numerical p_D solution for a reservoir with $r_{sD}=200$ at $t_D=10^3$ (left: log-log, right: semi-log)

The dimensionless radial pressure derivatives (p_{Ddr}) in **Figs. 3.11 – 3.16** (as functions of r_D/r_{sD}) correspond to Figs. 3.4 to 3.9, and evaluated at the same times. This rendering of the p_{Ddr} clearly identifies the n of each case's power-law permeability distribution by exhibiting a linear portion of the p_{Ddr}. I mark examples of the linear p_{Ddr} using dashed black lines in Fig. 3.11. The slope of a line on a log-log scale corresponds to the exponent value of a power-law function, so by determining the slope of the linear portion of the p_{Ddr}, I also obtain n. The p_{Ddr} linear behavior does not necessarily cease at r_D/r_{sD}=1. For a sufficiently small r_{sD} (such as r_{sD}=20), I can also identify the constant permeability (homogeneous) region of the reservoir. When the pressure transient is deep into the unstimulated zone, the p_{Ddr} clearly displays – as expected - a horizontal line or zero-slope at a p_{Ddr} value of 1 (marked by a dashed line in Fig. 3.16). A p_{Ddr} with zero-slope corresponds to a power-law permeability distribution with n = 0 which signifies a constant permeability.

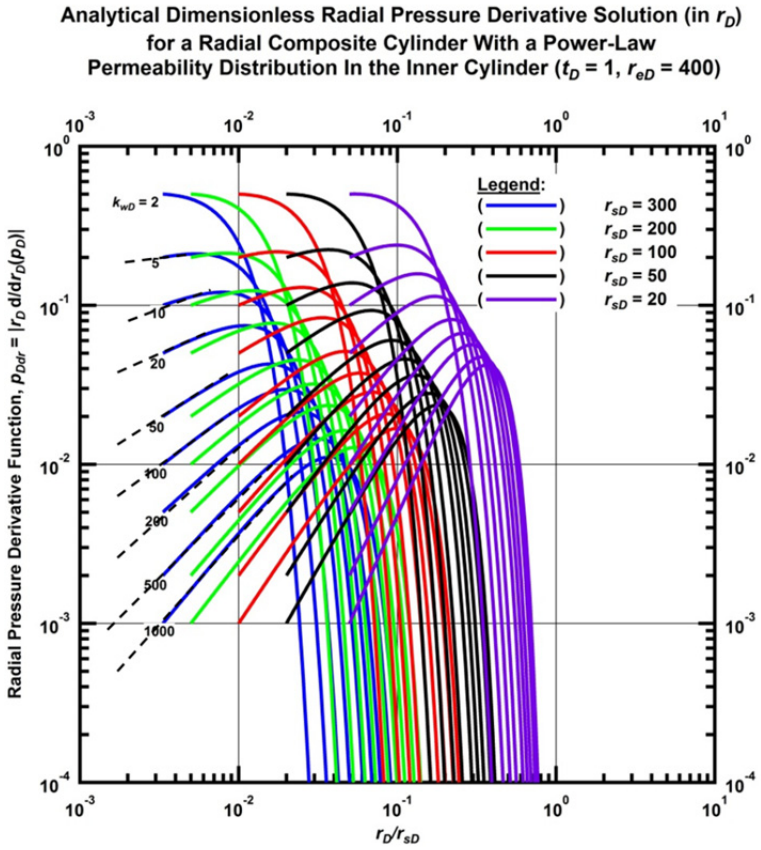

Figure 3.11 — Log-log plot of the analytical p_{Ddr} solutions at t_D=1 for a horizontal well producing at a constant rate, centered in a radial composite cylinder with a power-law permeability distribution in the inner region

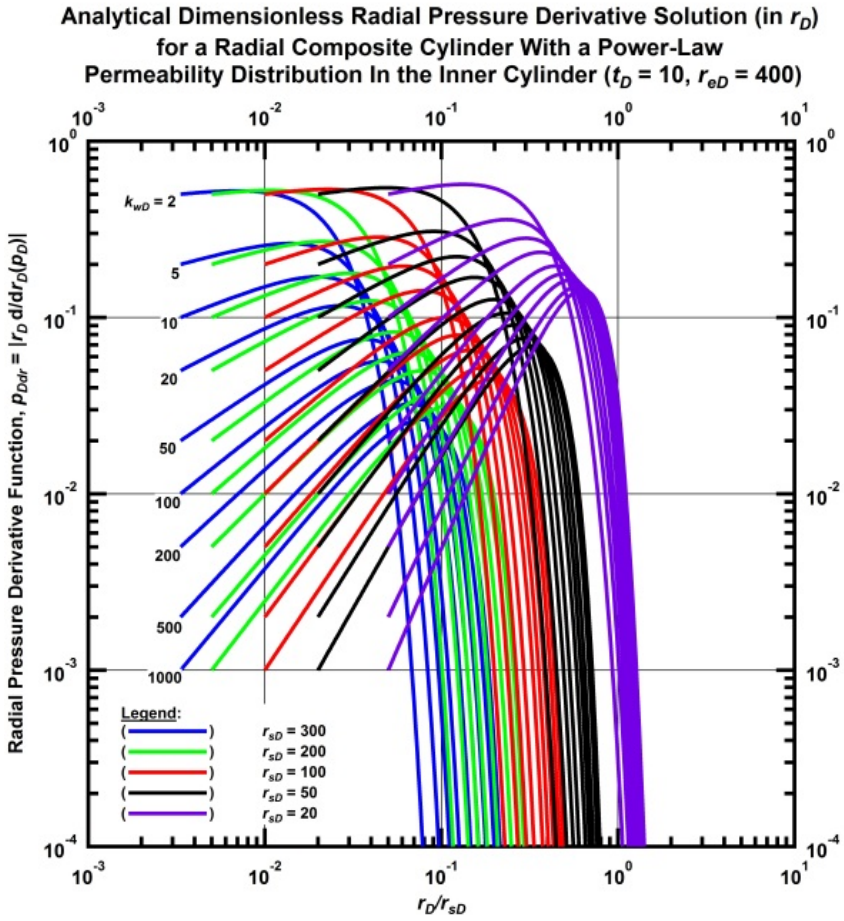

Figure 3.12 — Log-log plot of the analytical p_{Ddr} solutions at t_D=10 for a horizontal well producing at a constant rate, centered in a radial composite reservoir with a power-law permeability distribution in the inner region

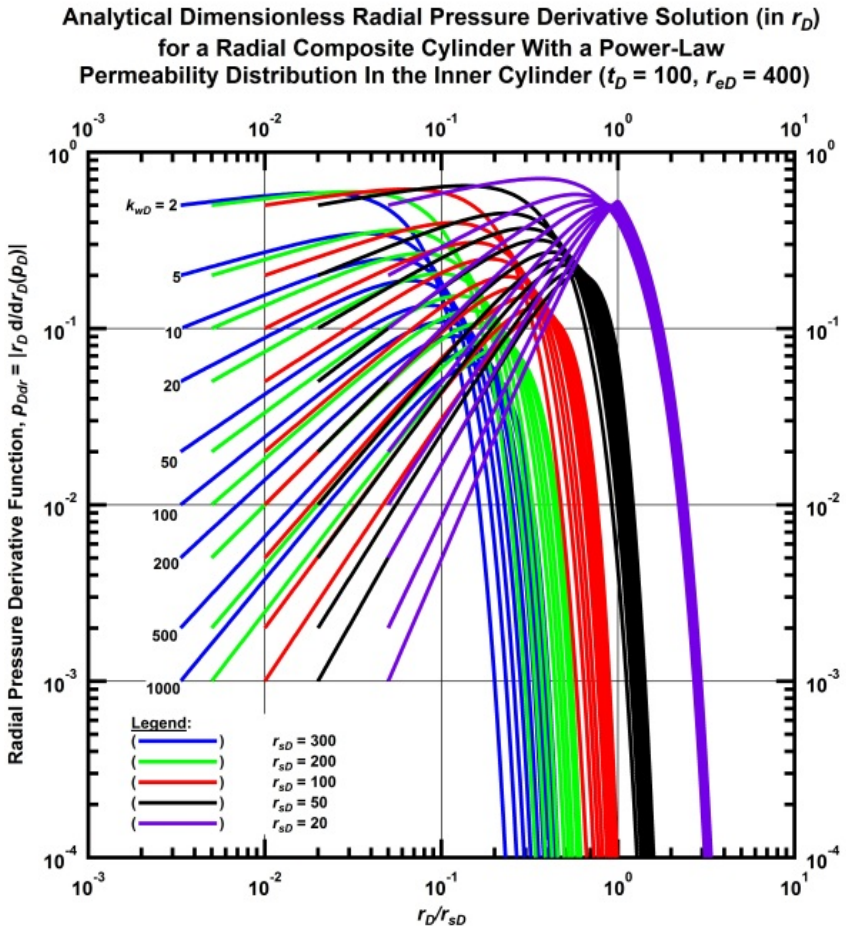

Figure 3.13 — Log-log plot of the analytical p_{Ddr} solutions at t_D=100 for a horizontal well producing at a constant rate, centered in a radial composite reservoir with a power-law permeability distribution in the inner region

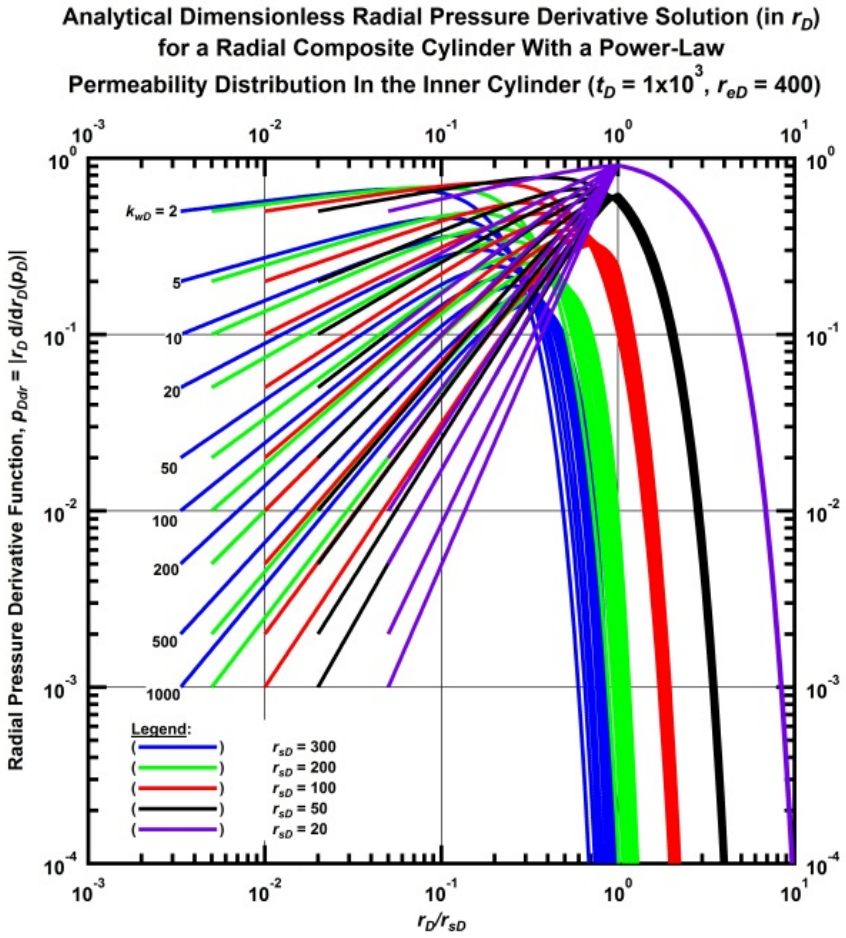

Figure 3.14 — Log-log plot of the analytical p_{Ddr} solutions at t_D=10^3 for a horizontal well producing at a constant rate, centered in a radial composite reservoir with a power-law permeability distribution in the inner region

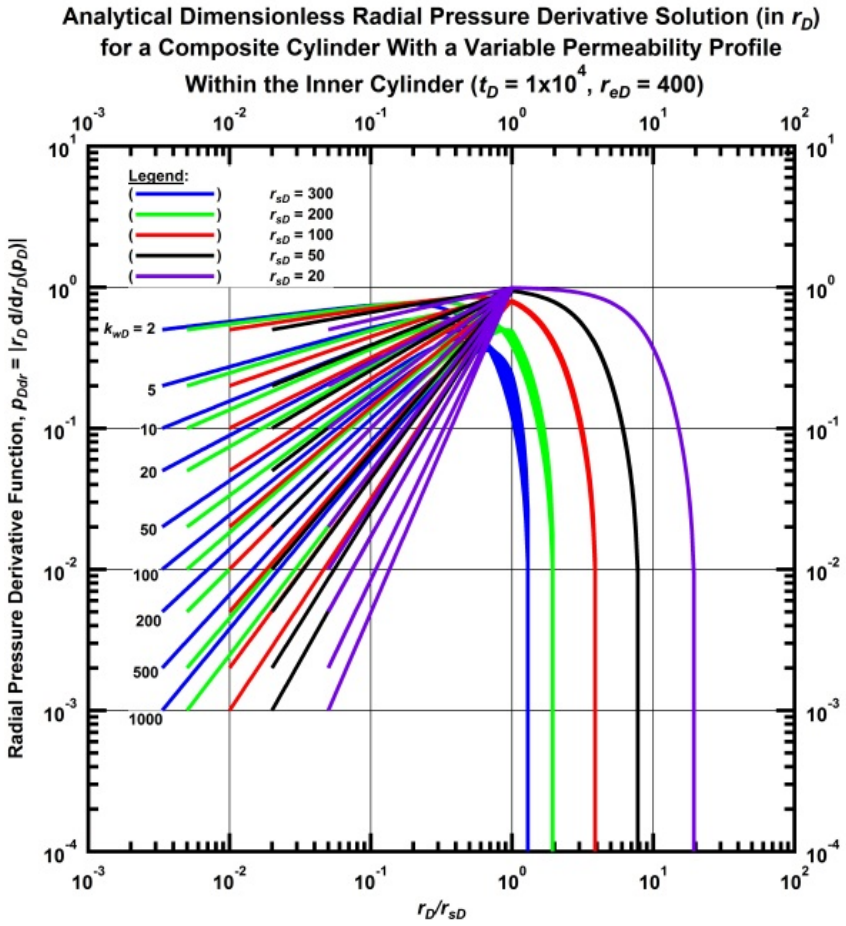

Figure 3.15 — Log-log plot of the analytical p_{Ddr} solutions at t_D=10^4 for a horizontal well producing at a constant rate, centered in a radial composite reservoir with a power-law permeability distribution in the inner region

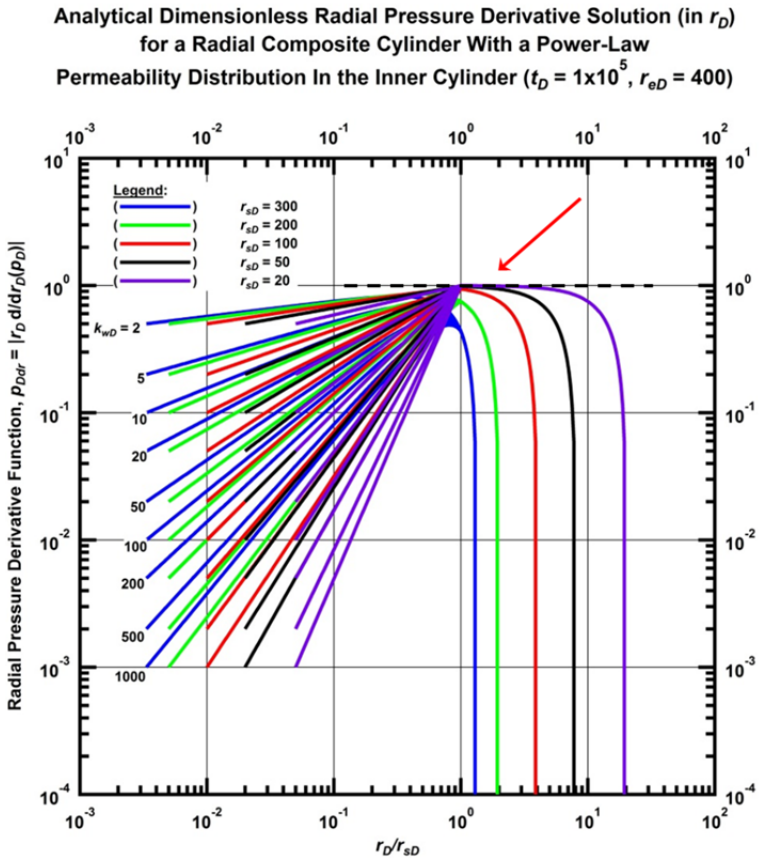

Figure 3.16 — Log-log plot of the analytical p_{Ddr} solutions at t_D=10^5 for a horizontal well producing at a constant rate, centered in a radial composite reservoir with a power-law permeability distribution in the inner region

Fig. 3.17 shows the dimensionless time pressure derivative (p_{Ddt}) as a function of t_D. The behavior of p_{Ddt} can clearly identify the time beyond which the stimulated zone no longer influences the pressure response. For a homogeneous radial flow system, p_{Ddt} should converge to a value of 0.5. In the cases of small r_{sD} (=20, 50, 100), p_{Ddt} does converge to a value of 0.5 (denoted by the horizontal part of the curve) because the pressure response is no longer affected by the variable permeability in the limited stimulated zone. However, in the cases of larger stimulated region, i.e., r_{sD}=300 and 200, p_{Ddt} does not converge to a value of 0.5 before the onset of the pseudo-steady state flow at t_D=10^5, beyond which the p_{Ddt} displays a unit slope. In other words, at no point in time before pseudo-steady state is the pressure response at the wellbore not subject to the influence of the stimulated zone.

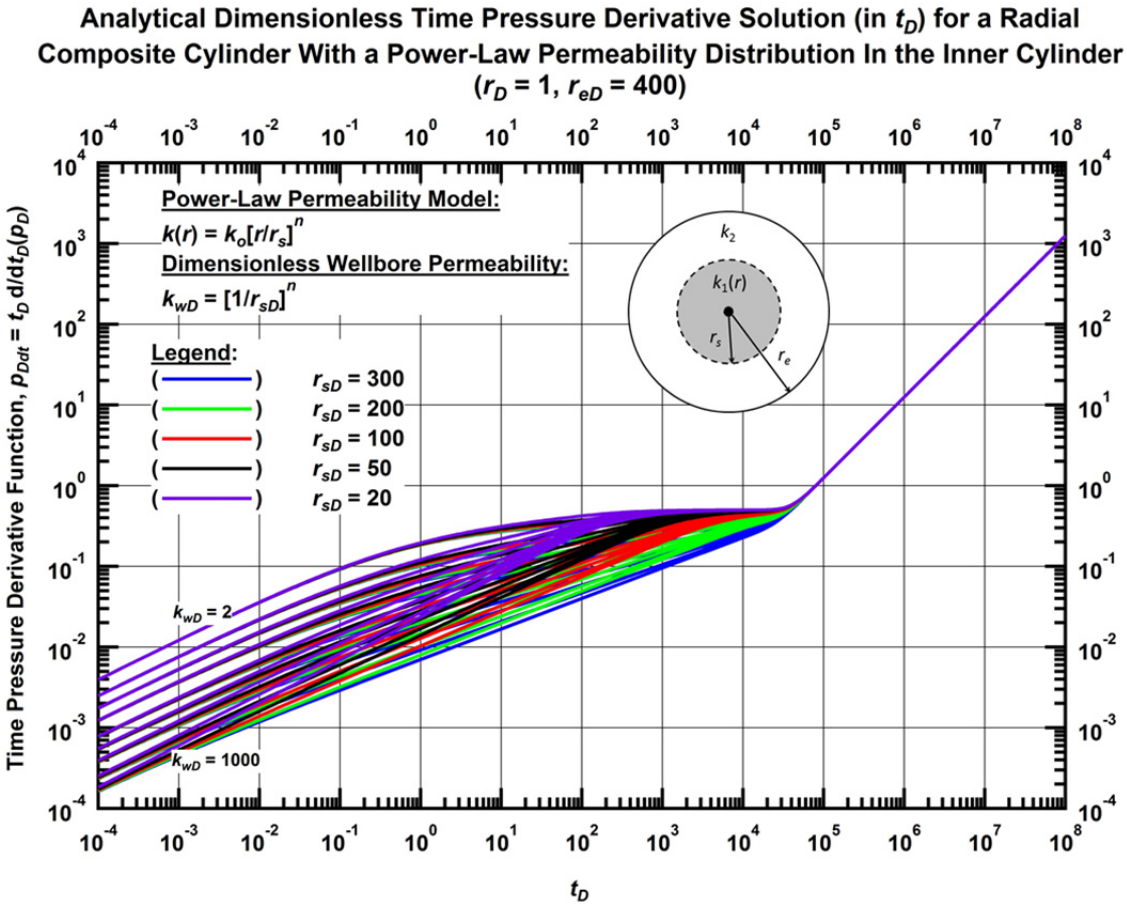

Figure 3.17 — Log-log plot of the analytical p_{Ddt} solutions at r_D=1 for a horizontal well producing at a constant rate, centered in a radial composite cylinder with a power-law permeability distribution in the inner region

3.3.2 The Rate Solutions

Fig. 3.18 presents the dimensionless production rate, q_D, for a wellbore producing at a constant pressure when the permeability distribution and the geometry of the reservoir are the same as in the previous section (3.3.1). As expected, the permeability distribution controls the rate response. At early times (t_D<10^{-1}), when the pressure transient has not advanced very far into the reservoir, k_{wD} controls the rate response — the larger the k_{wD}, the greater the initial rates. As time progresses, q_D response depends on both the degree of the stimulation-induced permeability enhancement (i.e., k_{wD}) and how quickly the effects of

stimulation dissipate (i.e., the magnitudes of r_{sD} and of n). The quicker the permeability dissipates, the steeper the rate declines. Eventually (around t_D=10^5), transient flow is succeeded by an exponential decline, indicating that the pressure transient has reached the impermeable outer reservoir boundary. The reservoirs with the largest r_{sD} reach boundary-dominated flow first, followed by the reservoirs with progressively smaller r_{sD}.

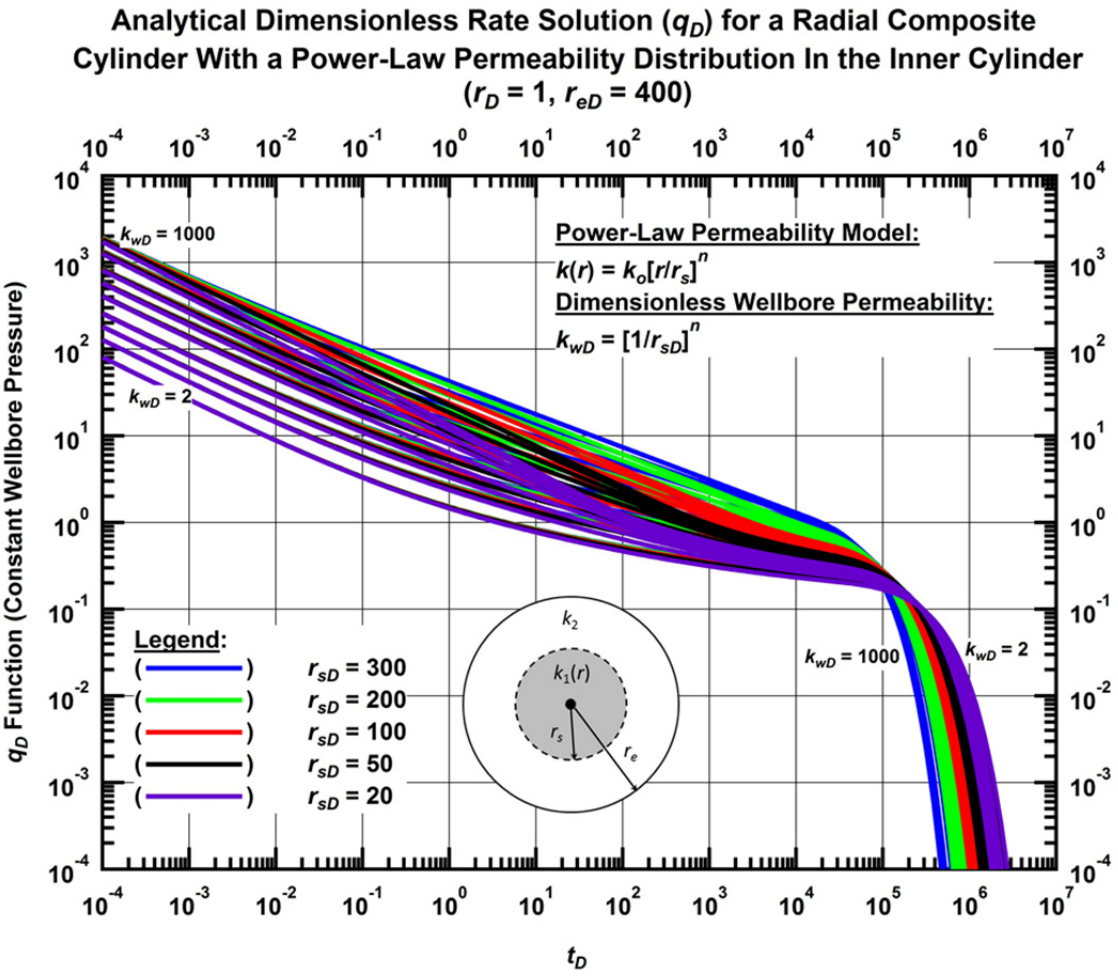

Figure 3.18 — Log-log plot of the analytical q_D solutions at r_D=1 for a horizontal well producing at a constant pressure, centered in a radial composite cylinder with a power-law permeability distribution in the inner region

I validated the analytical q_D solutions by comparing them to numerical simulation results. I present an example for the case of r_{sD}=200 in **Fig. 3.19**. Fig. 3.19 shows that there is excellent agreement between the numerical and analytical solutions. There is some divergence in the solutions for the smaller k_{wD} cases. This is a result of insufficient grid discretization near the wellbore not a deficiency in the analytical solution. The ultra-low permeability of the reservoir requires extremely small grids close to the wellbore where the pressure and permeability change is greatest. Overall, the results of the analytical and numerical comparisons (more presented in Appendix C) validate the analytical q_D solution.

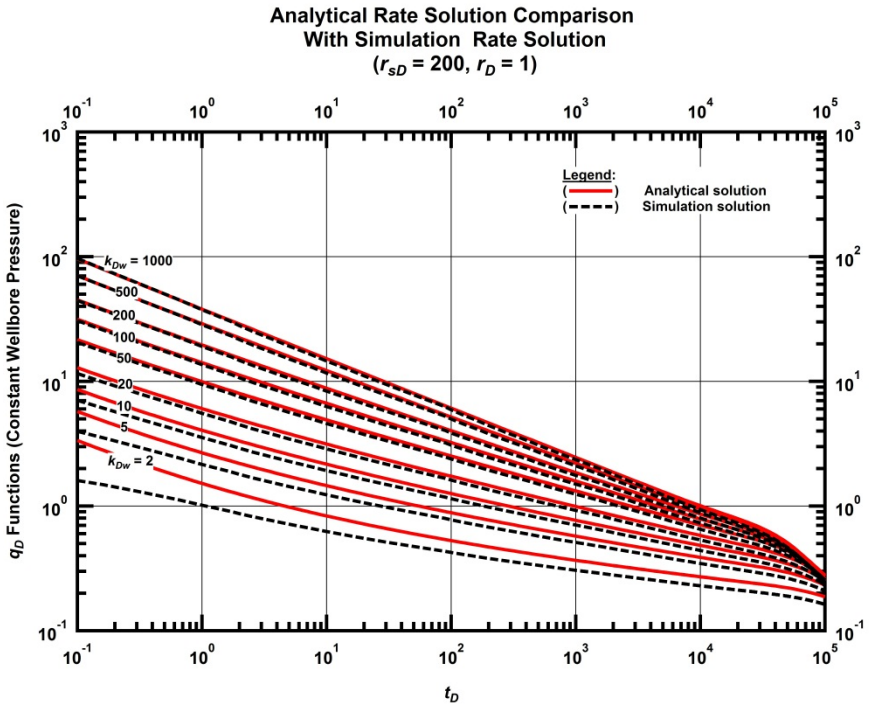

Figure 3.19 — Log-log plot comparing the analytic q_D solution to numerical q_D solution for a reservoir with r_{sD}=*200* at r_D=*1*.

4. COMPARISON OF POWER-LAW STIMULATION TO MULTI-STAGE HYDRAULIC FRACTURING

4.1 Simulation Parameters and Gridding

The main objective of this component of my study is to compare the performance of the two stimulation approaches I discussed earlier. To achieve this end, I utilized a fully implicit numerical simulator (FTSim – Flow and Transport Simulator) based on the TOUGH+ reservoir simulation code developed at the Lawrence Berkeley National Laboratory (Moridis et al. 2008; Moridis et al. 2010). I did not employ the PPR analytical solution for the comparisons because by using the same simulator (thus the same methods of calculating changes in porosity and liquid density with pressure) for both stimulation approaches, I am able to isolate the differences in solutions to only the stimulation geometries (i.e., equally spaced, circular fractures along the wellbore versus a cylindrical volume of stimulated rock along the entire length of the well) and the permeabilities within those geometries.

I limit the simulations to isothermal Darcy flow of a single-phase, single-component, black oil in an ultra-low permeability reservoir. Table 4.1 lists the reservoir fluid and rock properties used in the simulations.

Table 4.1 — Reservoir, completion and fluid properties used in simulations of power-law permeability reservoir and multi-fractured horizontal

Reservoir and Completion Properties	SI Units	Field Units
Reservoir permeability, k_o	9.8693×10^{-20} m^2	1.0×10^{-4} md
Matrix compressibility, c_f	1.0×10^{-9} 1/Pa	6.8948×10^{-6} 1/psia
Matrix porosity (at p_i), ϕ_i	4%	4%
Reservoir height, h or $2*r_e$	60.96 m	200 ft
Reservoir width, w or $2*r_e$	60.96 m	200 ft
Reservoir length, L_e	1524 m	5000 ft
Wellbore length, L_w	1524 m	5000 ft
Wellbore radius, r_w	7.62×10^{-2} m	.25 ft
Fracture width, w_f	3.048 mm	.01 ft
Fracture porosity, ϕ_f	33%	33%
Initial reservoir pressure, p_i	2.4132×10^7 Pa	3500 psia
Well pressure, p_{wf}	6.8946×10^6 Pa	1000 psia

Fluid Properties	SI Units	Field Units
Oil compressibility, c_o	1.0×10^{-8} 1/Pa	6.8948×10^{-5} 1/psia
Oil density (at 14.7 psia), ρ_{atm}	696.658 kg/m^3	43.5 lbm/ft^3
Oil viscosity, μ_o	4.93×10^{-4} Pa·sec	.493 cp

The reservoir, completion and fluid properties listed in Table 4.1 are the same for all simulation cases. The reservoir is originally (i.e., before stimulation) homogeneous and isotropic, and the fluid properties are uniform throughout the reservoir. Only the oil density and the matrix porosity change with pressure according to the following functions:

$$\rho_o = \rho_{atm} \exp\left[c_o \left[p - p_{atm}\right]\right] \quad (4.1)$$

$$\phi = \phi_i \exp\left[c_f \left[p - p_i\right]\right] \quad (4.2)$$

ρ_o (lbm/ft^3) is the oil density; ρ_{atm} (lbm/ft^3) is the oil density at atmospheric pressure; p_{atm} (psi) is the atmospheric pressure; c_o (1/psi) is the oil compressibility; ϕ_i (fraction) is the porosity at p_i and c_f (1/psi) is the matrix compressibility. The primary practical differences between simulations of the power-law permeability reservoir (referred to as "PPR") and the multi-stage hydraulically fractured reservoir with a horizontal well (referred to as "MFH") are obviously the permeability distributions and the respective

domain geometries, as these affect the discretization (grid development) approach. I discretize the PPR using cylindrical grids, which is an obvious choice when considering the form of the analytical solution and the power-law permeability function (Eq. 3.10). I discretize the reservoir only in the radial direction (**Fig. 4.1**), i.e., I consider a single cylindrical slice (along the z-axis) of the system shown in Fig. 3.1, and I only model one-dimensional flow.

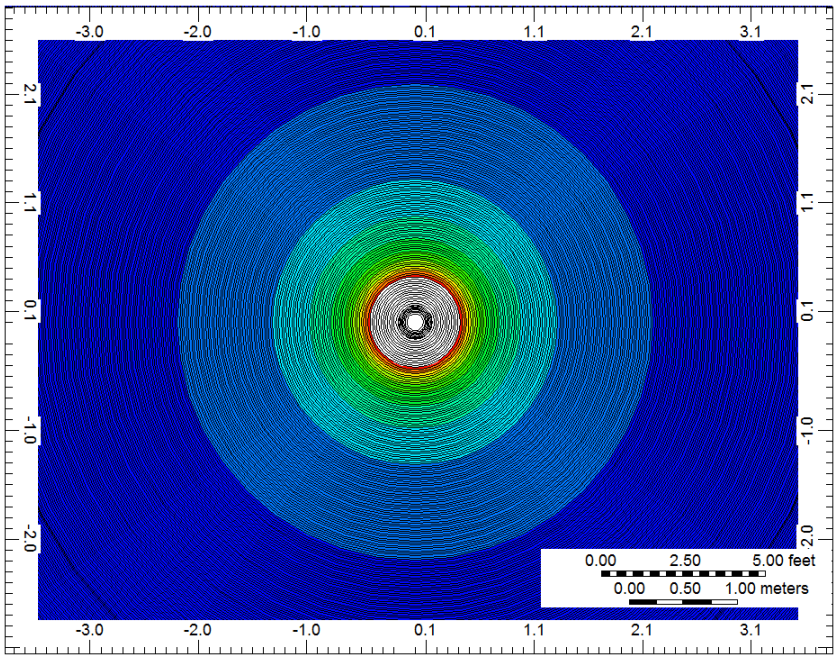

Figure 4.1 — Grid scheme for numerical simulation (radial increments = 2 cm)

Eq. 3.1 determines the permeability of the grid cells within the stimulated zone, with the radius (*r)* measured from the grid center to the center of gravity of each cell. Table 4.2 lists all combinations of PPR model stimulation parameters (r_s, n, k_{wD}) used for the comparison to the MFH performance.

Table 4.2 — Power-law permeability reservoir stimulation parameters used for comparison to multi-fractured horizontal

		r_s		
	n	75 ft	50 ft	25 ft
k_{wD}	10000	-1.6147777	-1.7383519	-2
	5000	-1.4932535	-1.6075279	-1.8494849
	2000	-1.3326073	-1.434588	-1.650515
	1000	-1.2110825	-1.303764	-1.5000001
	500	-1.0895573	-1.1729398	-1.3494849
	200	-0.92891244	-1	-1.150515
	100	-0.807388	-0.86917582	-1
	50	-0.68586456	-0.73835182	-0.84948507
	20	-0.52521819	-0.56541192	-0.65051493

I also discretize the domain corresponding to the MFH treatment using a cylindrical grid system to eliminate any geometric differences between the MFH and PPR that might distort the comparisons. I discretize the MFH domain in two dimensions. The radial discretization (r) advances along the direction of the hydraulically-induced fracture (now represented as a cylindrical disk), and the horizontal discretization (z) advances in the direction of the wellbore. Both the fracture and wellbore contribute to flow. I neglect gravity, so the orientation of the wellbore doesn't matter as long as the fractures are in the same position relative to the wellbore. The fracture radius does not reach the top or bottom boundaries of the reservoir (i.e., I consider a partially-penetrating fracture). I constrain the fracture height to be the same dimensions as the full fracture length ($2*x_f$), creating a perfectly circular fracture area.

I simulate various combinations of fracture dimensions, fracture properties and number of fractures for comparison to the PPR cases. Table 4.3 lists the various combinations I used in this study.

Table 4.3 — MFH stimulation parameters used for comparison to PPR

Fracture half-length, x_f	Fracture conductivity, wk_f
75 ft	10 md-ft
75 ft	1 md-ft
75 ft	0.1 md-ft
50 ft	10 md-ft
50 ft	1 md-ft
50 ft	0.1 md-ft
25 ft	10 md-ft
25 ft	1 md-ft
25 ft	0.1 md-ft

Each set of parameters above is simulated with the following number of fractures:

Number of fractures	istance between fractures, d_f
100	50 ft
75	66.66 ft
50	100 ft
25	200 ft

4.2 Comparison of PPR and MFH Performance

In this section I compare three sets of PPR and MFH simulation results (displayed in a dimensionless form) in an ultra-low permeability reservoir. Each set considers a x_f and r_s of different size, ranging from x_f = 75 ft. and r_s = 75 ft. (large) to xf = 25 ft. and r_s = 25 ft (small). The PPR stimulation radius (r_s) equals the MFH fracture half-length (x_f) in each comparison. The PPR cases include various k_{wD}, ranging from 20 to 10000. The MFH cases include wk_f of 10, 1, and 0.1 md-ft, with a fracture density of 25, 50, 75 and 100 fractures along the horizontal wellbore (see Table 4.1). In all the simulations, p_w, was kept constant at 1000 psia for a period of 40 years.

I compare q_D, Q_D, and recovery factor (RF) as a percent of original oil-in-place (OOIP) estimated from the PPR and MFH simulations. The main objective of this effort is to evaluate whether the PPR provides a promising stimulation strategy in ultra-low permeability reservoirs by comparing it to the performance of the current standard stimulation method of multi-stage hydraulic fracturing. Note that there are no economic considerations in this study, which only aims to evaluate a stimulation method - that is currently no more than a concept – vis-à-vis a production standard.

4.2.1 Comparison of PPR to MFH: Large Stimulation Size

The first set of simulation results compares the q_D corresponding to the PPR with r_s=75 ft to that for the MFH with x_f=75 ft. I discuss the results sequentially, beginning from the highest fracture conductivity case and moving to the lowest, beginning with wk_f =10 md-ft.

All measures of comparison, i.e., q_D, Q_D and RF (see **Figs. 4.2–4.4**, respectively), show that the MFH cases with wk_f =10 md-ft, outperform the PPR, with the exception of the case of the 25 fracture (= low) density. The MFH case with fracture frequency of 25 does not provide enough fractures, thus not enough fracture surface area to outperform all of the PPR cases. It exhibits a q_D, Q_D and RF between those corresponding to the k_{wD}=500 and k_{wD}=200 PPR cases. In general, Fig. 4.2 shows that the PPR provides excellent q_D at early times, but the rate steeply declines as a result of the rapidly declining nature of the power-law permeability function. The MFH, because of its high conductivity fractures, also demonstrates excellent initial rates. However, the initial rate decline is more gradual than the PPR because the large fracture surface areas provides access to significant volumes of easily drainable hydrocarbons. Then between t_D =10 and t_D =10^3, I observe an accelerated rate decline with the onset of formation linear flow when the MFH q_D curves exhibit a slope of -1/2. PPR cases with a k_{wD}>500 display q_D declines with a slope similar to the MFH during formation linear flow, but this is coincidence. There are no fractures in the PPR, so it does not experience formation linear flow.

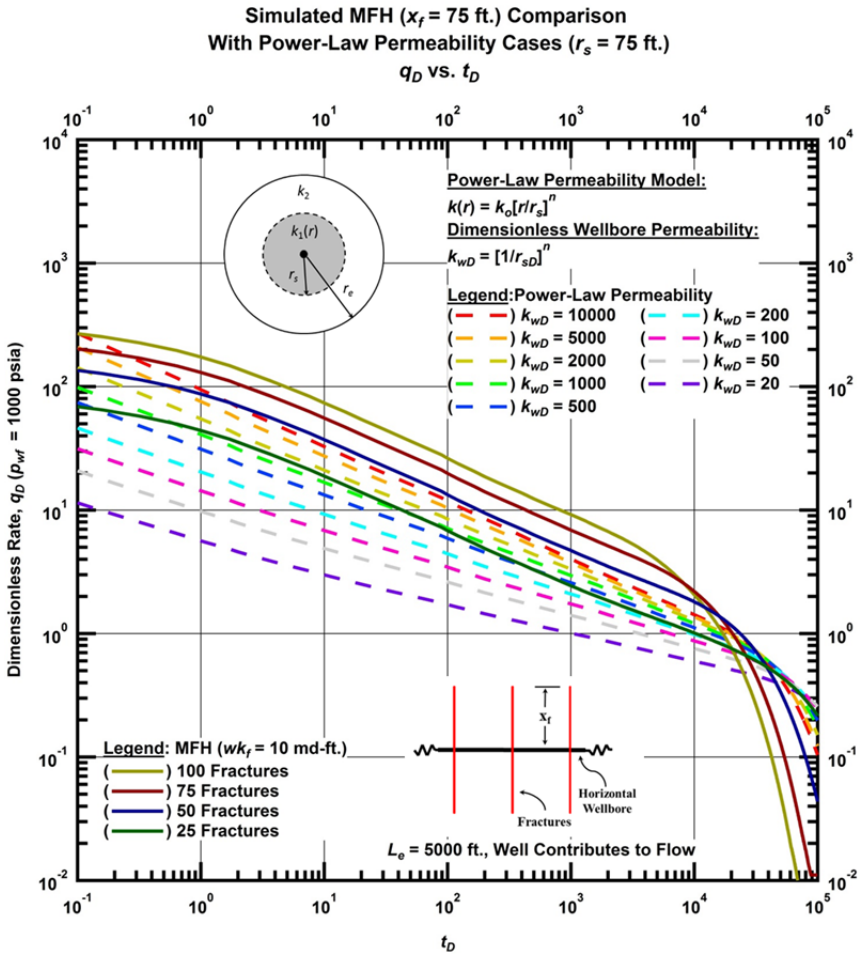

Figure 4.2 — Log-log plot of q_D vs. t_D for a PPR with r_s = 75 ft and a MFH with x_f = 75 ft and 10 md-ft fracture conductivity

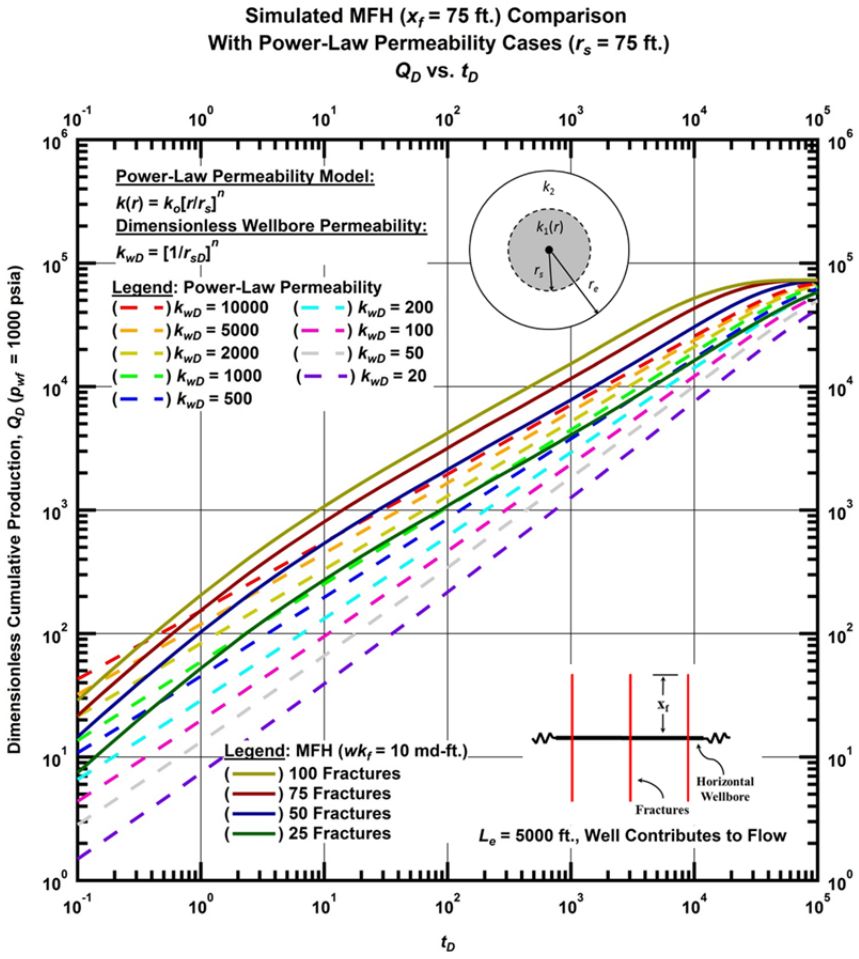

Figure 4.3 — Log-log plot of Q_D vs. t_D for a PPR with r_s = 75 ft and a MFH with x_f = 75 ft and 10 md-ft fracture conductivity

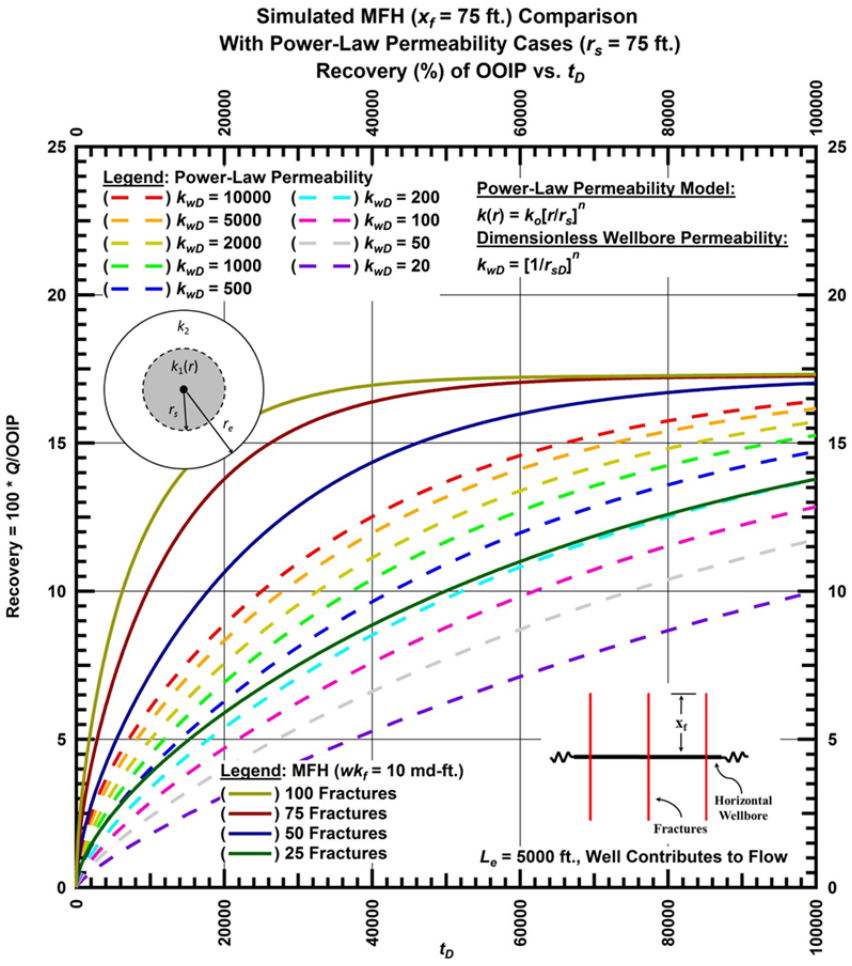

Figure 4.4 — Linear plot of RF vs. t_D for a PPR with r_s = 75 ft and a MFH with x_f = 75 ft and 10 md-ft fracture conductivity

Next, I evaluate the relative performance of the PPR and the MFH approaches for the case of wk_f =1 md-ft using the same q_D, Q_D and RF criteria. The effect of the change in fracture conductivity shows most distinctly in the early time q_D (**Fig. 4.5**) during the drainage of the fracture and near fracture regions. The lower fracture conductivity diminishes the initial rates by an order of magnitude and extends the time it takes to drain the fracture and near fracture regions. As in the wk_f =10 md-ft case, the q_D, Q_D (**Fig. 4.6**) and RF (**Fig. 4.7**) clearly show that all MFH cases except that for the fracture density of 25, outperform the PPR. With wk_f =1 md-ft, the 25 fracture case exhibits a q_D, Q_D and RF between those corresponding to

the k_{wD}=200 and k_{wD}=100 PPR cases. The results of this study indicate that PPR does not perform as well as the MFH when the fracture conductivity is high and the fracture density is high, but the PPR can yield modest (or even decent) production from ultra-low permeability reservoirs (if it can progress past the concept stage and shown to be feasible) and could be a potentially viable production alternative under appropriate economic, reservoir and operational conditions that are not favorable to the MHF treatment.

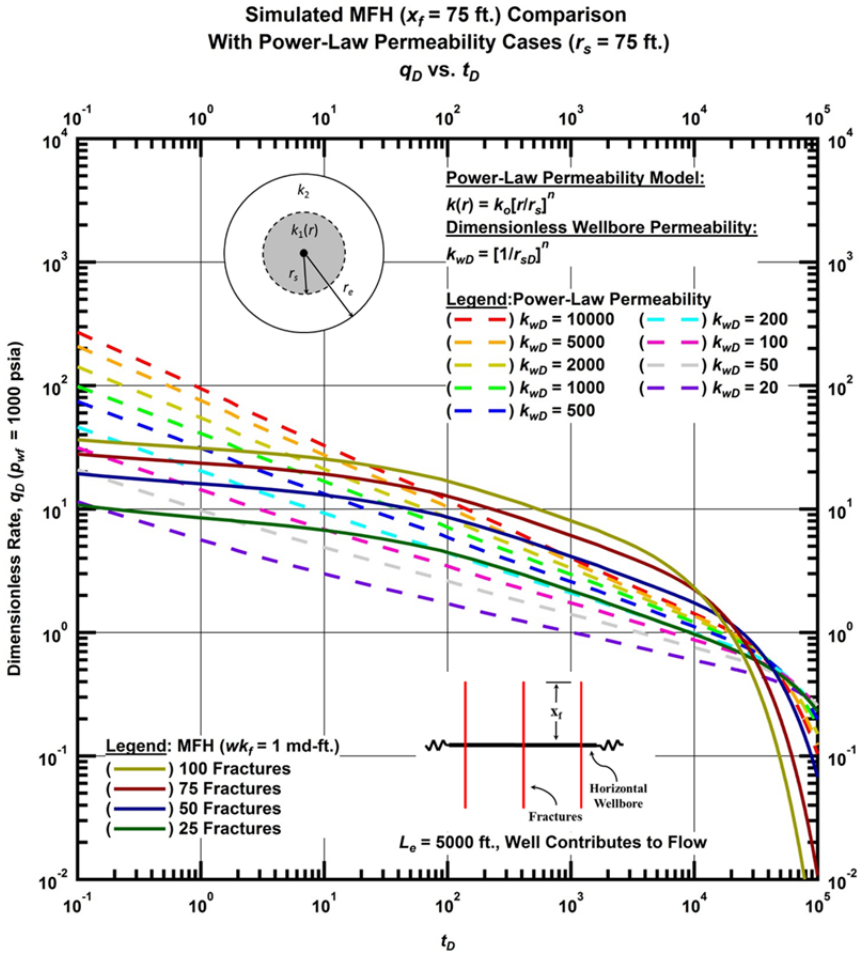

Figure 4.5 — Log-log plot of q_D vs. t_D for a PPR with r_s = 75 ft and a MFH with x_f = 75 ft and 1 md-ft fracture conductivity

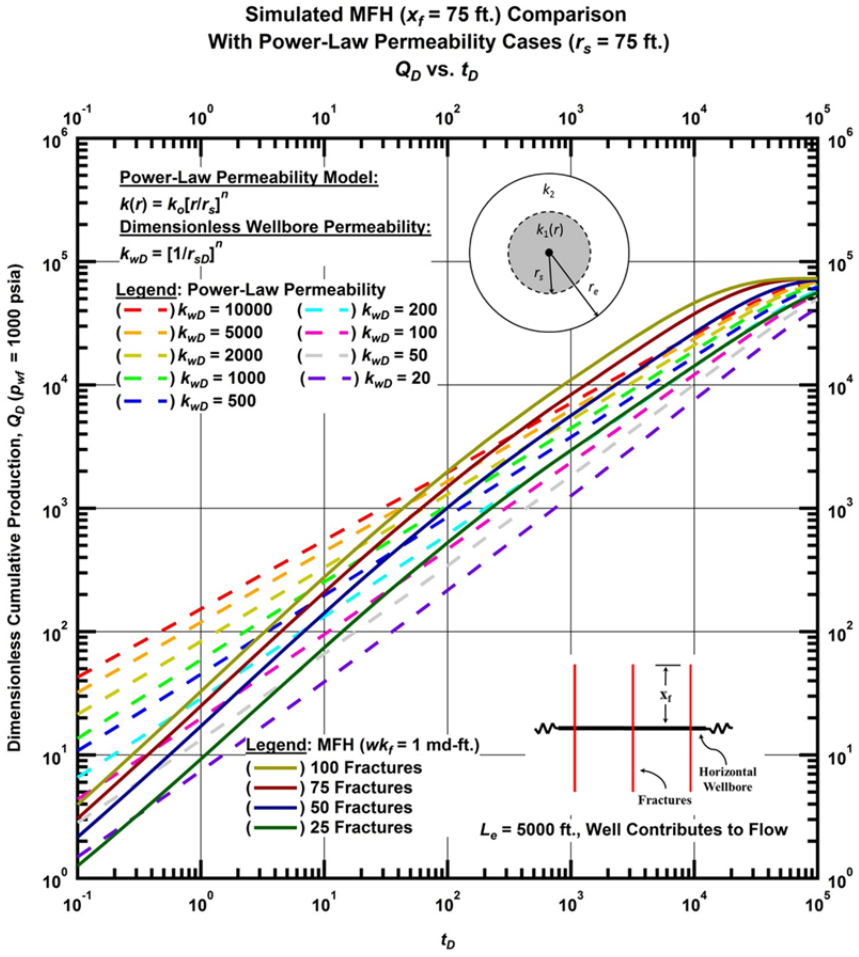

Figure 4.6 — Log-log plot of Q_D vs. t_D for a PPR with r_s = 75 ft and a MFH with x_f = 75 ft and 1 md-ft fracture conductivity

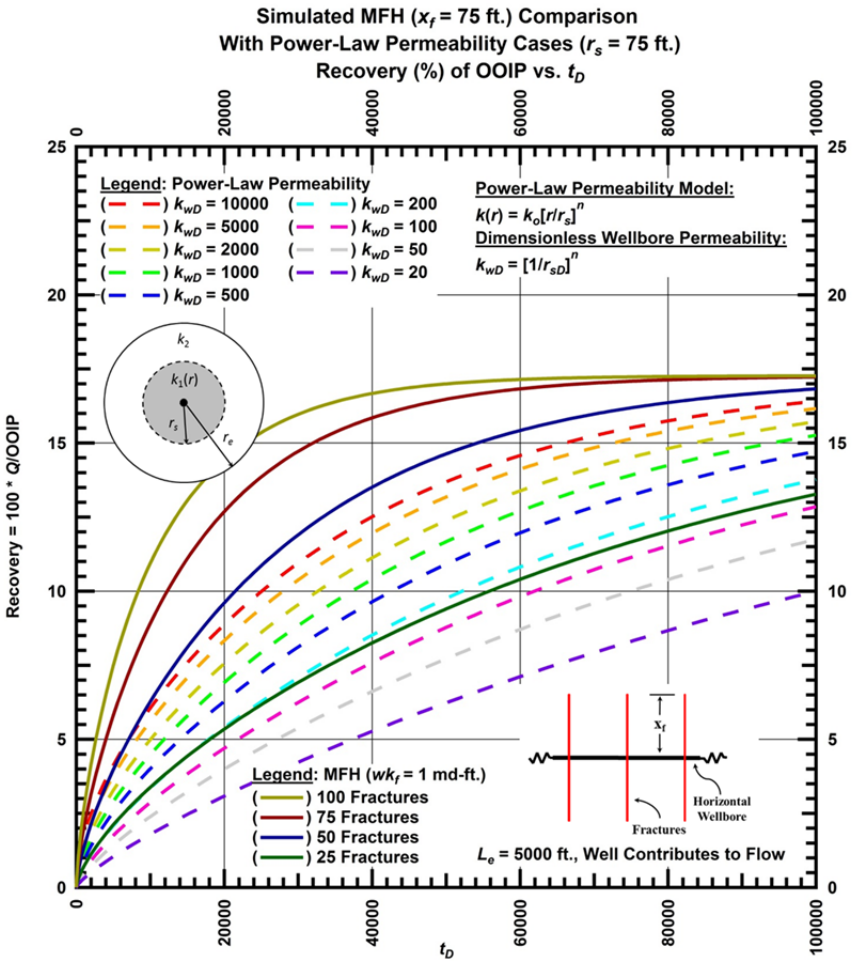

Figure 4.7 — Linear plot of RF vs. t_D for a PPR with r_s = 75 ft and a MFH with x_f = 75 ft and 1 md-ft fracture conductivity

Finally, I compare the PPR and MFH with low conductivity fractures, i.e., with a wk_f = 0.1 md-ft. As **Fig. 4.8** clearly shows, the PPR performs better than the MFH for this low fracture permeability case of wk_f. The early q_D corresponding to the PPR is a full order of magnitude larger than that for the MFH treatment (Fig. 4.8). Although the MFH rates decline much slower than the PPR (notice that formation linear flow is no longer observable as it has been in the higher conductivity comparisons), the early q_D of the PPR is so much larger that it is not until between $t_D = 10^3$ and 10^4 that the PPR q_D has declined to similar values as the MFH. The Q_D (**Fig. 4.9**) and RF (**Fig. 4.10**) show that not until late time (t_D=2*10^4), near the onset of boundary dominated flow, does the 100 fracture MFH case (the most productive MFH case) produce

volumes comparable to the *kwD* = 10000 PPR case (the most productive such case), and the 25 fracture MFH case matches k_{wD}=20 PPR case (the least productive such case). Figs. 4.8–4.10 demonstrate that the PPR with r_s=75 ft has a consistent production advantage over the MFH with a wk_f = 0.1 md-ft because of a more favorable permeability regime.

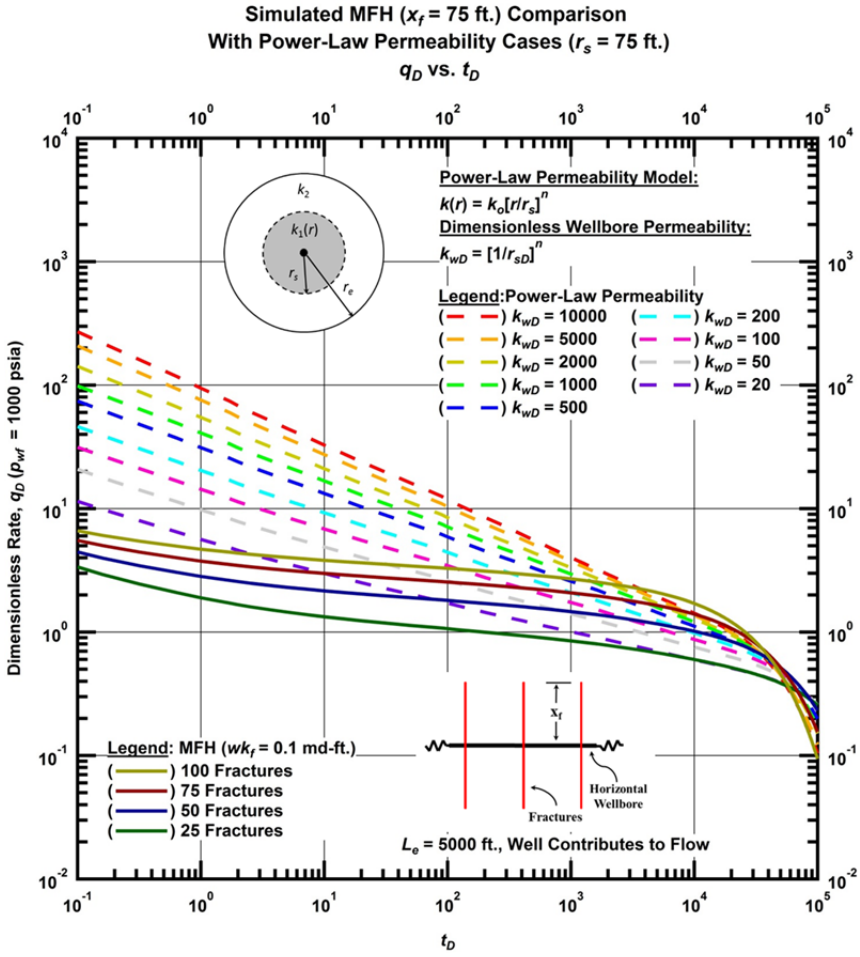

Figure 4.8 — Log-log plot of q_D vs. t_D for a PPR with r_s = 75 ft and a MFH with x_f = 75 ft and 0.1 md-ft fracture conductivity

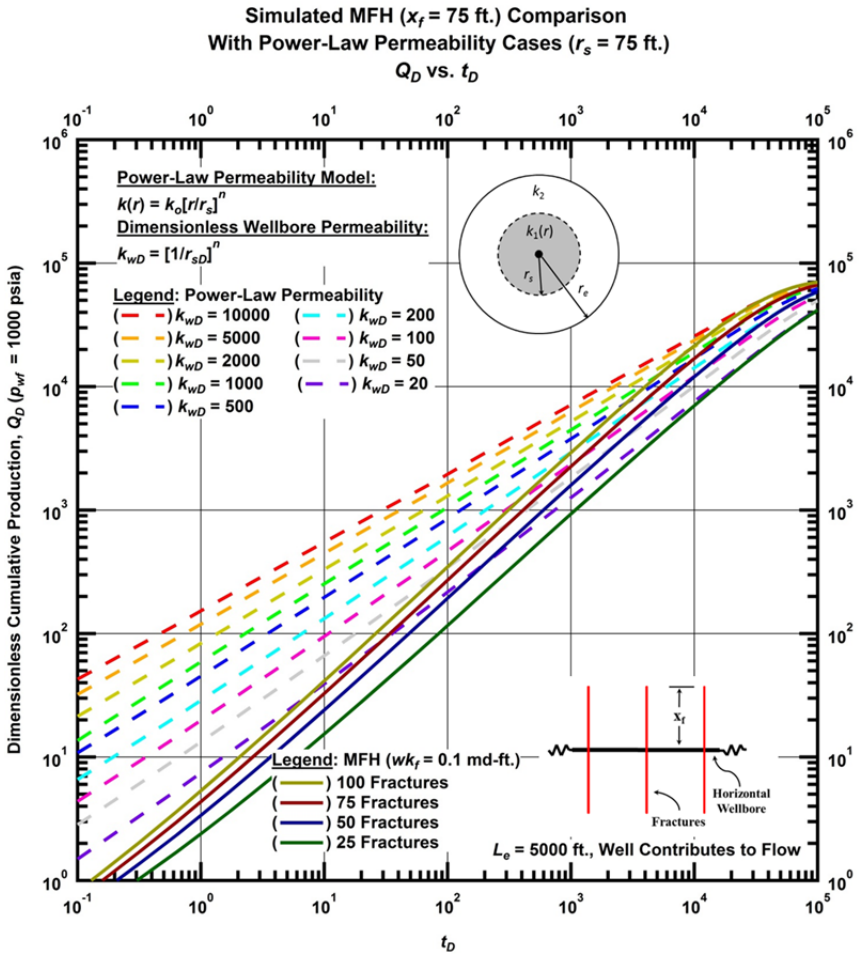

Figure 4.9 — Log-log plot of Q_D vs. t_D for a PPR with r_s = 75 ft and a MFH with x_f = 75 ft and 0.1 md-ft fracture conductivity

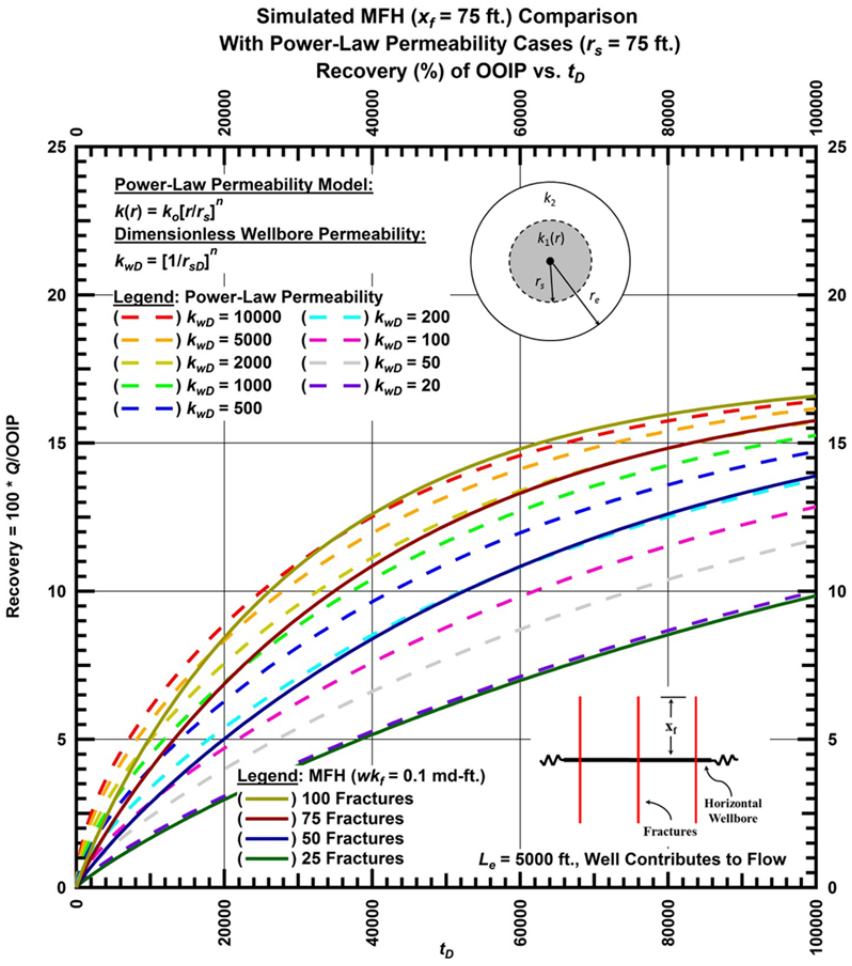

Figure 4.10 — Linear plot of RF vs. t_D for a PPR with r_s=75 ft and a MFH with x_f = 75 ft and 0.1 md-ft fracture conductivity

4.2.2 Comparison of PPR to MFH: Medium Stimulated Region

In the second set of simulations, we compare the production estimates for a PPR with r_s=50 ft (i.e., with a medium-sized stimulated cylindrical region) to those for a MFH treatment with x_f=50 ft. We follow the same evaluation approach as the previous section, progressively reducing the fracture conductivity (which are the same as in Section 4.2.1) and comparing the results. First, we compare the PPR production performance to that of an MFH treatment with wk_f =10 md-ft.

The reduction in the fracture surface area that results from the decrease of x_f from 75 to 50 ft adversely (and significantly) affected the performance of the MFH treatment compared to that of the PPR (**Figs. 4.11–4.13**). The early MHF values of q_D (Fig. 4.11) differ little from the MFH cases with x_f=75 ft and wk_f = 10 md-ft, but the smaller fracture surface area has expedited the onset of the formation linear flow (denoted by a slope of -1/2 of the q_D curve on the log-log plot). As a result, the production advantage of the 100 fracture and 75 fracture cases over the PPR has reduced significantly, but they still perform better than all PPR cases. The evolution of Q_D (**Fig. 4.12**) and RF (**Fig. 4.13**) over time show that the MFH case of fracture frequency of 50 performs similarly to the PPR case with k_{wD} = 2000, but in Section 4.2.1 (the wk_f = 10 md-ft comparison), the 50 fracture case outperformed all PPR cases. The Q_D (Fig. 4.12) and RF (Fig. 4.13) curves for a fracture frequency of 25 display an early time performance between k_{wD}=500 and k_{wD}=200 and late time behavior that appears to match the k_{wD}=50 PPR case. Clearly, the effect of the decrease in the fracture surface area in the MFH on production and recovery is more important than the effect of the reduction in stimulation radius (*rs*) of the PPR.

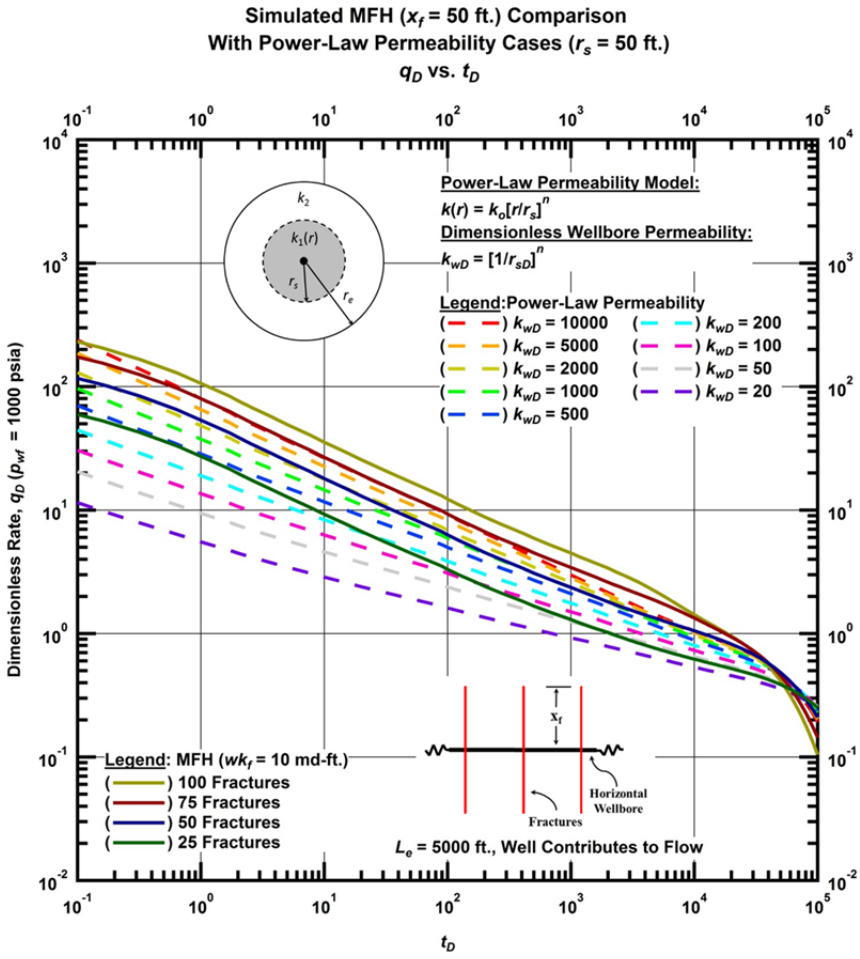

Figure 4.11 — Log-log plot of q_D vs. t_D for a PPR with r_s = 50 ft and a MFH with x_f = 50 ft and 10 md-ft fracture conductivity

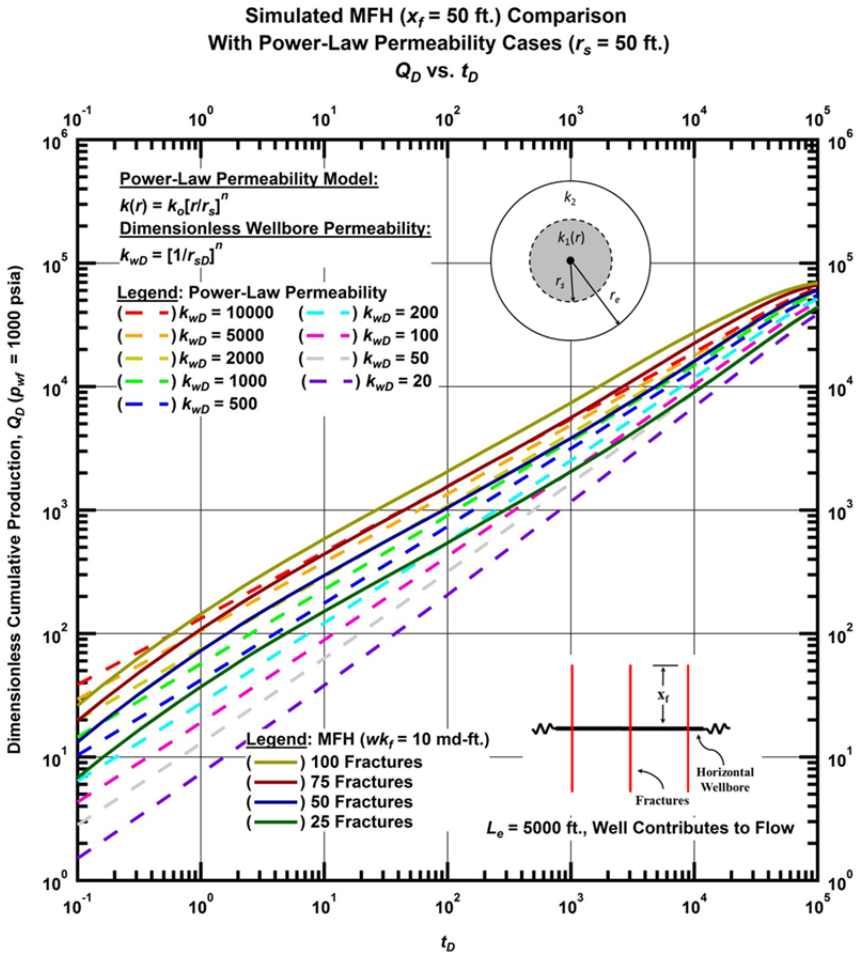

Figure 4.12 — Log-log plot of Q_D vs. t_D for a PPR with r_s = 50 ft and a MFH with x_f = 50 ft and 10 md-ft fracture conductivity

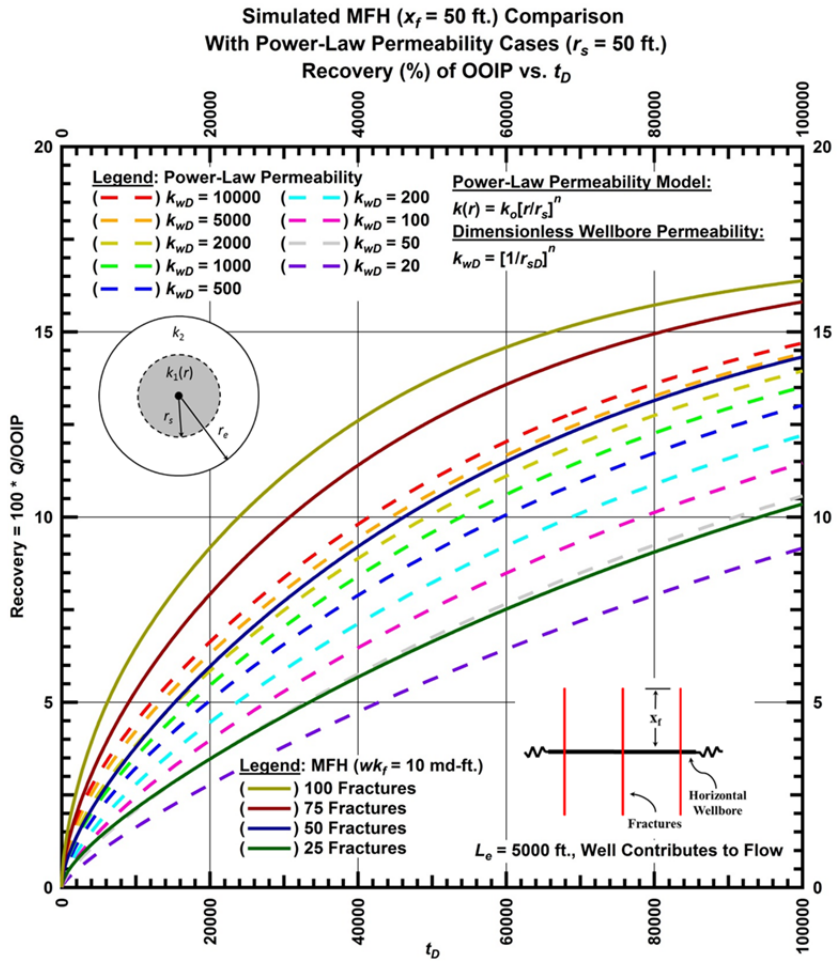

Figure 4.13 — Linear plot of RF vs. t_D for a PPR with r_s = 50 ft and a MFH with x_f = 50 ft and 10 md-ft fracture conductivity

Figs. 4.14–4.16 show the comparison between PPR and MFH with a wk_f = 1 md-ft. The reduction in fracture surface area (from x_f=75 ft in Section 4.2.1) has not affected the early time production performance (Fig. 4.14). Therefore, we can conclude that the wk_f dominates the early time q_D of the MFH. In the middle-time and late-time regions however, the reduction in x_f (or fracture surface area) has dominated the rate response, causing a significant drop in productivity. We observe that the reduction in fracture surface area has diminished the production advantage of the 100 fracture and 75 fracture cases, as seen in the Q_D (Fig. 4.15) and RF (Fig. 4.16) curves. Also, the 50 fracture case performance has reduced to

a similarity with the k_{wD}=1000 PPR case, and the 25 fractures case displays a production performance between the k_{wD}=50 and k_{wD}=20 PPR cases.

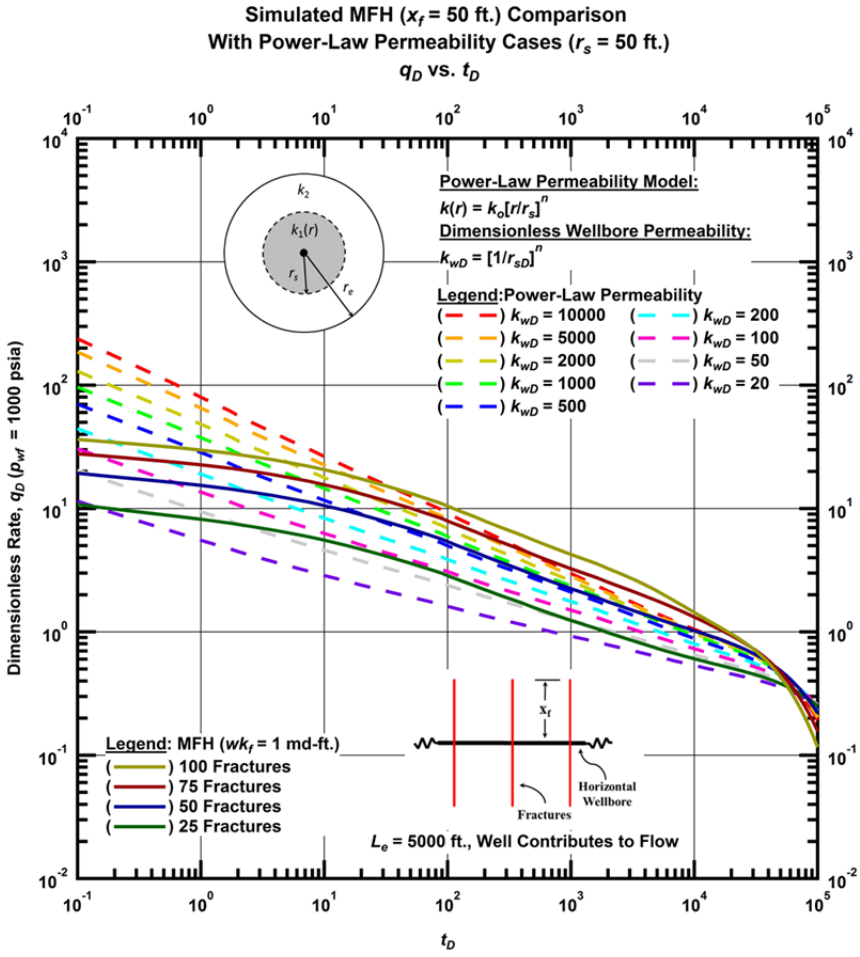

Figure 4.14 — Log-log plot of q_D vs. t_D for a PPR with r_s = 50 ft and a MFH with x_f = 50 ft and 1 md-ft fracture conductivity

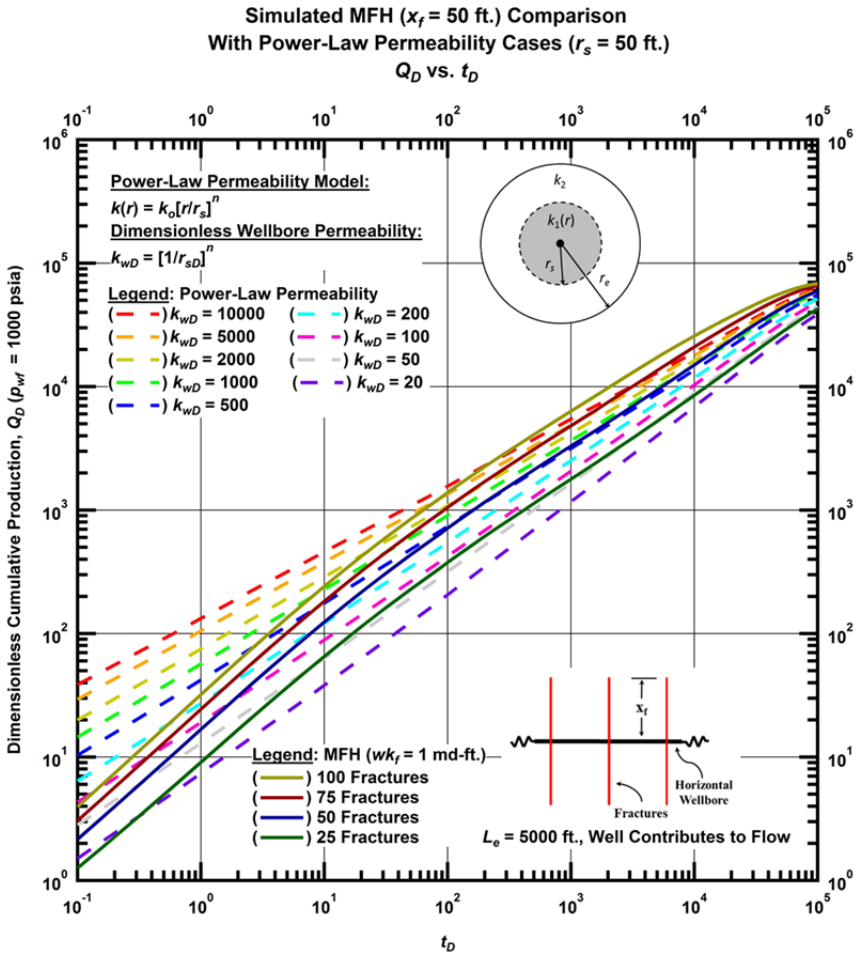

Figure 4.15 — Log-log plot of Q_D vs. t_D for a PPR with r_s = 50 ft and a MFH with x_f = 50 ft and 1 md-ft fracture conductivity

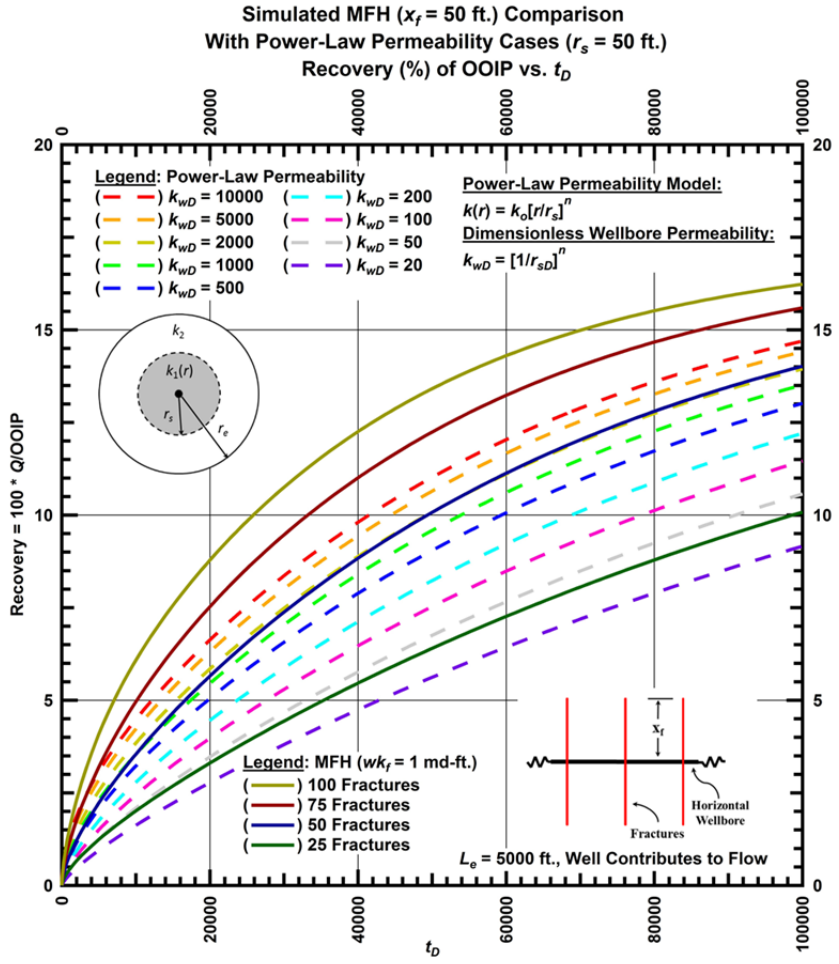

Figure 4.16 — Linear plot of RF vs. t_D for a PPR with r_s = 50 ft and a MFH with x_f = 50 ft and 1 md-ft fracture conductivity

Figs. 4.17–4.19 show the comparison between PPR and MFH with wk_f =0.1 md-ft. This comparison displays a lot of similarities with the wk_f=0.1 md-ft comparison in Section 4.2.1 (Figs. 4.8-4.10). First and most importantly, the PPR performs better than the MFH for this low fracture permeability case of wk_f. Also, the early q_D corresponding to the PPR is a full order of magnitude larger than that for the MFH treatment (Fig. 4.17), and formation linear flow is not observable. However, what we do not see is a significant effect of reducing the fracture surface area as seen in the wk_f=10 md-ft and wk_f=1 md-ft comparisons (Figs. 4.11-4.13 and Figs. 4.14-4.16 respectively). The Q_D (Fig. 4.18) and RF (Fig. 4.19) show that the fracture frequencies of 100, 75, 50 and 25 perform only marginally less than that shown in

the Q_D and RF of Fig. 4.9 and 4.10 respectively. This is because the low wk_f dominates the rate response for an extended period of time (until t_D=10^3). The fracture size (i.e., x_f) does not exert a significant influence on the MFH productivity until much later than that of the wk_f=10 md-ft (Figs. 4.11-4.13) and wk_f=1 md-ft (Figs. 4.14-4.16) comparisons.

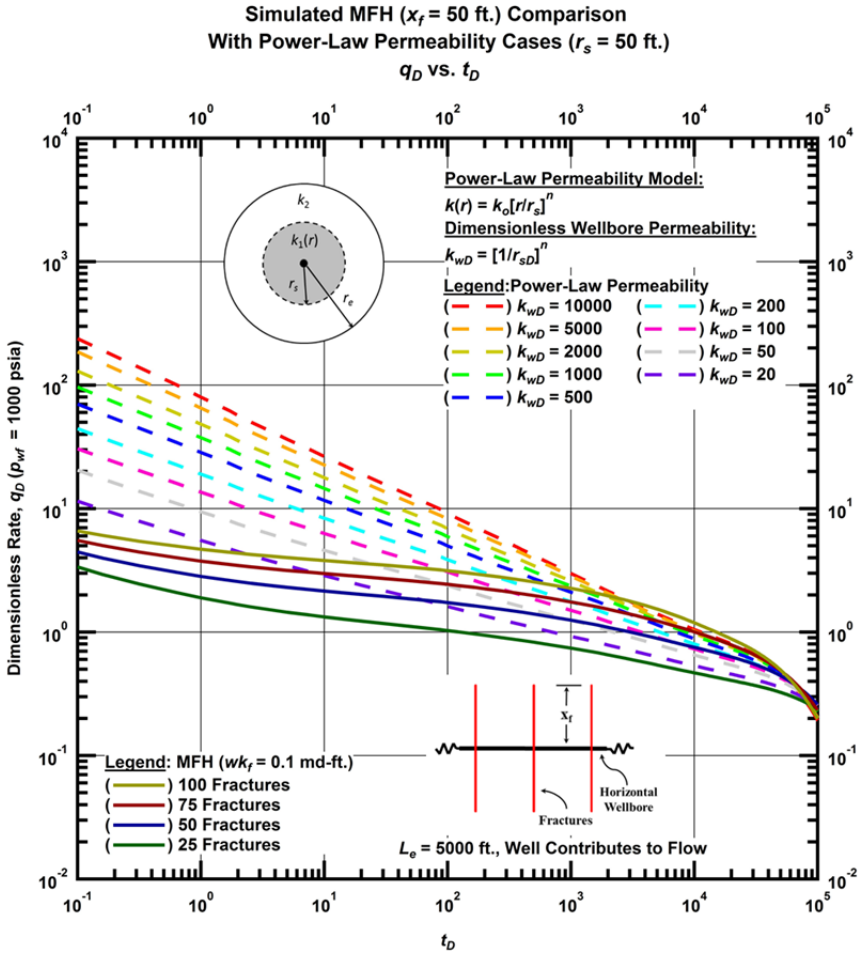

Figure 4.17 — Log-log plot of q_D vs. t_D for a PPR with r_s = 50 ft and a MFH with x_f = 50 ft and 0.1 md-ft fracture conductivity

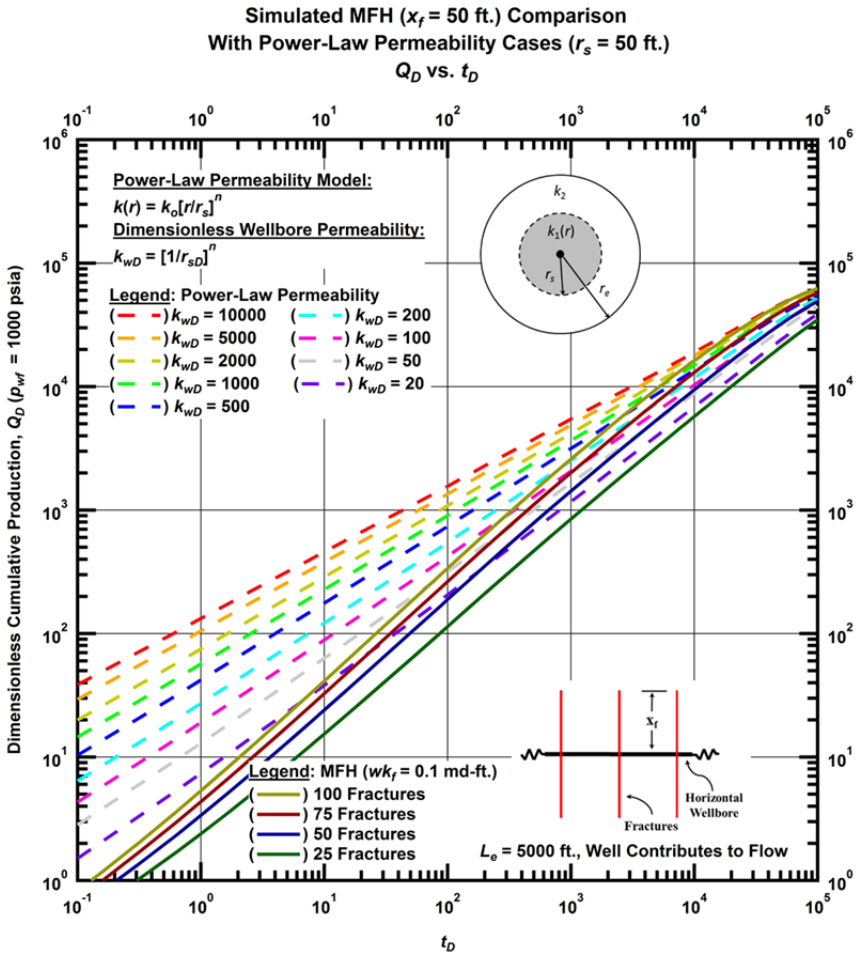

Figure 4.18 — Log-log plot of Q_D vs. t_D time for a PPR with r_s = 50 ft and a MFH with x_f = 50 ft and 0.1 md-ft fracture conductivity

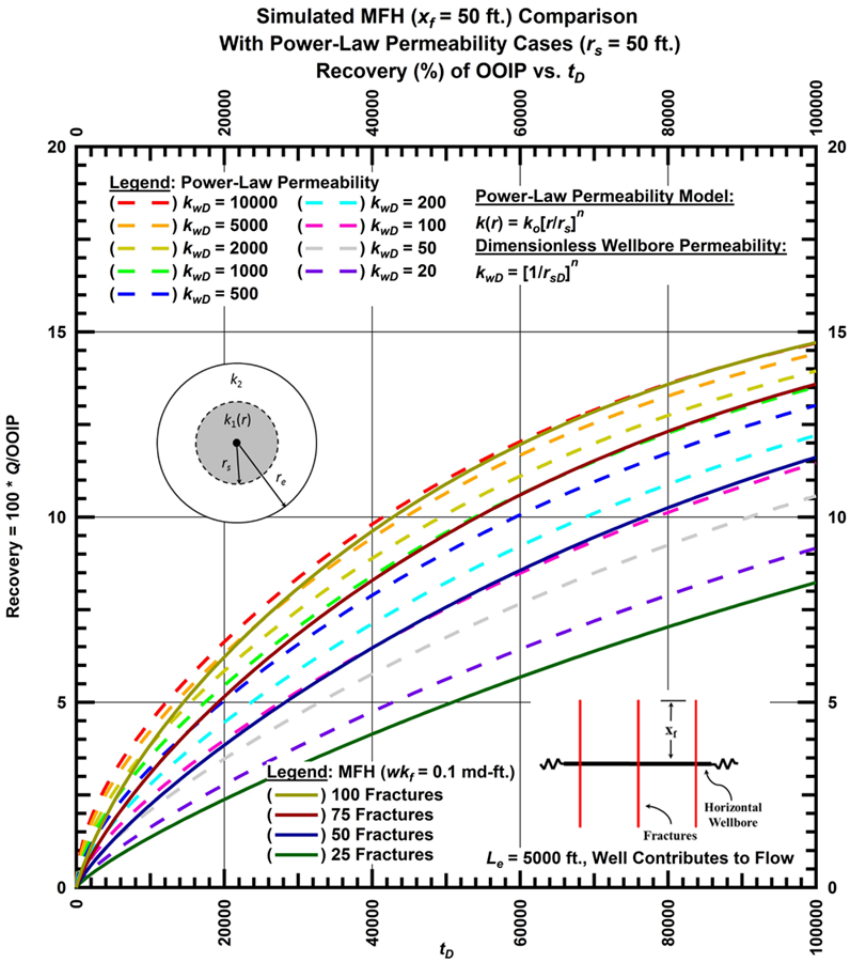

Figure 4.19 — Linear plot of RF vs. t_D for a PPR with r_s = 50 ft and a MFH with x_f = 50 ft and 0.1 md-ft fracture conductivity

4.2.3 Comparison of PPR to MFH: Small Stimulated Region

The third and final set of simulation results compares the PPR with r_s=25 ft to the MFH with x_f=25 ft. Because of the similarity in the wk_f=10 md-ft and wk_f=1 md-ft comparisons in Section 4.2.1 and Section 4.2.2, we limit the comparisons in this section to wk_f=10 md-ft and wk_f=0.1 md-ft.

The MFH q_D in **Fig. 4.20** shows evidence of formation linear flow (dq_D/dt_D = -1/2) from the very beginning. The small x_f and the high wk_f allow the low permeability matrix to quickly dominate the rate response. As a result, contrary to the results for the cases of medium and large r_s, the PPR outperforms the

MFH treatment when the stimulated region is limited (r_s=25 ft and x_f=25 ft). The PPR displays a small productivity decline because of the limited r_s and rapidly diminishing permeability, but the productivity of the PPR does not appear to be as sensitive to a change in the r_s as the MFH is to a change in x_f. The small x_f has greatly diminished the productivity of the MFH. The evolution of Q_D in **Fig. 4.21**and RF in **Fig. 4.22** shows that the fracture frequencies of 100 and 75 perform similarly to k_{wD}=2000 and k_{wD}=200 PPR cases respectively. The 50 fracture case performance is between that of the k_{wD}=50 and k_{wD}=20 PPR cases and the 25 fracture case performs well below all PPR cases.

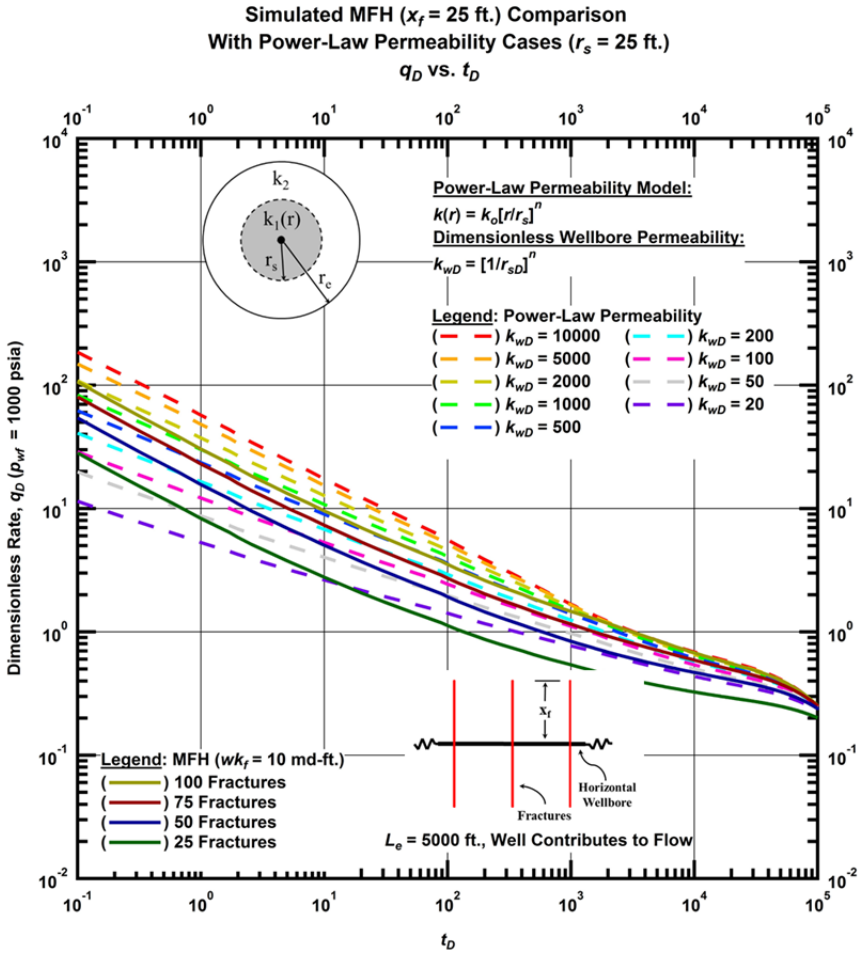

Figure 4.20 — Log-log plot of q_D vs. t_D for a PPR with r_s = 25 ft and a MFH with x_f = 25 ft and 10 md-ft fracture conductivity

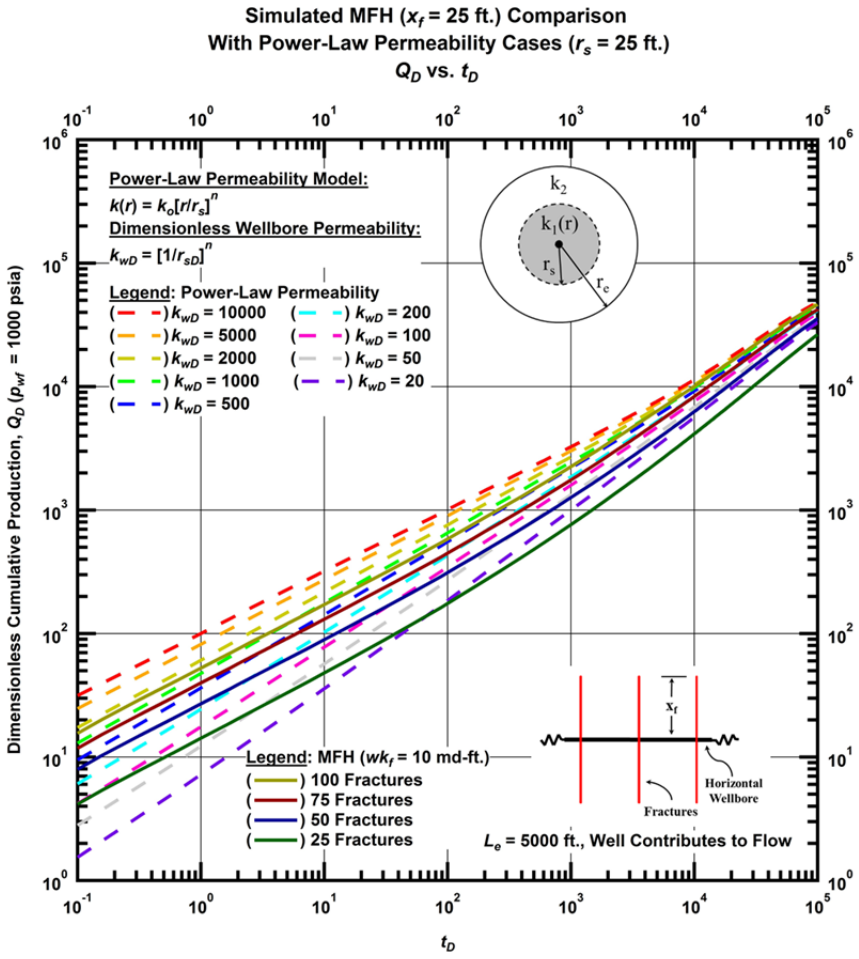

Figure 4.21 — Log-log plot of Q_D vs. t_D for a PPR with r_s = 25 ft and a MFH with x_f = 25 ft and 10 md-ft fracture conductivity

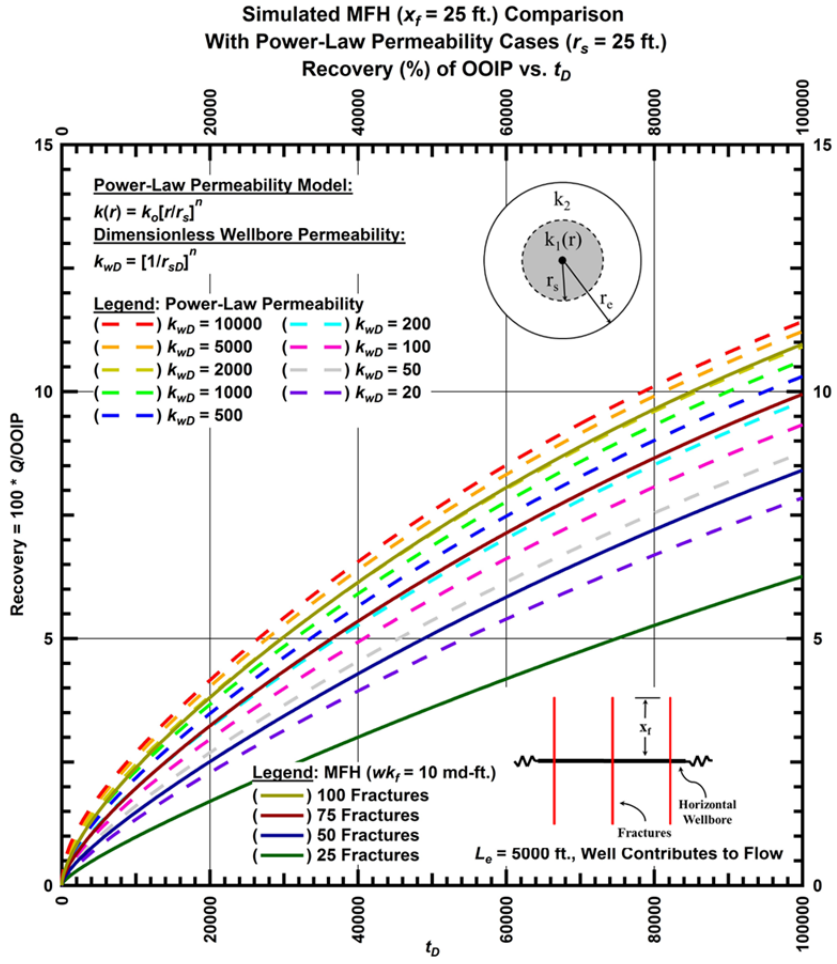

Figure 4.22 — Linear plot of RF vs. t_D for a PPR with r_s = 25 ft and a MFH with x_f = 25 ft and 10 md-ft fracture conductivity

Figs. 4.23–4.25 show the comparison between PPR and MFH with low fracture conductivity (wk_f = 0.1 md-ft). The q_D, Q_D, and RF in **Figs. 4.23, 4.24** and **4.25**, respectively, show that the PPR clearly outperforms the MFH in the case of low wk_f and small x_f. It appears that the PPR concept can be a viable and promising stimulation alternative (if it can be adequately developed in the field) when there is a hindrance or failure to develop adequate fracture conductivity or sufficient fracture surface area. When these conditions are not met, the PPR may not outperform the MFH, but it can provide respectable rates of hydrocarbon recovery from ultra-low permeability reservoirs.

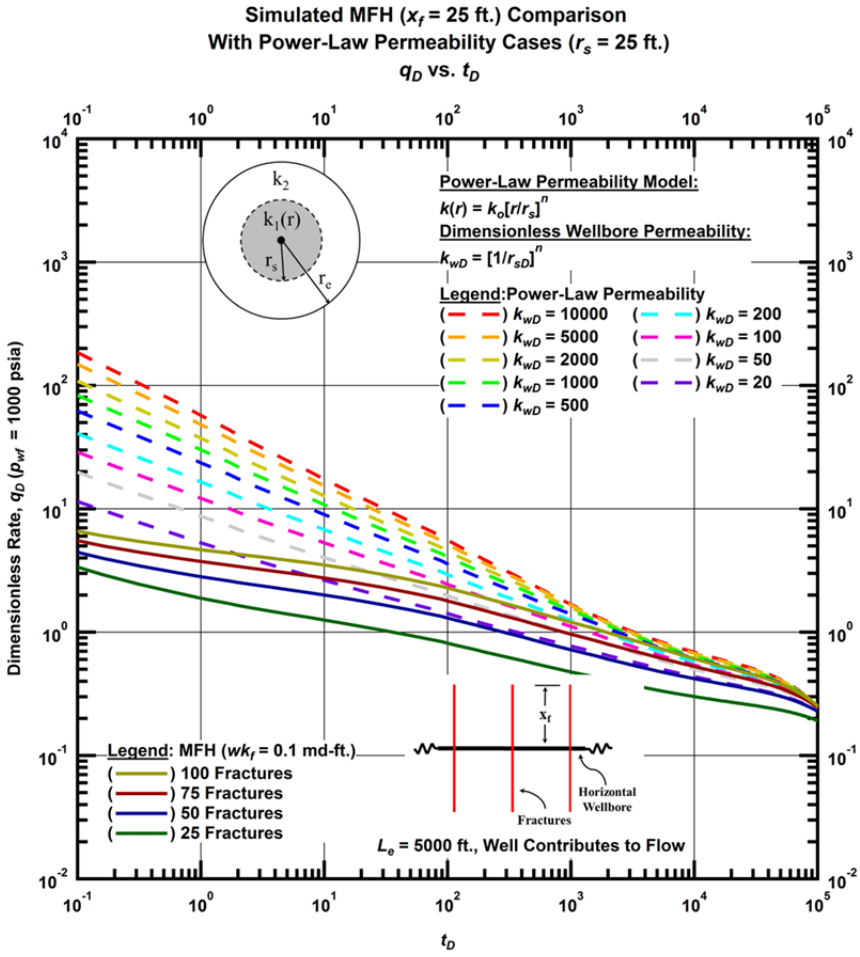

Figure 4.23 — Log-log plot of q_D vs. t_D for a PPR with r_s = 25 ft and a MFH with x_f = 25 ft and 0.1 md-ft fracture conductivity

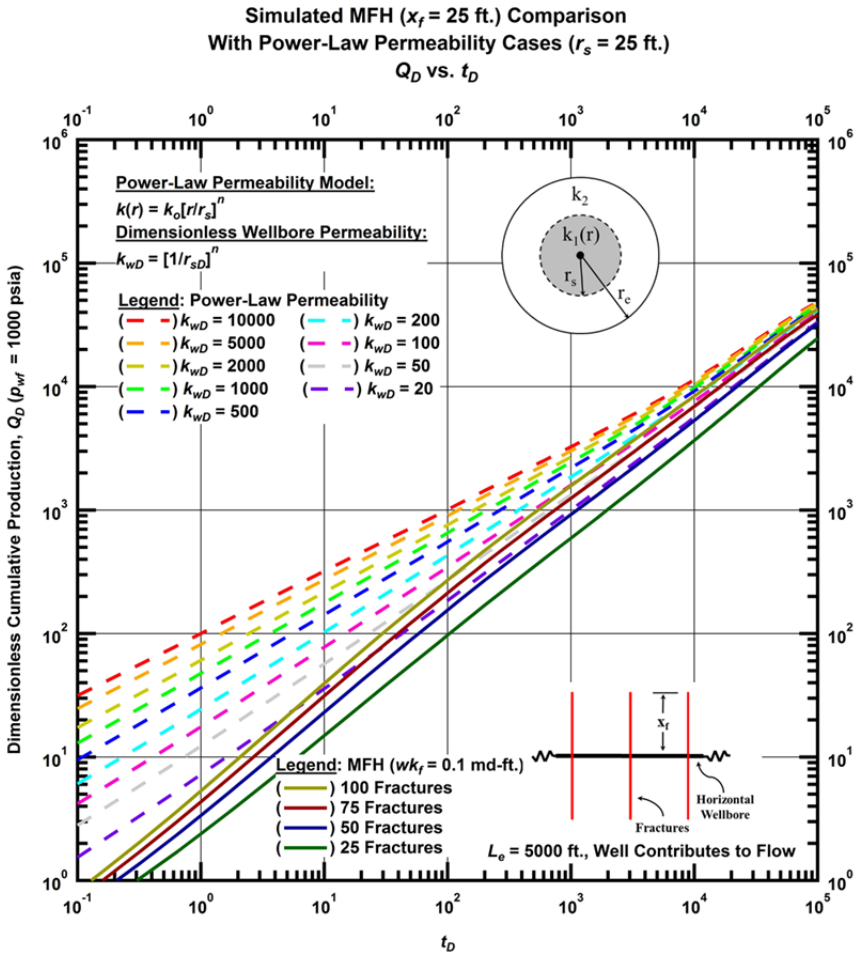

Figure 4.24 — Log-log plot of Q_D vs. t_D for a PPR with r_s = 25 ft and a MFH with x_f = 25 ft and 0.1 md-ft fracture conductivity

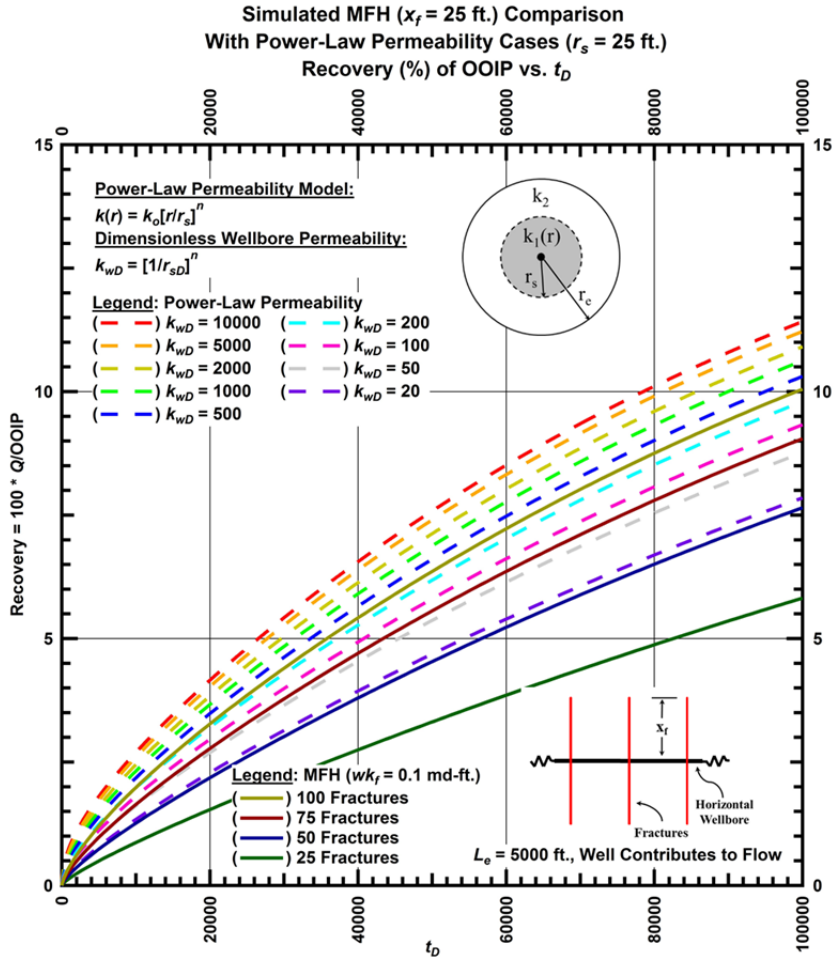

Figure 4.25 — Linear plot of RF vs. t_D for a PPR with r_s = 25 ft and a MFH with x_f = 25 ft and 0.1 md-ft fracture conductivity

5. SUMMARY, CONCLUSIONS, AND RECOMMENDATIONS

Summary:

In this work I have proposed a conceptual solution for a horizontal well with a radially propagating "power-law" permeability distribution — where this permeability distribution represents an *improvement* of the permeability. This concept model presumes that the maximum permeability is at the wellbore itself, and the minimum permeability is actually the native permeability existing at some physical distance away from the wellbore. The "power-law" permeability distribution was chosen to represent this scenario because:

- Such a distribution would seem feasible given that hydraulic, sonic, or electromagnetic pulse energy (that would be used to effect reservoir stimulation) would be expended mostly near the wellbore, hence creating the type of profile we envision.
- Similarly, a distribution such as this could also be expected from chemical alteration (*e.g.*, using acid); note that I recognize that the specific method of well acidizing would not be a viable stimulation method because it would require a long exposure and an impractically large volume of acid to substantially alter the native state permeability in a shale.
- Based on the results of literature review, I believe that the "power-law" permeability distribution should be the most conservative permeability profile that can be achieved by hydraulic, mechanical, or chemical mechanisms.

I developed both analytical and numerical solutions for this scenario, I provided validation of the analytical solution through comparison to the numerical one, and I compiled an exhaustive suite of simulation cases to provide illustrative pressure and rate behavior. I also provided numerous performance comparisons with the standard horizontal multi-fracture well case, and I gave relevant commentary as to these comparisons. In summary, the proposed case of a horizontal well with a power-law permeability distribution appears to be competitive with the standard horizontal multi-fracture well case under certain circumstances. It is important to note that, at present, there is no

known mechanism or process to generate a power-law permeability distribution around a horizontal well, but this is possible as well completion techniques continue to evolve.

Conclusions:

- The analytical dimensionless pressure and dimensionless rate solutions derived for the case of a radial composite reservoir with a power-law permeability distribution in the inner region were solved in the Laplace domain and numerically inverted into the real domain using the Gaver-Wynn-Rho algorithm implemented in *Mathematica* (Valkó and Abate 2004; Abate and Valkó 2004). These solutions are considered to be "analytically" accurate (*i.e.*, near exact) and are presented in terms of dimensionless time and dimensionless distance in order to illustrate the relevant features of the proposed model.
- I have validated the analytical dimensionless pressure (p_D) and dimensionless rate (q_D) solutions by comparing them to numerical simulation predictions. The results show excellent agreement between the analytical and numerical solutions. There are negligible divergences in the dimensionless pressure solutions at radial distances far from the wellbore where the pressure is approaching that of the initial reservoir pressure, and there are slight divergences in the dimensionless rate solutions for low stimulation cases (low k_{wD}) because of insufficient grid discretization near the wellbore. The ultra-low permeability of the reservoir requires extremely small grids close to the wellbore where the pressure and permeability change is greatest.
- I observed that the slope of the dimensionless pressure derivative (in terms of dimensionless radius) yields the power-law exponent (n) of the power-law permeability distribution in the inner stimulated zone. This rendering also yields a horizontal trend during the times where the pressure transients have moved into the outer (constant permeability) region. However, if the stimulated region extends close to the reservoir outer boundary, pseudosteady-state will be observed (as would be expected).
- I observed that, when comparing the "power-law permeability reservoir" (or PPR) and the "multi-fracture horizontal" (MFH) cases, it appears that a change in the magnitude of the stimulation affects the MFH significantly more than the PPR. The primary advantage of the MFH is that this

method creates a tremendous amount of surface area by way of the fractures. Increasing or decreasing the fracture size has a profound effect on the fracture surface area and thus the effectiveness of the stimulation. However, the productivity of the PPR does not appear to be as sensitive to a change in the PPR stimulation radius (r_s). If the dimensionless wellbore permeability (k_{wD}) remains the same, then reducing the stimulation radius (r_s) increases the power-law exponent (n) and accelerates the rate of permeability decline. This change in the permeability distribution does not affect the PPR as significantly as a change in fracture size affects the MFH.

- Comparing the MFH and PPR cases, the PPR presents a performance advantage over the MFH when the fracture conductivity and fracture half-length are small. As such, I believe our results provide sufficient evidence to conclude that the PPR stimulation concept is suitable for the efficient recovery of hydrocarbons from ultra-low permeability reservoirs.

Recommendations:

Based on the results of this study, I recommend the following areas as subject for future work:

- The cases of a "linear" and an "exponential" permeability propagation trend. As I have stated, I believe that the power-law case is the most conservative permeability profile, so it is warranted to consider other profiles, particularly in light of the fact that stimulation technology may provide a substantially better permeability profile than currently envisioned.
- The effects of pressure-dependent porosity and permeability profiles in the inner cylindrical region.

NOMENCLATURE

B = formation volume factor, L^3/L^3, res bbl/STB

c_t = total compressibility, Lt^2/m, atm

I_x = modified Bessel function of the first kind of order x

k_D = ratio of permeability at the wellbore to original reservoir permeability, dimensionless

k_o = original permeability of the reservoir, L^2, D

k_r = permeability in the radial direction, L^2, D

k_w = permeability at the wellbore, L^2, D

K_x = modified Bessel function of the second kind of order x

L_e = Length of the reservoir/wellbore in the z-direction, L, cm

n = power-law model exponent, dimensionless

p = pressure, m/Lt^2, atm

p_D = dimensionless pressure, dimensionless

p_{wD} = dimensionless pressure at the wellbore, dimensionless

$\overline{p}_D$ = Laplace transform of dimensionless pressure, dimensionless

p_i = initial reservoir pressure, m/Lt^2, atm

p_w = bottomhole pressure, m/Lt^2, atm

Q = cumulative production, L^3, cm^3

q = liquid flow rate, L^3/t, cm^3/s

Q_D = dimensionless cumulative production, dimensionless

q_D = dimensionless liquid flow rate, dimensionless

r = radial distance in the reservoir, L, cm

r_D = dimensionless radius, dimensionless

r_e = radial extent of the reservoir, L, cm

r_{eD} = dimensionless reservoir radius, dimensionless

r_s = radial extent of the stimulated zone, L, cm

r_{sD} = dimensionless stimulation radius, dimensionless

r_w = radius of the wellbore, L, cm

s = Laplace parameter, dimensionless

t = time, t, s

t_D = dimensionless time, dimensionless

r = Effective pore radius of the considered porous medium, length.

μ = Liquid viscosity, cp.

ϕ = porosity, fraction

REFERENCES

Abate, J. and Valkó, P.P. 2004. Multi-precision Laplace Transform Inversion. *International Journal for Numerical Methods in Engineering.* **60**: 979-993.

Arthur, D.J., Bohm, B., and Layne, M. 2008. Hydraulic Fracturing Considerations for Natural Gas Wells of the Marcellus Shale. GWCP Report presented at The Ground Water Protection Council 2008 Annual Forum, Cincinnati, Ohio, 21-24 September.

Bixel, H.C. and van Poollen, H.K. 1967. Pressure Drawdown and Buildup in the Presence of Radial Discontinuities. *SPE J.* **7** (3): 301-09. SPE-1516-PA. http://dx.doi.org/10.2118/1516-PA.

Bowman, F. 1958. *Introduction to Bessel Functions*, first edition. New York, New York: Dover Publications Inc.

Callard, J.G. and Schenewerk, P.A. 1995. Reservoir Performance History Matching Using Rate/Cumulative Type-Curves, Paper SPE 30793 presented at the SPE Annual Technical Conference and Exhibition, Dallas, U.S.A., 22-25 October. SPE-30793-MS. http://dx.doi.org/10.2118/30793-MS.

Carter, E.E. 2009. Novel Concepts for Unconventional Gas Development of Gas Resources in Gas Shales, Tight Sands and Coalbeds. RPSEA 07122-7, Carter Technologies Co., Sugar Land, Texas (19 February 2009).

Carter, R.D. 1966. Pressure Behavior of a Limited Circular Composite Reservoir. *SPE J.* **6** (4): 328-334. SPE-1621-PA. http://dx.doi.org/10.2118/1621-PA.

El-Khatib, N.A.F. 2009. Transient Pressure Behavior for a Reservoir With Continuous Permeability Distribution in the Invaded Zone, Paper SPE 120111 presented at the SPE Middle East Oil and Gas Show and Conference, Kingdom of Bahrain, 15-18 March. SPE-120111-MS. http://dx.doi.org/10.2118/120111-MS.

ORD. 2011. Draft Plan to Study the Potential Impacts of Hydraulic Fracturing on Drinking Water Resources, US EPA, Office of Research and Development, Washington, D.C. (7 February 2011).

Freeman, C.M. 2010. Study of Flow Regimes in Multiply-Fractured Horizontal Wells in Tight Gas and Shale Gas Reservoir Systems. MS thesis, Texas A&M University, College Station, Texas (May 2010).

Hefley, W.E., Seydor, S.M., Bencho, M.K.., et al. 2011. The Economic Impact of the Value Chain of a Marcellus Shale Well, Katz Graduate School of Business, University of Pittsburgh, Pittsburgh, Pennsylvania (30 August 2011).

Hurst, W. 1960. Interference Between Oil Fields, In *Transactions of the Society of Petroleum Engineers*, Vol. 219, 175-192. SPE-1335-G. http://dx.doi.org/10.2118/1335-G.

Loucks, T.L. and Guerrero, E.T. 1961. Pressure Drop in a Composite Reservoir. *SPE J.* **1** (3): 170-176. SPE-19-PA. http://dx.doi.org/10.2118/19-PA.

Mathematica (software), version 8.0. 2010. Wolfram Research, Champaign-Urbana, Illinois.

Montgomery, C.T. and Smith, M.B. 2010. Hydraulic Fracturing: History of an Enduring Technology. *J. Pet. Tech.* **62** (12): 26-32.

Moridis, G.J., Blasingame, T.A., and Freeman, C.M. 2010. Analysis of Mechanisms of Flow in Fractured Tight-Gas and Shale-Gas Reservoirs, Paper SPE 139250 presented at the SPE Latin American and Caribbean Petroleum Engineering Conference, Lima, Peru, 1-3 December. SPE-139250-MS. http://dx.doi.org/10.2118/139250-MS.

Moridis, G.J., Kowalsky, M.B., and Pruess, K. 2008.TOUGH+HYDRATE v1.0 User's Manual: A Code for the Simulation of System Behavior in Hydrate-Bearing Geologic Media. Report LBNL-00149E, Lawrence Berkeley National Laboratory, Berkeley, CA.

Mortada, M. 1960. Oilfield Interference in Aquifers of Non-Uniform Properties, In *Transactions of the Society of Petroleum Engineers*, Vol. 219, 412. SPE-1507-G. http://dx.doi.org/10.2118/1507-G.

Mursal. 2002. A New Approach For Interpreting a Pressure Transient Test After a Massive Acidizing Treatment. MS thesis, Texas A&M University, College Station, Texas (December 2002).

Ramey, H.J. 1970. Approximate Solutions For Unsteady Liquid Flow in Composite Reservoirs. *J. Cdn. Pet. Tech.* **9** (1). SPE-70-01-04. http://dx.doi.org/10.2118/70-01-04.

Satman, A., Eggenschwiler, M., and Ramey, H.J. 1980. Interpretation of Injection Well Pressure Transient Data in Thermal Oil Recovery. Paper SPE 8908 presented at the SPE California Regional Meeting, Los Angeles, California, 9-11 April. SPE-8908-MS. http://dx.doi.org/10.2118/8908-MS.

Texas Tech University. 2011. Dr. M. Rafiqul Awal, http://www.depts.ttu.edu/pe/dept/facstaff/awal/ (accessed 31 October)

United States Energy Information Administration (US EIA). 2012. U.S. Crude Oil, Natural Gas, and NG Liquids Proved Reserves, http://www.eia.gov/naturalgas/crudeoilreserves/index.cfm (accessed 31 October)

Valkó, P.P. and Abate, J. 2004. Comparison of Sequence Accelerators for the Gaver Method of Numerical Laplace Transform Inversion. *Computers and Mathematics with Application* **48**: 629-636.

van Everdingen, A.F. and Hurst, W. 1949. The Application of the Laplace Transformation to Flow Problems in Reservoirs. *J. Pet. Tech.* **1** (12): 305-324. SPE-949305-G. http://dx.doi.org/10.2118/949305-G.

Wilson, B. 2003. Modeling of Performance Behavior in Gas Condensate Reservoirs Using a Variable Mobility Concept. MS thesis, Texas A&M University, College Station, Texas (December 2003).

Zhang, L., Dusseault, M.B., and Xu, B. 2006. New Method to Estimate Damaged Formation Permeability with Well Testing. Paper SPE 98200 presented at the 2006 SPE International Symposium and Exhibition on Formation Damage Control, Lafayette, Louisiana, 15-17 February. SPE-98200-MS. http://dx.doi.org/10.2118/98200-MS.

APPENDIX A

DERIVATION OF THE ANALYTICAL SOLUTION

In this Appendix, I derive an analytical representation of the pressure behavior in time and space for a fully-penetrating horizontal well (i.e. the well length is equal to the reservoir length) producing at a constant rate in the center of a composite, cylindrical reservoir system. The composite reservoir consists of two regions. The inner region, closest to the wellbore, is stimulated and exhibits a continuous permeability distribution with the highest permeability achieved at the wellbore. The distribution follows a power law function, decreasing to original reservoir permeability at the outer boundary of the inner region. The outer region is unstimulated and has homogenous reservoir properties. Mathematically, I describe this composite system by writing two governing equations for fluid flow in porous media known as diffusivity equations, one for each region:

- Stimulated Volume

$$\frac{1}{r}\frac{\partial}{\partial r}\left[k_r r\frac{\partial p_1}{\partial r}\right]=\phi\mu c_t\frac{\partial p_1}{\partial t}\ \text{(Darcy units)} \quad \text{(A-1)}$$

- Unstimulated Volume

$$\frac{1}{r}\frac{\partial}{\partial r}\left[k_o r\frac{\partial p_2}{\partial r}\right]=\phi\mu c_t\frac{\partial p_2}{\partial t}\ \text{(Darcy units)} \quad \text{(A-2)}$$

The significant assumptions involved in the construction of Eqs. A-1 and A-2 are:

- Slightly compressible liquid
- Single-phase Darcy flow
- Constant formation porosity and liquid viscosity
- Gravity effects are neglected
- Horizontal wellbore penetrates and produces along the entire length of the reservoir (radial flow only)

The outer boundaries of the reservoir are all sealed, and the well produces at a constant rate. The pressure before production (*t=0*) in the stimulated and unstimulated volume is uniform and equal to p_i. Also, the pressure and flux across the interface between the stimulated and unstimulated volumes are continuous. Mathematically, the stated boundary and initial conditions are represented by the following equations:

- Initial Conditions (uniform pressure at time zero):

$$p_1(r,t)\big|_{t=0}=p_2(r,t)\big|_{t=0}=p_i \quad \text{(A-3)}$$

- Outer Boundary Condition (no flow outer boundary):

$$\left[r \frac{\partial p_2}{\partial r} \right]_{r=r_e} = 0 \quad \text{(A-4)}$$

- Inner Boundary Condition (constant flow rate):

$$\left[r \frac{\partial p_1}{\partial r} \right]_{r=r_w} = \frac{1}{2\pi} \frac{qB\mu}{k_r L_e} \quad \text{(A-5)}$$

- Interface Condition (continuous pressure across the interface):

$$[p_1]_{r=r_s} = [p_2]_{r=r_s} \quad \text{(A-6)}$$

- Interface Condition (continuous flux across the interface):

$$\left[\frac{\partial p_1}{\partial r} \right]_{r=r_s} = \left[\frac{\partial p_2}{\partial r} \right]_{r=r_s} \quad \text{(A-7)}$$

I need to transform the diffusivity equations, initial and boundary conditions into dimensionless form. I define the following dimensionless variables from the conditions of the problem (i.e. uniform pressure initial condition and constant flow rate inner boundary condition) and using intuitive definitions:

$$r_D = \frac{r}{r_w} \quad \text{(A-8)}$$

$$r_{sD} = \frac{r_s}{r_w} \quad \text{(A-9)}$$

$$r_{eD} = \frac{r_e}{r_w} \quad \text{(A-10)}$$

$$p_D = 2\pi \frac{k_o L_e}{qB\mu} (p_i - p) \quad \text{(A-11)}$$

$$t_D = \frac{k_o t}{\phi \mu c_t r_w^2} \quad \text{(A-12)}$$

First, I will transform Eq. A-1 and A-2 into dimensionless form followed by the conditions of the problem. Solving Eq. A-8 for *r* and substituting into Eq. A-1 and A-2 I have:

- Stimulated Volume

$$\frac{1}{(r_w r_D)}\frac{\partial}{\partial(r_w r_D)}\left[k_r(r_w r_D)\frac{\partial p_1}{\partial(r_w r_D)}\right]=\phi\mu c_t\frac{\partial p_1}{\partial t} \quad \text{(A-13)}$$

- Unstimulated Volume

$$\frac{1}{(r_w r_D)}\frac{\partial}{\partial(r_w r_D)}\left[k_o(r_w r_D)\frac{\partial p_2}{\partial(r_w r_D)}\right]=\phi\mu c_t\frac{\partial p_2}{\partial t} \quad \text{(A-14)}$$

Factoring out the r_w terms from inside the derivatives and simplifying gives

- Stimulated Volume

$$\frac{1}{r_w^2 r_D}\frac{\partial}{\partial r_D}\left[k_r r_D\frac{\partial p_1}{\partial r_D}\right]=\phi\mu c_t\frac{\partial p_1}{\partial t} \quad \text{(A-15)}$$

- Unstimulated Volume

$$\frac{1}{r_w^2 r_D}\frac{\partial}{\partial r_D}\left[k_o r_D\frac{\partial p_2}{\partial r_D}\right]=\phi\mu c_t\frac{\partial p_2}{\partial t} \quad \text{(A-16)}$$

Multiplying both sides of Eq. A-15 and A-16 by r_w^2 results in

- Stimulated Volume

$$\frac{1}{r_D}\frac{\partial}{\partial r_D}\left[k_r r_D\frac{\partial p_1}{\partial r_D}\right]=\phi\mu c_t r_w^2\frac{\partial p_1}{\partial t} \quad \text{(A-17)}$$

- Unstimulated Volume

$$\frac{1}{r_D}\frac{\partial}{\partial r_D}\left[k_o r_D\frac{\partial p_2}{\partial r_D}\right]=\phi\mu c_t r_w^2\frac{\partial p_2}{\partial t} \quad \text{(A-18)}$$

Solving Eq. A-11 for p and substituting into Eq. A-17 and A-18 provides

- Stimulated Volume

$$\frac{1}{r_D}\frac{\partial}{\partial r_D}\left[k_r r_D\frac{\partial}{\partial r_D}\left(p_i-\frac{1}{2\pi}\frac{qB\mu}{k_o L_e}p_{D1}\right)\right]=\phi\mu c_t r_w^2\frac{\partial}{\partial t}\left(p_i-\frac{1}{2\pi}\frac{qB\mu}{k_o L_e}p_{D1}\right) \quad \text{(A-19)}$$

- Unstimulated Volume

$$\frac{1}{r_D}\frac{\partial}{\partial r_D}\left[k_o r_D \frac{\partial}{\partial r_D}\left(p_i - \frac{1}{2\pi}\frac{qB\mu}{k_o L_e} p_{D2}\right)\right] = \phi\mu c_t r_w^2 \frac{\partial}{\partial t}\left(p_i - \frac{1}{2\pi}\frac{qB\mu}{k_o L_e} p_{D2}\right) \quad \text{(A-20)}$$

Expanding the derivatives of the pressure terms gives

- Stimulated Volume

$$\frac{1}{r_D}\frac{\partial}{\partial r_D}\left[k_r r_D \frac{\partial}{\partial r_D}(p_i) - k_r r_D \frac{1}{2\pi}\frac{qB\mu}{k_o L_e}\frac{\partial p_{D1}}{\partial r_D}\right] = \phi\mu c_t r_w^2 \frac{\partial}{\partial t}(p_i) - \phi\mu c_t r_w^2 \frac{1}{2\pi}\frac{qB\mu}{k_o L_e}\frac{\partial p_{D1}}{\partial t} \quad \text{(A-21)}$$

- Unstimulated Volume

$$\frac{1}{r_D}\frac{\partial}{\partial r_D}\left[k_o r_D \frac{\partial}{\partial r_D}(p_i) - k_o r_D \frac{1}{2\pi}\frac{qB\mu}{k_o L_e}\frac{\partial p_{D2}}{\partial r_D}\right] = \phi\mu c_t r_w^2 \frac{\partial}{\partial t}(p_i) - \phi\mu c_t r_w^2 \frac{1}{2\pi}\frac{qB\mu}{k_o L_e}\frac{\partial p_{D2}}{\partial t} \quad \text{(A-22)}$$

Recognizing that the derivative of a constant is equal to zero, Eq. A-21 and A-22 simplifies to

- Stimulated Volume

$$\frac{1}{r_D}\frac{\partial}{\partial r_D}\left[-k_r r_D \frac{1}{2\pi}\frac{qB\mu}{k_o L_e}\frac{\partial p_{D1}}{\partial r_D}\right] = -\phi\mu c_t r_w^2 \frac{1}{2\pi}\frac{qB\mu}{k_o L_e}\frac{\partial p_{D1}}{\partial t} \quad \text{(A-23)}$$

- Unstimulated Volume

$$\frac{1}{r_D}\frac{\partial}{\partial r_D}\left[-k_o r_D \frac{1}{2\pi}\frac{qB\mu}{k_o L_e}\frac{\partial p_{D2}}{\partial r_D}\right] = -\phi\mu c_t r_w^2 \frac{1}{2\pi}\frac{qB\mu}{k_o L_e}\frac{\partial p_{D2}}{\partial t} \quad \text{(A-24)}$$

Factoring out constants from the derivative terms and simplifying further, I have

- Stimulated Volume

$$\frac{1}{r_D}\frac{\partial}{\partial r_D}\left[k_r r_D \frac{\partial p_{D1}}{\partial r_D}\right] = \phi\mu c_t r_w^2 \frac{\partial p_{D1}}{\partial t} \quad \text{(A-25)}$$

- Unstimulated Volume

$$\frac{1}{r_D}\frac{\partial}{\partial r_D}\left[k_o r_D \frac{\partial p_{D2}}{\partial r_D}\right] = \phi\mu c_t r_w^2 \frac{\partial p_{D2}}{\partial t} \quad \text{(A-26)}$$

Solving Eq. A-12 for *t* and substituting into Eq. A-25 and A-26 provides

- Stimulated Volume

$$\frac{1}{r_D}\frac{\partial}{\partial r_D}\left[k_r r_D \frac{\partial p_{D1}}{\partial r_D}\right] = k_o \frac{\partial p_{D1}}{\partial t_D} \quad \text{(A-27)}$$

- Unstimulated Volume

$$\frac{1}{r_D}\frac{\partial}{\partial r_D}\left[k_o r_D \frac{\partial p_{D2}}{\partial r_D}\right] = k_o \frac{\partial p_{D2}}{\partial t_D} \quad \text{(A-28)}$$

By factoring out and canceling the k_o terms, I get the final form of the dimensionless diffusivity equation for the unstimulated zone:

- Unstimulated Volume

$$\frac{1}{r_D}\frac{\partial}{\partial r_D}\left[r_D \frac{\partial p_{D2}}{\partial r_D}\right] = \frac{\partial p_{D2}}{\partial t_D} \quad \text{(A-29)}$$

Now, I introduce the power law model for the behavior of permeability in the stimulated zone:

$$k_r(r) = k_o\left[\frac{r}{r_s}\right]^n \quad \text{(A-30)}$$

Substituting Eq. A-30 into Eq. A-27 results in

- Stimulated Volume

$$\frac{1}{r_D}\frac{\partial}{\partial r_D}\left[k_o\left[\frac{r}{r_s}\right]^n r_D \frac{\partial p_{D1}}{\partial r_D}\right] = k_o \frac{\partial p_{D1}}{\partial t_D} \quad \text{(A-31)}$$

Moving all constants out from inside the derivatives and simplifying yields

$$\frac{1}{r_s^n}\frac{1}{r_D}\frac{\partial}{\partial r_D}\left[r^n r_D \frac{\partial p_{D1}}{\partial r_D}\right] = \frac{\partial p_{D1}}{\partial t_D} \quad \text{(A-32)}$$

Solving Eq. A-8 and A-9 for r and r_s respectively and substituting into Eq. A-32 gives

$$\frac{1}{(r_w r_{sD})^n}\frac{1}{r_D}\frac{\partial}{\partial r_D}\left[(r_w r_D)^n r_D \frac{\partial p_{D1}}{\partial r_D}\right] = \frac{\partial p_{D1}}{\partial t_D} \quad \text{(A-33)}$$

Factoring out r_w and simplifying gives the final form of the dimensionless diffusivity equation for the stimulated volume

$$\frac{1}{r_{sD}^{n}}\frac{1}{r_D}\frac{\partial}{\partial r_D}\left[r_D^{n+1}\frac{\partial p_{D1}}{\partial r_D}\right]=\frac{\partial p_{D1}}{\partial t_D} \quad \text{(A-34)}$$

Next, substituting the definitions of r, r_s, r_e, p, and t from the dimensionless variables of Eq. A-8, A-9, A-10, A-11 and A-12 will provide the dimensionless initial and boundary conditions

- Initial Conditions (uniform pressure at time zero):

$$p_i-\frac{1}{2\pi}\frac{qB\mu}{k_oL_e}p_{D1}(r_D,t_D)\Big|_{t_D=0}=p_i-\frac{1}{2\pi}\frac{qB\mu}{k_oL_e}p_{D2}(r_D,t_D)\Big|_{t_D=0}=p_i \quad \text{(A-35)}$$

Subtracting p_i from each term gives

$$-\frac{1}{2\pi}\frac{qB\mu}{k_oL_e}p_{D1}(r_D,t_D)\Big|_{t_D=0}=-\frac{1}{2\pi}\frac{qB\mu}{k_oL_e}p_{D2}(r_D,t_D)\Big|_{t_D=0}=0 \quad \text{(A-36)}$$

And then dividing by $-\frac{1}{2\pi}\frac{qB\mu}{k_oL_e}$,

$$p_{D1}(r_D,t_D)\Big|_{t_D=0}=p_{D2}(r_D,t_D)\Big|_{t_D=0}=0 \quad \text{(A-37)}$$

- Outer Boundary Condition (no flow outer boundary):

$$\left[r_wr_D\frac{\partial}{\partial(r_wr_D)}\left(p_i-\frac{1}{2\pi}\frac{qB\mu}{k_oL_e}p_{D2}\right)\right]\Bigg\|_{r_D=r_{eD}}=0 \quad \text{(A-38)}$$

Expanding the terms inside the derivative,

$$\left[r_D\frac{\partial}{\partial r_D}(p_i)-r_D\frac{1}{2\pi}\frac{qB\mu}{k_oL_e}\frac{\partial p_{D2}}{\partial r_D}\right]\Bigg\|_{r_D=r_{eD}}=0 \quad \text{(A-39)}$$

Recognizing that the derivative of a constant is equal to zero and dividing by all constant terms gives

$$\left[r_D\frac{\partial p_{D2}}{\partial r_D}\right]\Bigg\|_{r_D=r_{eD}}=0 \quad \text{(A-40)}$$

- Inner Boundary Condition (constant flowrate):

$$\left[r_wr_D\frac{\partial}{\partial(r_wr_D)}\left(p_i-\frac{1}{2\pi}\frac{qB\mu}{k_oL_e}p_{D1}\right)\right]\Bigg\|_{r_D=1}=\frac{1}{2\pi}\frac{qB\mu}{k_rL_e} \quad \text{(A-41)}$$

Performing the same steps as for the outer boundary condition results in

$$\left[r_D \frac{\partial p_{D1}}{\partial r_D} \right]_{r_D=1} = -\frac{k_o}{k_r} \quad \text{(A-42)}$$

I can modify Eq. A-42 to be only in terms of r_{sD} and n by transforming the power law model of Eq. A-30 into a dimensionless form and evaluating at $r_D=1$. Substituting the dimensionless definitions of r_s and r and solving for k_o/k_r yields

$$\frac{k_o}{k_r} = \left[\frac{r_w r_{sD}}{r_w r_D} \right]^n \quad \text{(A-43)}$$

Evaluating Eq. A-43 at $r_D=1$ and simplifying gives me

$$\frac{k_o}{k_r} = r_{sD}^n \quad \text{(A-44)}$$

Substituting the results of Eq. A-44 into Eq. A-42 and I have

$$\left[r_D \frac{\partial p_{D1}}{\partial r_D} \right]_{r_D=1} = -r_{sD}^n \quad \text{(A-45)}$$

- Interface Condition (continuous pressure across the interface):

$$\left[p_i - \frac{1}{2\pi} \frac{qB\mu}{k_o L_e} p_{D1} \right]_{r_D=r_{sD}} = \left[p_i - \frac{1}{2\pi} \frac{qB\mu}{k_o L_e} p_{D2} \right]_{r_D=r_{sD}} \quad \text{(A-46)}$$

Reducing,

$$[p_{D1}]_{r_D=r_{sD}} = [p_{D2}]_{r_D=r_{sD}} \quad \text{(A-47)}$$

- Interface Condition (continuous flux across the interface):

$$\left[\frac{\partial}{\partial(r_w r_D)} \left(p_i - \frac{1}{2\pi} \frac{qB\mu}{k_o L_e} p_{D1} \right) \right]_{r_D=r_{sD}} = \left[\frac{\partial}{\partial(r_w r_D)} \left(p_i - \frac{1}{2\pi} \frac{qB\mu}{k_o L_e} p_{D2} \right) \right]_{r_D=r_{sD}} \quad \text{(A-48)}$$

Reducing,

$$\left[\frac{\partial p_{D1}}{\partial r_D} \right]_{r_D=r_{sD}} = \left[\frac{\partial p_{D2}}{\partial r_D} \right]_{r_D=r_{sD}} \quad \text{(A-49)}$$

Acquiring the general and particular solution to Eq. A-29 and A-34 requires transformation to the Laplace domain. So, I take the Laplace transformation of each diffusivity equation, where *s* is the Laplace transform variable, and I have

- Stimulated Volume

$$\frac{1}{r_{sD}^{n}}\frac{1}{r_D}\frac{\partial}{\partial r_D}\left[r_D^{n+1}\frac{d\bar{p}_{D1}}{dr_D}\right]=s\bar{p}_{D1}-p_{D1}\left[t_D=0\right] \quad \text{(A-50)}$$

- Unstimulated Volume

$$\frac{1}{r_D}\frac{\partial}{\partial r_D}\left[r_D\frac{d\bar{p}_{D2}}{dr_D}\right]=s\bar{p}_{D2}-p_{D2}\left[t_D=0\right] \quad \text{(A-51)}$$

Substituting the initial conditions of Eq. A-37 into Eq. A-50 and A-51 gives

- Stimulated Volume

$$\frac{1}{r_{sD}^{n}}\frac{1}{r_D}\frac{\partial}{\partial r_D}\left[r_D^{n+1}\frac{d\bar{p}_{D1}}{dr_D}\right]=s\bar{p}_{D1} \quad \text{(A-52)}$$

- Unstimulated Volume

$$\frac{1}{r_D}\frac{\partial}{\partial r_D}\left[r_D\frac{d\bar{p}_{D2}}{dr_D}\right]=s\bar{p}_{D2} \quad \text{(A-53)}$$

I also need to transform the boundary conditions into the Laplace domain. Taking the Laplace transformation of the boundary conditions results in

- Outer Boundary Condition (no flow outer boundary):

$$\left[r_D\frac{\partial\bar{p}_{D2}}{\partial r_D}\right]\Bigg|_{r_D=r_{eD}}=0 \quad \text{(A-54)}$$

- Inner Boundary Condition (constant flow rate):

$$\left[r_D\frac{\partial\bar{p}_{D1}}{\partial r_D}\right]\Bigg|_{r_D=1}=-\frac{r_{sD}^{n}}{s} \quad \text{(A-55)}$$

- Interface Condition (continuous pressure across the interface):

$$\left[\bar{p}_{D1}\right]_{r_D=r_{sD}} = \left[\bar{p}_{D2}\right]_{r_D=r_{sD}} \quad \text{..... (A-56)}$$

- Interface Condition (continuous flux across the interface):

$$\left[\frac{\partial \bar{p}_{D1}}{\partial r_D}\right]_{r_D=r_{sD}} = \left[\frac{\partial \bar{p}_{D2}}{\partial r_D}\right]_{r_D=r_{sD}} \quad \text{..... (A-57)}$$

I can manipulate and rearrange Eq. A-52 to facilitate obtaining the general solution. For instance, I can expand Eq. A-52 using the product rule to give

- Stimulated Volume

$$\frac{1}{r_{sD}^n}\left[r_D^n \frac{d^2\bar{p}_{D1}}{dr_D^2} + (n+1) r_D^{n-1} \frac{d\bar{p}_{D1}}{dr_D}\right] = s\bar{p}_{D1} \quad \text{..... (A-58)}$$

Multiplying both sides by r_{Ds}^n / r_D^{n-2} yields

$$r_D^2 \frac{d^2\bar{p}_{D1}}{dr_D^2} + (n+1) r_D \frac{d\bar{p}_{D1}}{dr_D} = \frac{r_{sD}^n}{r_D^{n-2}} s\bar{p}_{D1} \quad \text{..... (A-59)}$$

Eq. A-59 is the transformed version of the Bessel differential equation given by Bowman (1958) which has the following form:

$$x^2 \frac{d^2y}{dx^2} + (2p+1)x\frac{dy}{dx} = -\left[a^2 x^{2r} + \beta^2\right]y \quad \text{..... (A-60)}$$

And has the general solution:

$$y = x^{-p}\left[c_1 J_{\frac{\sqrt{p^2-\beta^2}}{r}}\left(\frac{a}{r}x^r\right) + c_2 Y_{\frac{\sqrt{p^2-\beta^2}}{r}}\left(\frac{a}{r}x^r\right)\right] \quad \text{..... (A-61)}$$

In my case,

$$y = \bar{p}_{D1}, \quad x = r_D, \quad p = \frac{n}{2}, \quad a = \sqrt{s r_{sD}^n}, \quad r = \frac{2-n}{2}, \quad \beta = 0 \quad \text{..... (A-62)}$$

However, notice that Bowman's (1958) equation differs by a negative sign in the non-derivative term. Therefore, the general solution will consist of modified Bessel functions as follows:

$$\bar{p}_{D1} = \frac{1}{\sqrt{r_D^n}}\left[c_1 I_{\frac{n}{n-2}}\left(\frac{-2r_D^{\frac{2-n}{2}}\sqrt{sr_{sD}^n}}{n-2} \right) + c_2 I_{\frac{-n}{n-2}}\left(\frac{-2r_D^{\frac{2-n}{2}}\sqrt{sr_{sD}^n}}{n-2} \right) \right] \quad \text{(A-63)}$$

I can perform similar manipulations to the unstimulated volume diffusivity equation, Eq.A-53. Beginning by expanding the derivatives I have

- Unstimulated Volume

$$\frac{d^2\bar{p}_{D2}}{dr_D^2} + \frac{1}{r_D}\frac{d\bar{p}_{D2}}{dr_D} = s\bar{p}_{D2} \quad \text{(A-64)}$$

Multiplying both sides by r_D^2 gives

$$r_D^2\frac{d^2\bar{p}_{D2}}{dr_D^2} + r_D\frac{d\bar{p}_{D2}}{dr_D} = sr_D^2\bar{p}_{D2} \quad \text{(A-65)}$$

Eq. A-65 has the well-known form of a modified Bessel equation which appears as follows:

$$x^2\frac{d^2y}{dx^2} + x\frac{dy}{dx} = -\left[a^2x^2 + \beta^2\right]y \quad \text{(A-66)}$$

And has the general solution:

$$y = c_3 I_0(ax) + c_4 K_0(ax) \quad \text{(A-67)}$$

In my case,

$$y = \bar{p}_{D2}, \quad x = r_D, \quad a = \sqrt{s}, \quad \beta = 0 \quad \text{(A-68)}$$

And so the general solution for the unstimulated zone is

$$\bar{p}_{D2} = c_3 I_0\left[\sqrt{s}r_D\right] + c_4 K_0\left[\sqrt{s}r_D\right] \quad \text{(A-69)}$$

At this juncture in the derivation, I have two general solutions. Eq. A-63 represents the pressure behavior in the porous media from a radius at the wellbore, r_w, to the radius of stimulation, r_s. Eq. A-69 represents the pressure behavior in the porous media from r_s to the reservoir boundary, r_e. Each equation has two unknown constants for a total of four unknowns (i.e. c_1, c_2, c_3, c_4). Therefore, I need four boundary

conditions to formulate a unique solution to this problem. I have a no flow outer boundary condition (i.e. the reservoir is a tank with no fluid passing to or from the outer reservoir boundary, r_e), and I have a constant flow rate inner boundary condition at the wellbore. The two additional boundary conditions come from the interface of the two regions. I specify that the pressures and the flux must be continuous across this interface.

I solved this system of equations using *Mathematica*. The final result is presented below with simplifying notation.

- Stimulated Volume

$$\bar{p}_{D1} = \frac{1}{s^{3/2}} \sqrt{\frac{r_{sD}^n}{r_D^n}} \left[c_1 \, I_{\frac{n}{n-2}} \left[\frac{-2 r_D^{\frac{2-n}{2}} \sqrt{s r_{sD}^n}}{n-2} \right] + c_2 \, I_{\frac{-n}{n-2}} \left[\frac{-2 r_D^{\frac{2-n}{2}} \sqrt{s r_{sD}^n}}{n-2} \right] \right] \quad \text{(A-70)}$$

- Unstimulated Volume

$$\bar{p}_{D2} = \frac{1}{s^{3/2}} \left[c_3 I_0 \left[\sqrt{s} r_D \right] + c_4 K_0 \left[\sqrt{s} r_D \right] \right] \quad \text{(A-71)}$$

where

$$c_1 = \frac{f_0 b_4 - f_1 b_5}{b_1 \left[f_0 b_2 - f_1 b_3 \right] - b_0 \left[f_0 b_4 - f_1 b_5 \right]} \quad \text{(A-72)}$$

$$c_2 = -\frac{1}{b_1} \left[1 + \frac{b_0 \left[f_0 b_4 - f_1 b_5 \right]}{\left[b_1 \left[f_0 b_2 - f_1 b_3 \right] - b_0 \left[f_0 b_4 - f_1 b_5 \right] \right]} \right] \quad \text{(A-73)}$$

$$c_3 = \frac{f_2 K_1 \left[a_5 \right]}{f_3 - f_4 + f_5 - f_6} \quad \text{(A-74)}$$

$$c_4 = \frac{f_2 I_1 \left[a_5 \right]}{f_3 - f_4 + f_5 - f_6} \quad \text{(A-75)}$$

Simplifying notation:

$$\delta = \frac{2}{n-2}, \quad \beta = \frac{n}{n-2}$$

$$a_0 = \sqrt{s}, \quad a_1 = \sqrt{s r_{sD}^n}, \quad a_2 = -a_1 \delta, \quad a_3 = a_2 \left[r_{sD} \right]^{1-n/2}, \quad a_4 = a_0 r_{sD}, \quad a_5 = a_0 r_{eD}$$

$$b_0 = I_{\delta}[a_2], \quad b_1 = I_{-\delta}[a_2], \quad b_2 = I_{\delta}[a_3], \quad b_3 = I_{\beta}[a_3], \quad b_4 = I_{-\delta}[a_3], \quad b_5 = I_{-\beta}[a_3]$$

$$f_0 = a_0 a_1 [I_1[a_5]K_0[a_4] + I_0[a_4]K_1[a_5]], \quad f_1 = a_0 a_1 [I_1[a_4]K_1[a_5] - I_1[a_5]K_1[a_4]],$$

$$f_2 = a_1 [b_2 b_5 - b_4 b_3], \quad f_3 = a_1 I_0[a_4]K_1[a_5][b_0 b_4 - b_1 b_2], \quad f_4 = a_1 I_1[a_4]K_1[a_5][b_0 b_5 - b_1 b_3],$$

$$f_5 = a_1 b_0 I_1[a_5][b_4 K_0[a_4] + b_5 K_1[a_4]], \quad f_6 = a_1 b_1 I_1[a_5][b_2 K_0[a_4] + b_3 K_1[a_4]]$$

APPENDIX B

OBTAINING THE PARTICULAR SOLUTION AND VERIFYING THAT PROBLEM CONDITIONS ARE SATISFIED

Laplace space solutions

- **Stimulated zone: general solution in Laplace space**

$$\text{GenSolP1}[r\_] = r^{\frac{-n}{2}} \left(\text{BesselI}\left[-\frac{n}{-2+n}, -\frac{2 r^{1-\frac{n}{2}} \sqrt{s\, r s^n}}{-2+n} \right] C[2] + \text{BesselI}\left[\frac{n}{-2+n}, -\frac{2 r^{1-\frac{n}{2}} \sqrt{s\, r s^n}}{-2+n} \right] C[1] \right);$$

- **Unstimulated zone: general solution in Laplace space**

$$\text{GenSolP2}[r\_] = \text{BesselI}\left[0, \sqrt{s}\ r\right] C[3] + \text{BesselK}\left[0, \sqrt{s}\ r\right] C[4];$$

- **Stimulated zone: first derivative of general solution in Laplace space**

$$\text{DGenSolP1}[r\_] = \text{FullSimplify}[D[\text{GenSolP1}[r], r]]$$

$$r^{-n} \sqrt{r s^n s} \left(\text{BesselI}\left[\frac{2}{-2+n}, -\frac{2 r^{1-\frac{n}{2}} \sqrt{r s^n s}}{-2+n} \right] C[1] + \text{BesselI}\left[-\frac{2}{-2+n}, -\frac{2 r^{1-\frac{n}{2}} \sqrt{r s^n s}}{-2+n} \right] C[2] \right)$$

- **Unstimulated zone: first derivative of general solution in Laplace space**

$$\text{DGenSolP2}[r\_] = \text{FullSimplify}[D[\text{GenSolP2}[r], r]]$$

$$\sqrt{s} \left(\text{BesselI}\left[1, r\sqrt{s}\right] C[3] - \text{BesselK}\left[1, r\sqrt{s}\right] C[4] \right)$$

- **Boundary Conditions in Laplace space:**
  There are four boundary conditions. The first is a Neumann inner boundary condition that specifies constant flow rate at the wellbore. The second is a Neumann outer boundary condition that specifies no flow across the boundary. The third is a Dirichlet boundary condition at the interface between the stimulated and unstimulated zone specifying that the pressure must be continuous across the interface. The fourth is a Neumann boundary condition at the interface between the stimulated and unstimulated zone specifying that the flux must be continuous across the interface.

1. Inner Boundary Condition:

```
InnerBC = Simplify[(r DGenSolP1[r] /. r → 1) == -rs^n/s]
```

$$\sqrt{rs^n\,s}\left(\text{BesselI}\left[\frac{2}{-2+n},-\frac{2\sqrt{rs^n\,s}}{-2+n}\right]C[1]+\text{BesselI}\left[-\frac{2}{-2+n},-\frac{2\sqrt{rs^n\,s}}{-2+n}\right]C[2]\right)==-\frac{rs^n}{s}$$

2. Outer Boundary Condition:

```
OuterBC = Simplify[ (DGenSolP2[r] /. r → re) == 0]
```

$$\sqrt{s}\left(\text{BesselI}\left[1,re\sqrt{s}\right]C[3]-\text{BesselK}\left[1,re\sqrt{s}\right]C[4]\right)==0$$

3. Constant Pressure at the Interface:

```
PressInterface = Simplify[(GenSolP2[r] /. r → rs) == (GenSolP1[r] /. r → rs)]
```

$$\text{BesselI}\left[0,rs\sqrt{s}\right]C[3]+\text{BesselK}\left[0,rs\sqrt{s}\right]C[4]==$$

$$rs^{-n/2}\left(\text{BesselI}\left[\frac{n}{-2+n},-\frac{2\,rs^{1-\frac{n}{2}}\sqrt{rs^n\,s}}{-2+n}\right]C[1]+\text{BesselI}\left[-\frac{n}{-2+n},-\frac{2\,rs^{1-\frac{n}{2}}\sqrt{rs^n\,s}}{-2+n}\right]C[2]\right)$$

4. Constant Flux at the Interface:

```
FluxInterface = Simplify[(DGenSolP2[r] /. r → rs) == (DGenSolP1[r] /. r → rs)]
```

$$\sqrt{s}\left(\text{BesselI}\left[1,rs\sqrt{s}\right]C[3]-\text{BesselK}\left[1,rs\sqrt{s}\right]C[4]\right)==$$

$$\frac{s\left(\text{BesselI}\left[\frac{2}{-2+n},-\frac{2\,rs^{1-\frac{n}{2}}\sqrt{rs^n\,s}}{-2+n}\right]C[1]+\text{BesselI}\left[-\frac{2}{-2+n},-\frac{2\,rs^{1-\frac{n}{2}}\sqrt{rs^n\,s}}{-2+n}\right]C[2]\right)}{\sqrt{rs^n\,s}}$$

- **Using the boundary conditions to solve for the four constants:**
  The output of the following cell expression is not shown here. The constant expressions are too long and tedious to follow in the form presented by *Mathematica.*

```
SolveConst =
    Simplify[Flatten[Solve[OuterBC && InnerBC && PressInterface && FluxInterface,
        {C[1], C[2], C[3], C[4]}]]];
```

- **Stimulated zone: particular solution in Laplace space**
  Inserting the constants into the general solution provides us with the particular solution in Laplace space for the stimulated zone. The solution is not revealed here because of its long and tedious form. I also present the first and second derivatives with respect to radius for later use in verifying the solution.

```
PartSolP1[s_] = Simplify[GenSolP1[r] /. SolveConst, r > 0];
```

```
DPartSolP1s[s_] = D[PartSolP1s[s], r];
```

```
D2PartSolP1s[s_] = D[D[PartSolP1s[s], r], r];
```

- **Unstimulated zone: particular solution in Laplace space**
  Inserting the constants into the general solution provides us with the particular solution in Laplace space for the unstimulated zone. The solution is not revealed here because of its long and tedious form. I also present the first and second derivatives with respect to radius for later use in verifying the solution.

```
PartSolP2[s_] = Simplify[GenSolP2[r] /. SolveConst, r > 0];
```

```
DPartSolP2s[s_] = D[PartSolP2s[s], r];
```

```
D2PartSolP2s[s_] = D[D[PartSolP2s[s], r], r];
```

- **Introducing notation to simplify the appearance of the particular solutions:**
  Although the notation does simplify the user's ability to visualize the solution, its main advantage is to facilitate easier application of the equations into a program for calculations.

$$\delta = \frac{2}{n-2};$$
$$\beta = \frac{n}{n-2};$$

$$a0 = \sqrt{s};$$
$$a1 = \sqrt{s\, rs^n};$$
$$a2 = -a1\,\delta;$$
$$a3 = a2\, rs^{1-\frac{n}{2}};$$
$$a4 = a0\, rs;$$
$$a5 = a0\, re;$$

$$b0 = BesselI[\delta, a2];$$
$$b1 = BesselI[-\delta, a2];$$
$$b2 = BesselI[\delta, a3];$$
$$b3 = BesselI[\beta, a3];$$
$$b4 = BesselI[-\delta, a3];$$
$$b5 = BesselI[-\beta, a3];$$

$$f0 = a0\, a1\, (BesselI[1, a5]\, BesselK[0, a4] + BesselI[0, a4]\, BesselK[1, a5]);$$
$$f1 = a0\, a1\, (BesselI[1, a4]\, BesselK[1, a5] - BesselI[1, a5]\, BesselK[1, a4]);$$
$$f2 = a1\, (b2\, b5 - b4\, b3);$$
$$f3 = a1\, BesselI[0, a4]\, BesselK[1, a5]\, (b4\, b0 - b1\, b2);$$
$$f4 = a1\, BesselI[1, a4]\, BesselK[1, a5]\, (b0\, b5 - b1\, b3);$$
$$f5 = a1\, b0\, BesselI[1, a5]\, (b4\, BesselK[0, a4] + b5\, BesselK[1, a4]);$$
$$f6 = a1\, b1\, BesselI[1, a5]\, (b2\, BesselK[0, a4] + b3\, BesselK[1, a4]);$$

$$c1 = \frac{rs^{\frac{n}{2}}\, (f0\, b4 - f1\, b5)}{s^{3/2}\, (b1\, (f0\, b2 - f1\, b3) - b0\, (f0\, b4 - f1\, b5))};$$
$$c2 = \frac{rs^{\frac{n}{2}}}{s^{3/2}\, b1}\left(-1 - \frac{(b0\, (f0\, b4 - f1\, b5))}{-b0\, (f0\, b4 - f1\, b5) + b1\, (f0\, b2 - f1\, b3)}\right);$$
$$c3 = \frac{f2\, BesselK[1, a5]}{s^{3/2}\, (f3 - f4 + f5 - f6)};$$
$$c4 = \frac{f2\, BesselI[1, a5]}{s^{3/2}\, (f3 - f4 + f5 - f6)};$$

- **Stimulated zone: particular solution**

$$PartSolP1s[s\_] = r^{\frac{-n}{2}}\left(BesselI\left[-\frac{n}{-2+n}, -\frac{2\, r^{1-\frac{n}{2}}\sqrt{s\, rs^n}}{-2+n}\right] c2 + BesselI\left[\frac{n}{-2+n}, -\frac{2\, r^{1-\frac{n}{2}}\sqrt{s\, rs^n}}{-2+n}\right] c1\right);$$

- **Unstimulated zone: particular solution**

```
PartSolP2s[s_] = BesselI[0, √s r] c3 + BesselK[0, √s r] c4;
```

Verifying solutions

- **Arbitrary parameters for solution evaluation:**
  I have selected arbitrary values for n, r_{Ds}, r_{De} and s to test whether the solution with new notation is the same as the original solution, that the solution meets the problem conditions and that the left-hand side equals the right-hand side of the original dimensionless diffusivity equation for each cylindrical region.

```
n = -5 * 10^-2;
rs = 200;
re = 400;
s = 1 * 10^-3;
```

- **Comparing original solutions to the solutions with simplifying notations:**
  - Stimulated Zone

```
N[PartSolP1[s] /. r → 1, 50]
```

3065.29217470201683327130917241528245129221635854 81

```
N[PartSolP1s[s] /. r → 1, 50]
```

3065.29217470201683327130917241528245129221635854 81

  - Unstimulated Zone

```
N[PartSolP2[s] /. r → 200, 50]
```

0.96899543412600165010651019324341108776205928554426

```
N[PartSolP2s[s] /. r → 200, 50]
```

0.96899543412600165010651019324341108776205928554426

- **Testing that the solution meets the boundary conditions:**

1. Inner Boundary Condition

```
InnerBCTest = N[r DPartSolP1s[s] /. r → 1, 50]
```

−767.270499010925500514058946012746109476169052868 50

```
N[(-rs^n)/s, 50]
```

−767.270499010925500514058946012746109476169052868 50

2. Outer Boundary Condition

```
OuterBCTest = N[DPartSolP2s[s] /. r → re, 50]
```

0

3. Constant Pressure at the Interface

```
StimZonePress = N[PartSolP1s[s] /. r → rs, 50]
```

0.968995434126001650106510193243411087762059285544 26

```
UnstimZonePress = N[PartSolP2s[s] /. r → rs, 50]
```

0.968995434126001650106510193243411087762059285544 26

4. Constant Flux at the Interface

```
StimZoneFlux = N[DPartSolP1s[s] /. r → rs, 50]
```

−0.032981127869595621515123481203134565839616825166717

```
UnstimZoneFlux = N[DPartSolP2s[s] /. r → rs, 50]
```

−0.032981127869595621515123481203134565839616825166717

- **Testing that the solution satisfies the original dimensionless diffusivity equation for the stimulated zone:**

$$\text{StimZoneLHS} = N\left[\frac{1}{r s^n}\left(r^n\, \text{D2PartSolP1s}[s] + (n+1)\, r^{n-1}\, \text{DPartSolP1s}[s]\right) /. r \to 1, 50\right]$$

3.065292174702016833271309172415282451292216358548 1

$$\text{StimZoneRHS} = N[s\, \text{PartSolP1s}[s] /. r \to 1, 50]$$

3.065292174702016833271309172415282451292216358548 1

- **Testing that the solution satisfies the original dimensionless diffusivity equation for the unstimulated zone:**

$$\text{UnstimZoneLHS} = N\left[\left(\text{D2PartSolP2s}[s] + \frac{1}{r}\, \text{DPartSolP2s}[s]\right) /. r \to 200, 50\right]$$

0.000968995434126001650106510193243411087762059285544 26

$$\text{UnstimZoneRHS} = N[s\, \text{PartSolP2s}[s] /. r \to 200, 50]$$

0.000968995434126001650106510193243411087762059285544 26

APPENDIX C

COMPARING ANALYTICAL PRESSURE AND RATE SOLUTIONS TO NUMERICAL SIMULATION RESULTS

C.1 Dimensionless Pressure Solutions

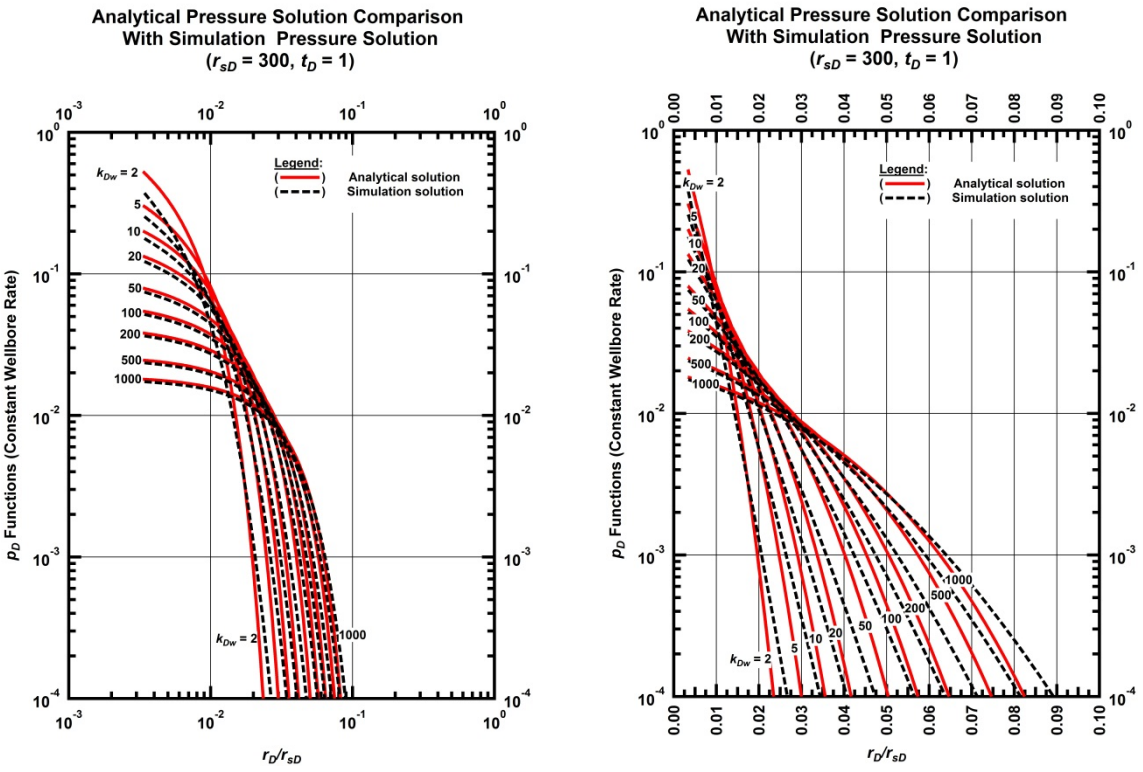

Figure C.1 — Comparison of analytic pressure solution to numerical pressure solution for a reservoir with $r_{sD}=300$ at $t_D=1$ (left: log-log, right: semi-log)

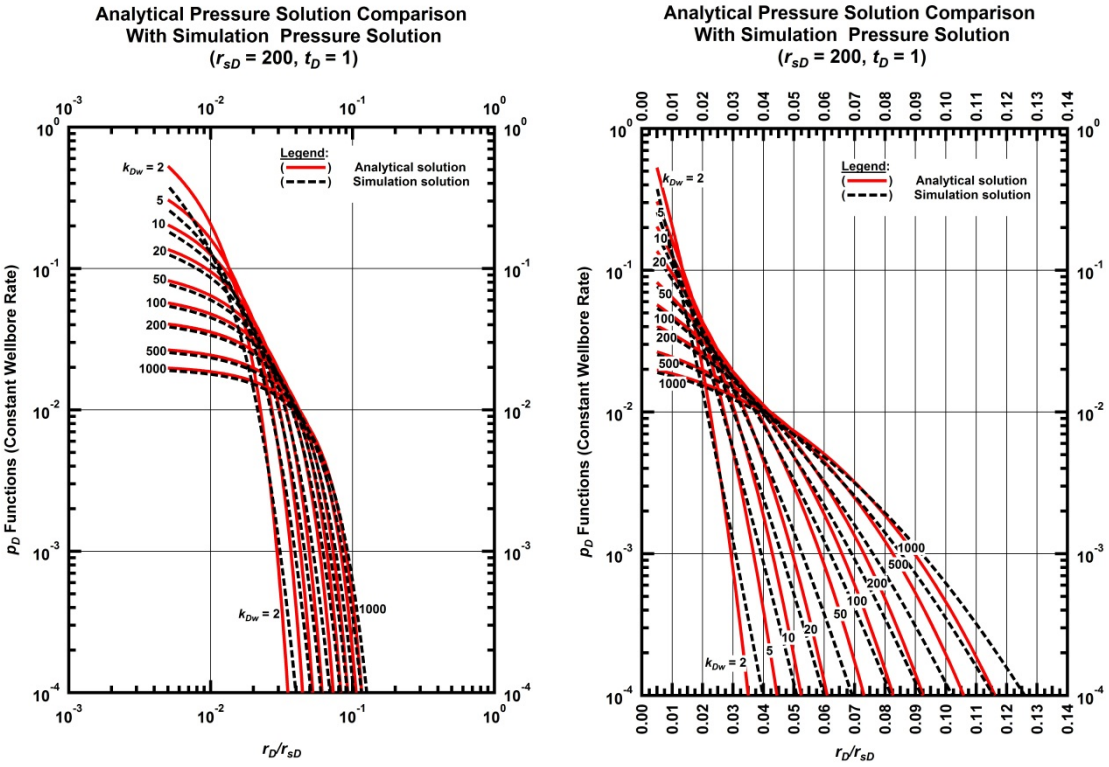

Figure C.2 — Comparison of analytic pressure solution to numerical pressure solution for a reservoir with $r_{sD}=200$ at $t_D=1$ (left: log-log, right: semi-log)

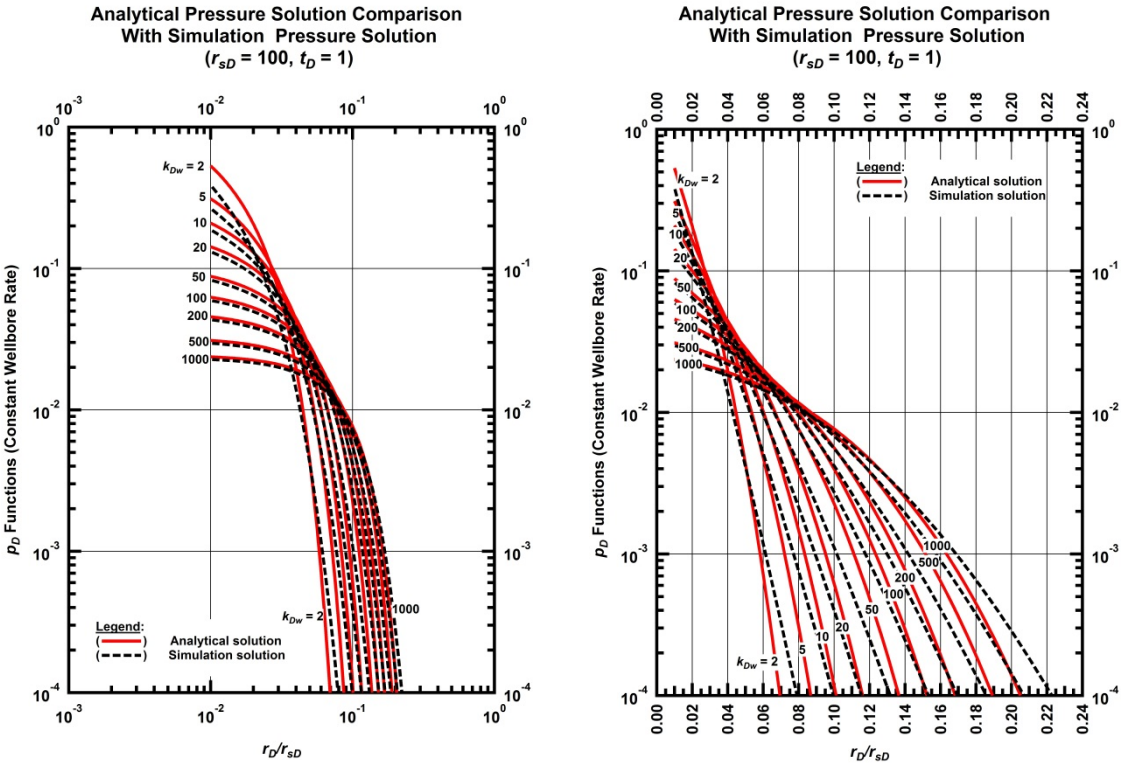

Figure C.3 — Comparison of analytic pressure solution to numerical pressure solution for a reservoir with $r_{sD}=100$ at $t_D=1$ (left: log-log, right: semi-log)

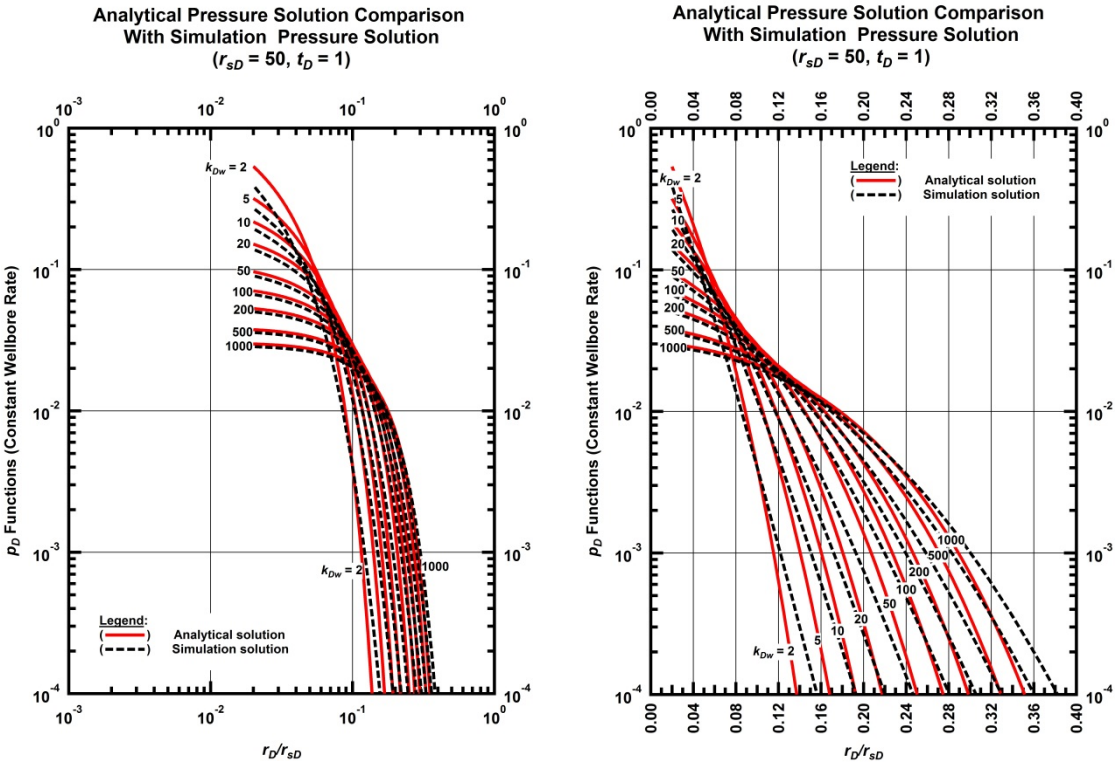

Figure C.4 — Comparison of analytic pressure solution to numerical pressure solution for a reservoir with $r_{sD}=50$ at $t_D=1$ (left: log-log, right: semi-log)

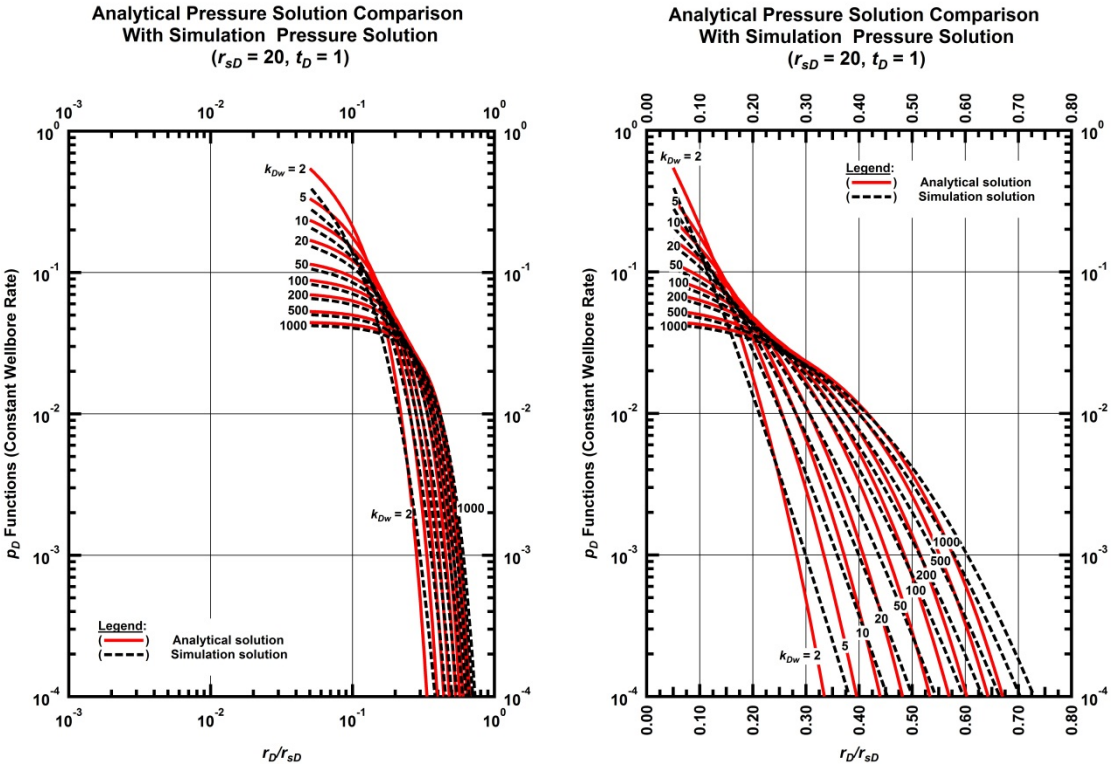

Figure C.5 — Comparison of analytic pressure solution to numerical pressure solution for a reservoir with $r_{sD}=20$ at $t_D=1$ (left: log-log, right: semi-log)

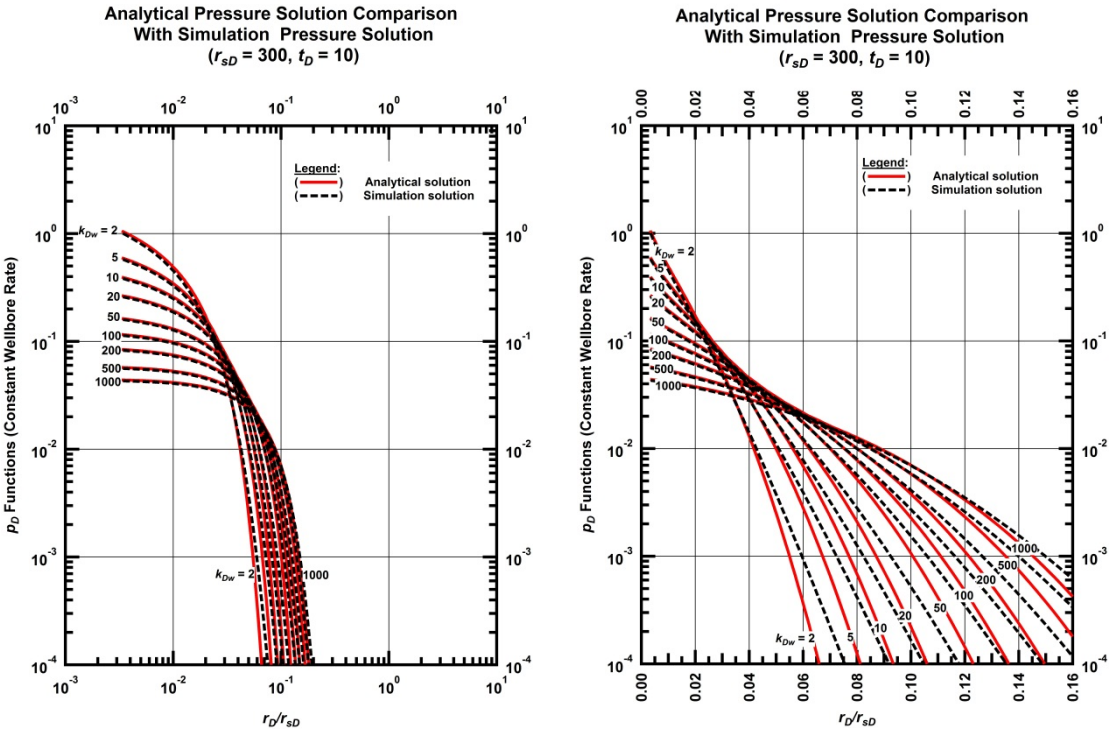

Figure C.6 — Comparison of analytic pressure solution to numerical pressure solution for a reservoir with $r_{sD}=300$ at $t_D=10$ (left: log-log, right: semi-log)

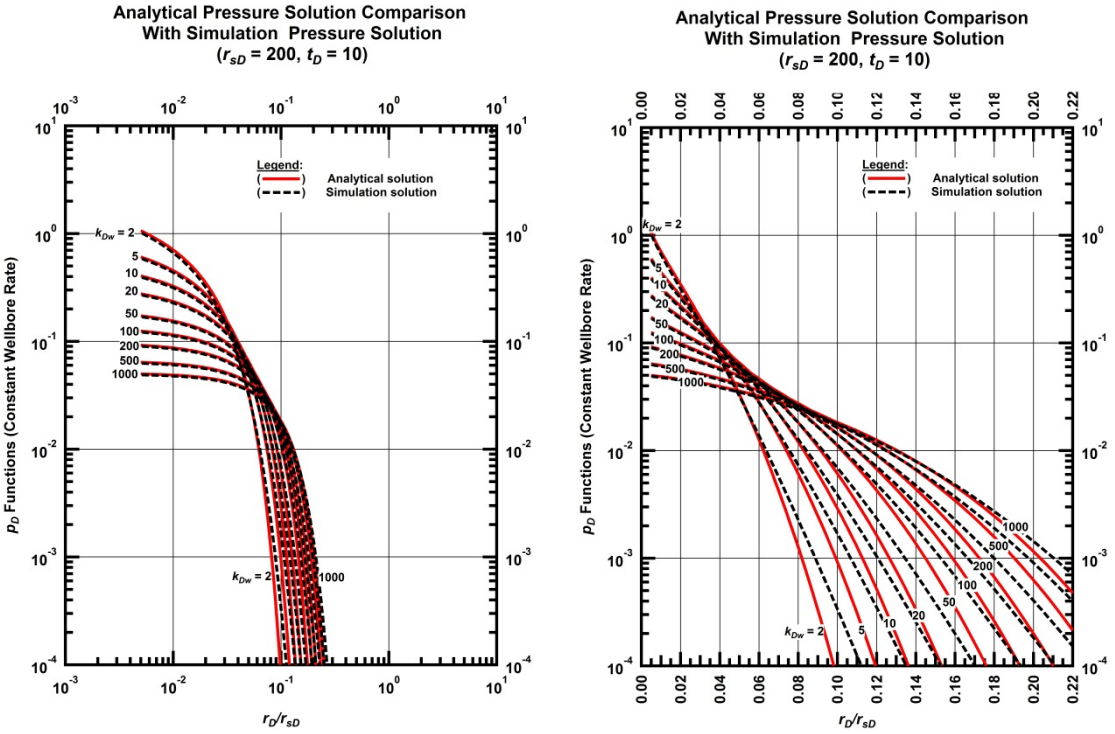

Figure C.7 — Comparison of analytic pressure solution to numerical pressure solution for a reservoir with $r_{sD}=200$ at $t_D=10$ (left: log-log, right: semi-log)

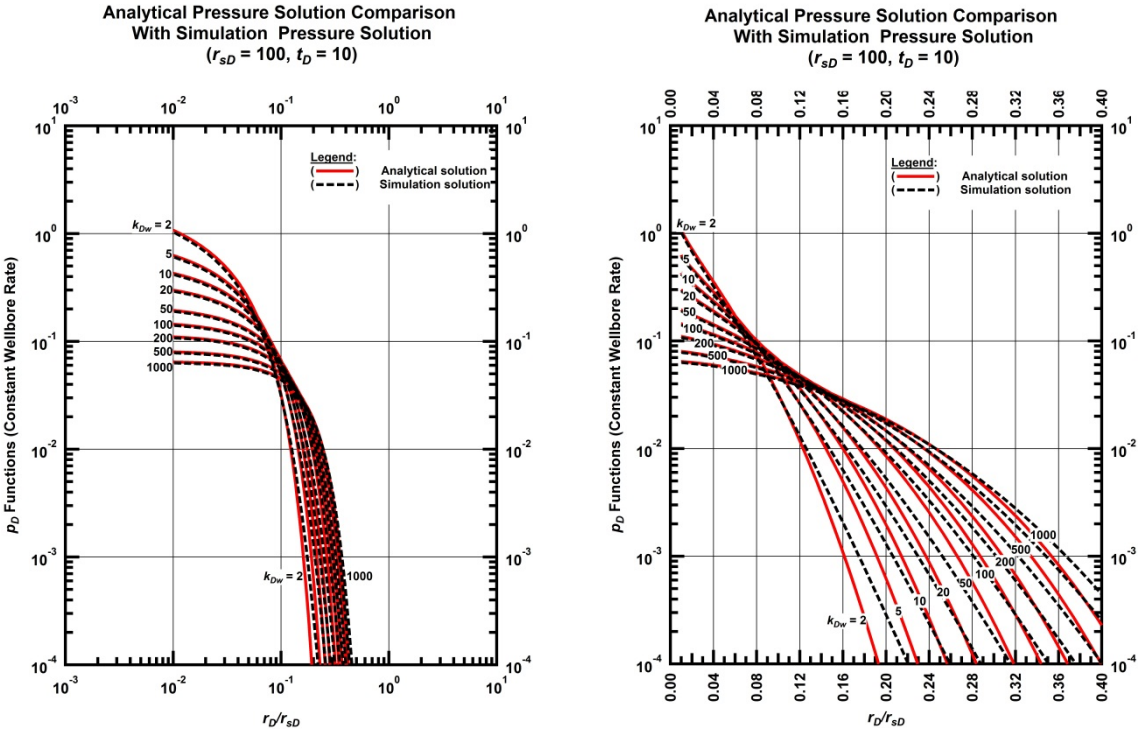

Figure C.8 — Comparison of analytic pressure solution to numerical pressure solution for a reservoir with $r_{sD}=100$ at $t_D=10$ (left: log-log, right: semi-log)

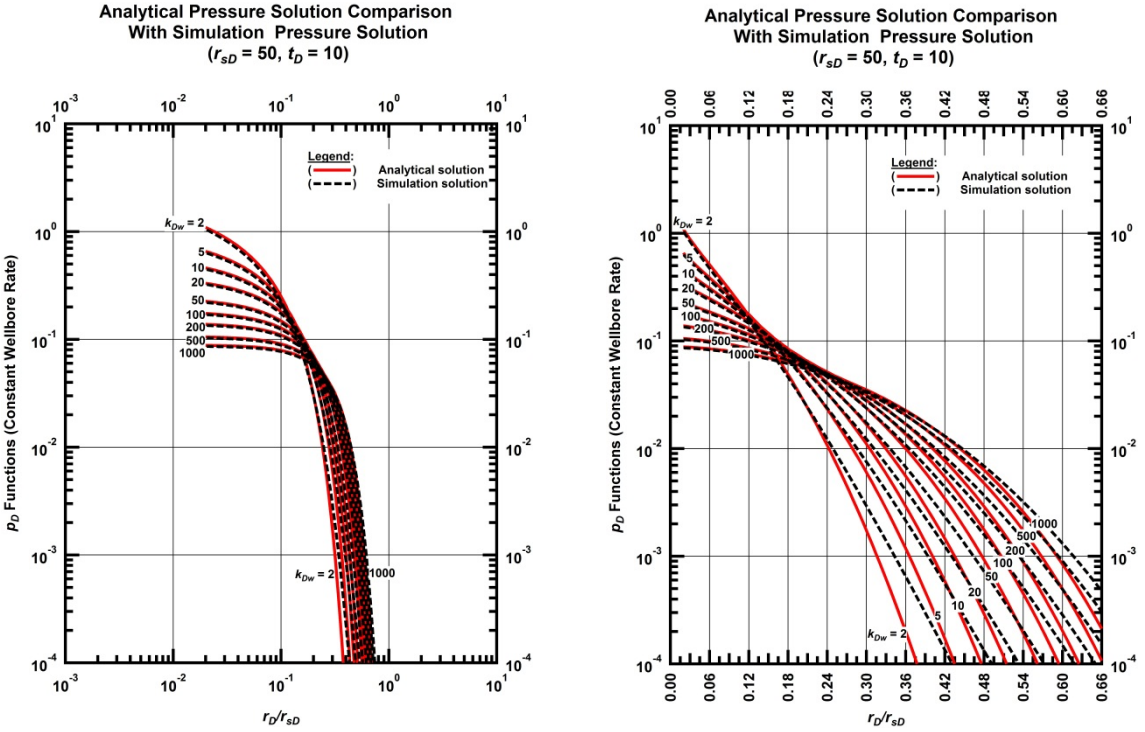

Figure C.9 — Comparison of analytic pressure solution to numerical pressure solution for a reservoir with $r_{sD}=50$ at $t_D=10$ (left: log-log, right: semi-log)

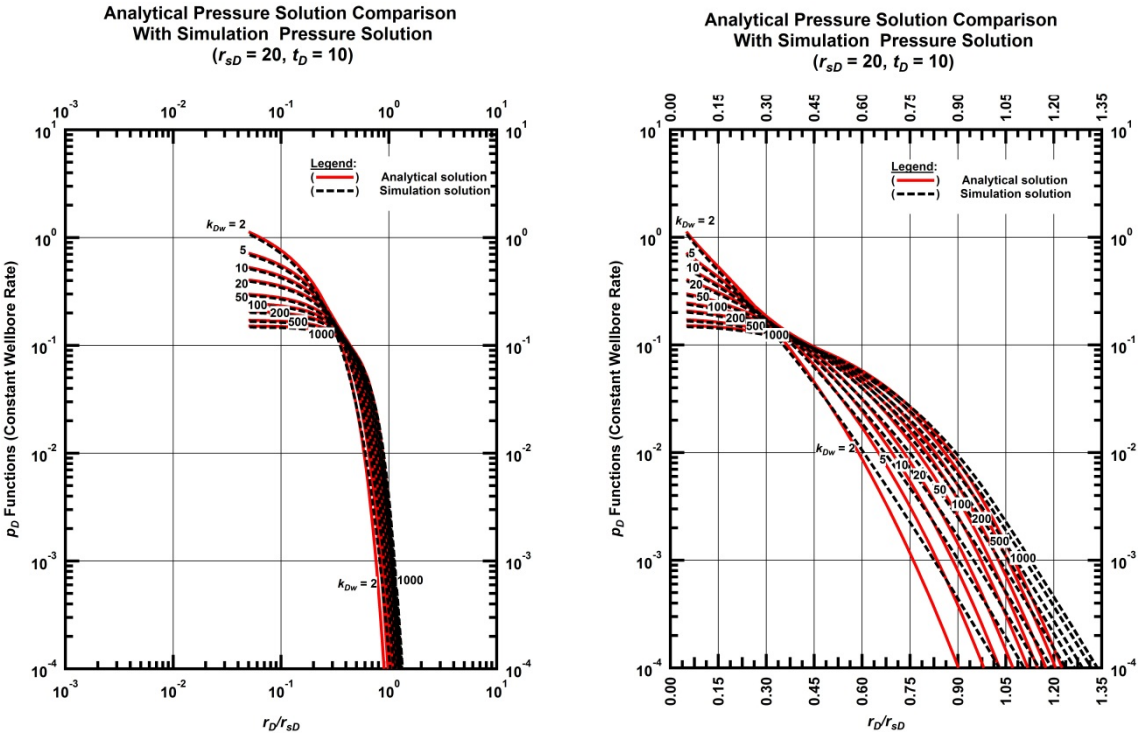

Figure C.10 — Comparison of analytic pressure solution to numerical pressure solution for a reservoir with $r_{sD}=20$ at $t_D=10$ (left: log-log, right: semi-log)

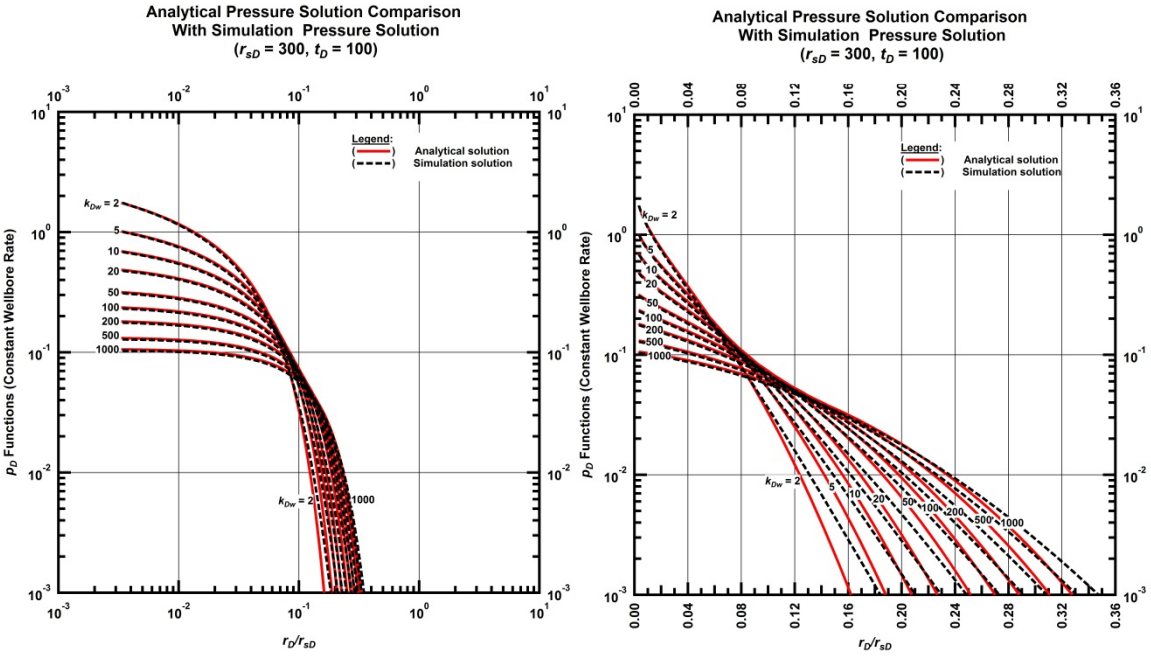

Figure C.11 — Comparison of analytic pressure solution to numerical pressure solution for a reservoir with $r_{sD}=300$ at $t_D=100$ (left: log-log, right: semi-log)

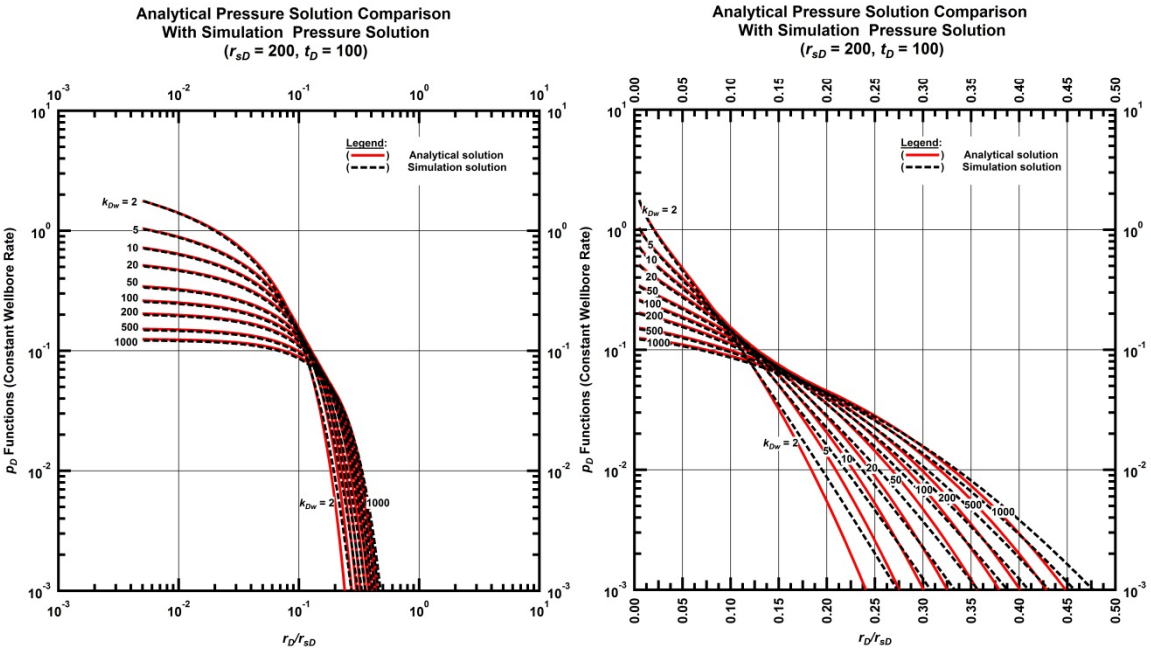

Figure C.12 — Comparison of analytic pressure solution to numerical pressure solution for a reservoir with $r_{sD}=200$ at $t_D=100$ (left: log-log, right: semi-log)

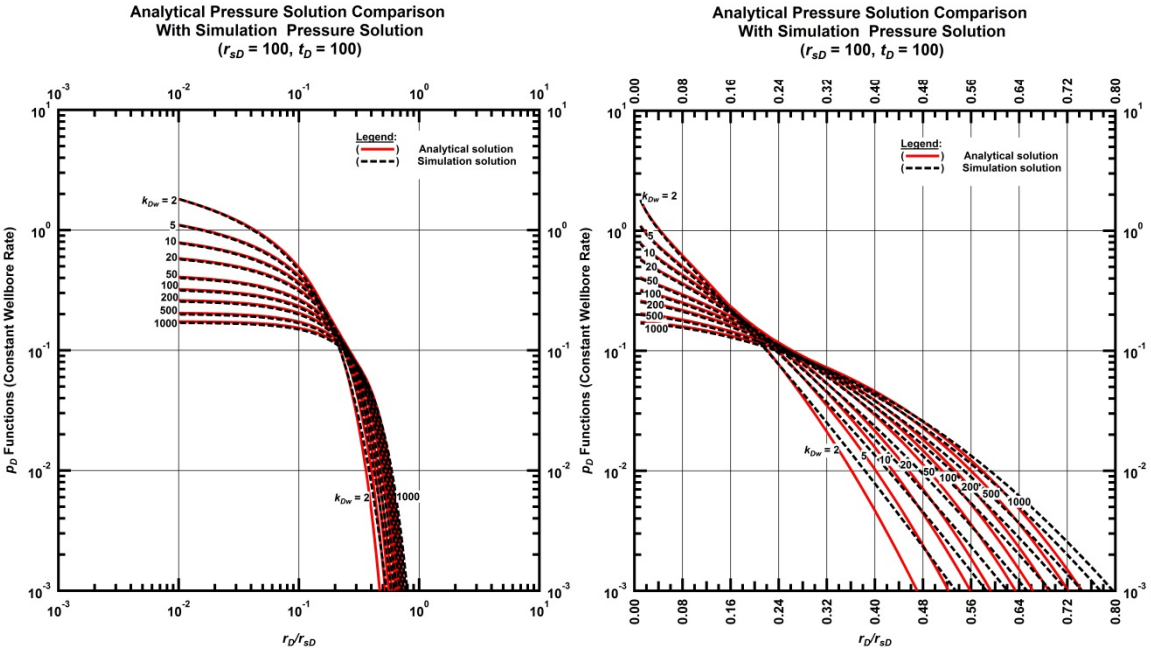

Figure C.13 — Comparison of analytic pressure solution to numerical pressure solution for a reservoir with $r_{sD}=100$ at $t_D=100$ (left: log-log, right: semi-log)

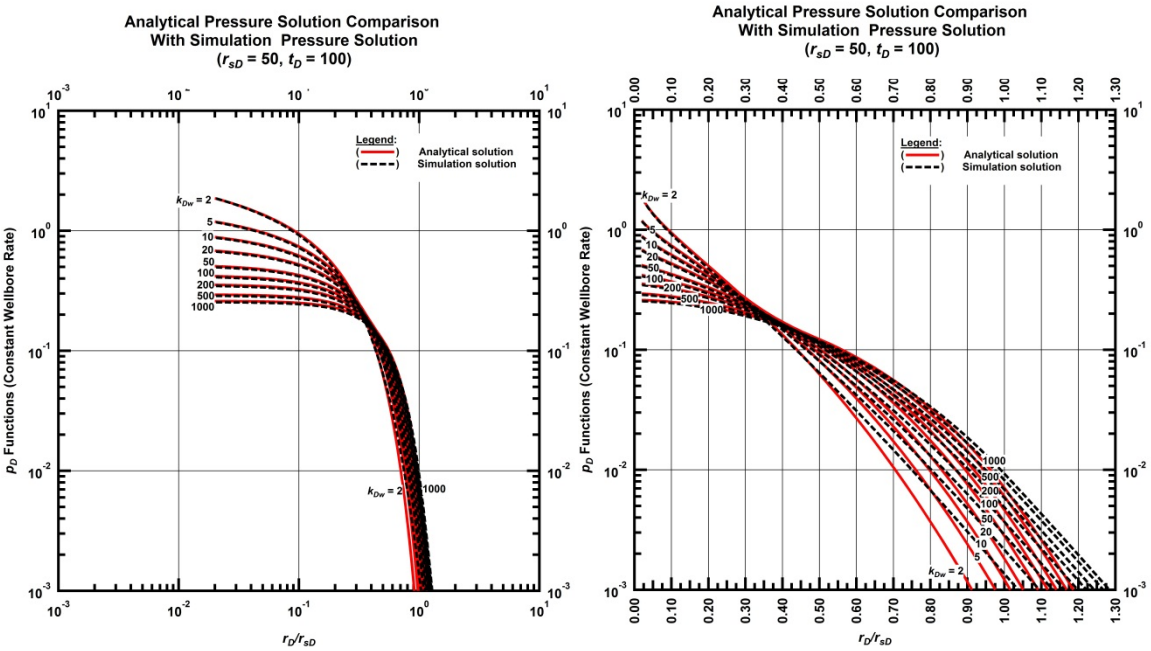

Figure C.14 — Comparison of analytic pressure solution to numerical pressure solution for a reservoir with $r_{sD}=50$ at $t_D=100$ (left: log-log, right: semi-log)

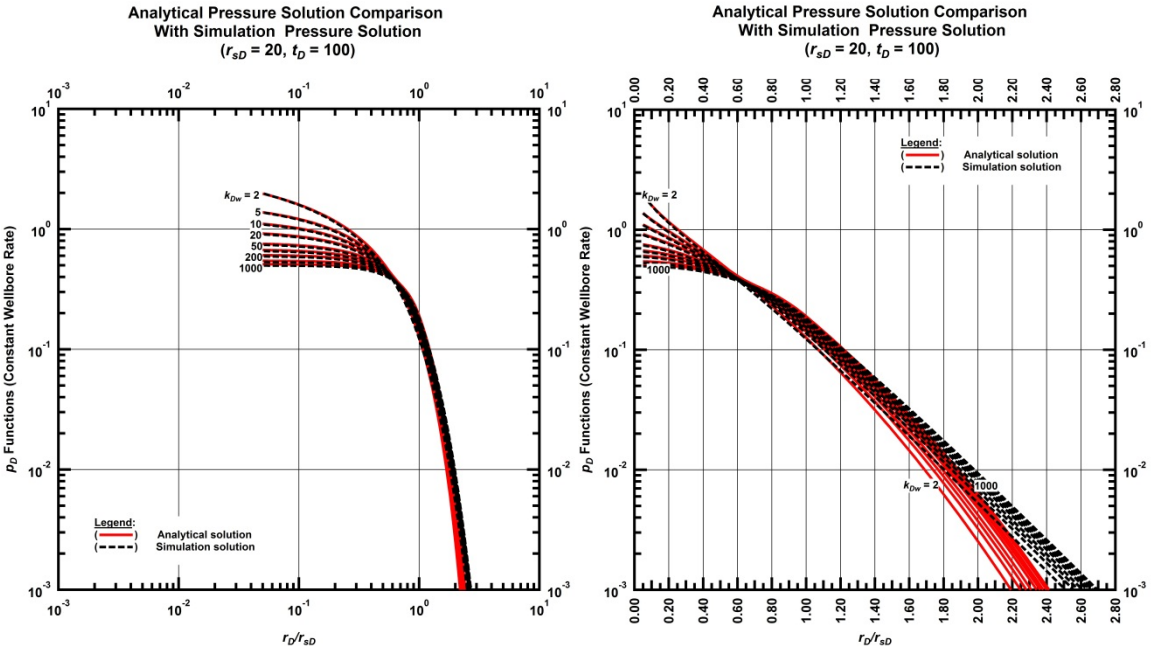

Figure C.15 — Comparison of analytic pressure solution to numerical pressure solution for a reservoir with $r_{sD}=20$ at $t_D=100$ (left: log-log, right: semi-log)

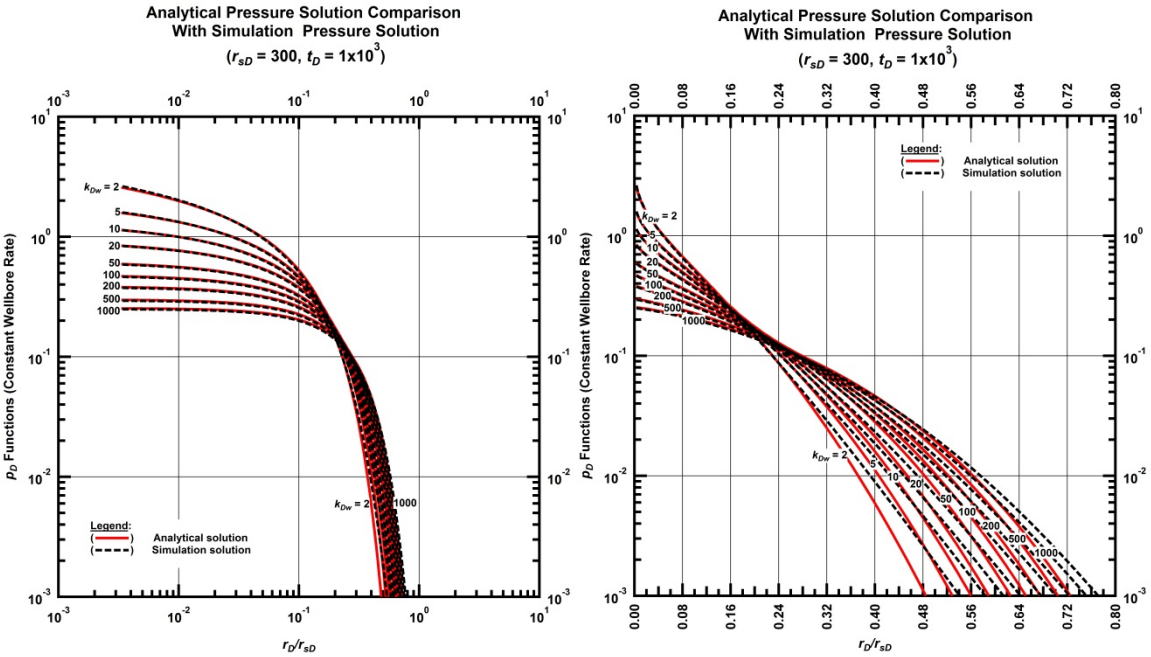

Figure C.16 — Comparison of analytic pressure solution to numerical pressure solution for a reservoir with $r_{sD}=300$ at $t_D=10^3$ (left: log-log, right: semi-log)

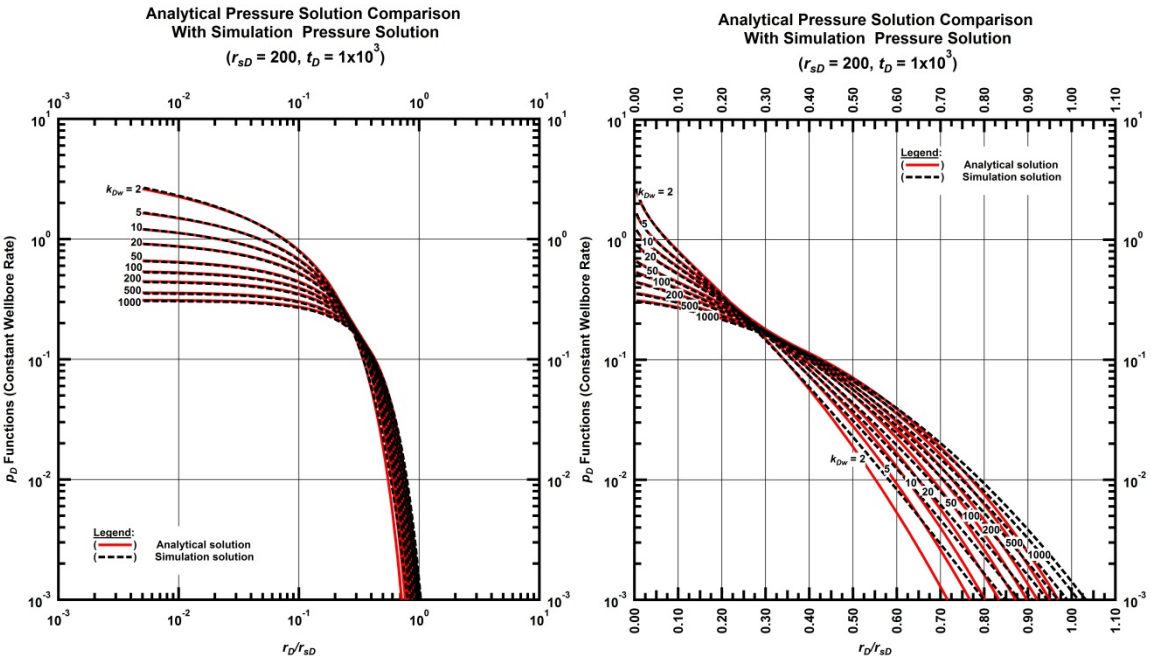

Figure C.17 — Comparison of analytic pressure solution to numerical pressure solution for a reservoir with $r_{sD}=200$ at $t_D=10^3$ (left: log-log, right: semi-log)

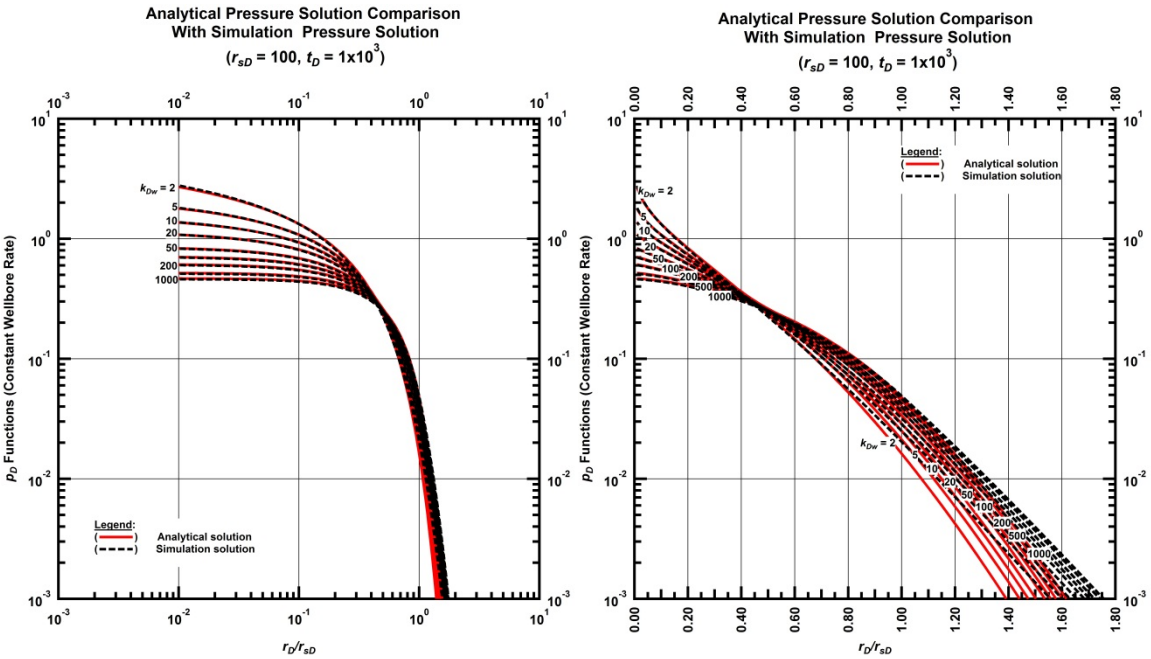

Figure C.18 — Comparison of analytic pressure solution to numerical pressure solution for a reservoir with $r_{sD}=100$ at $t_D=10^3$ (left: log-log, right: semi-log)

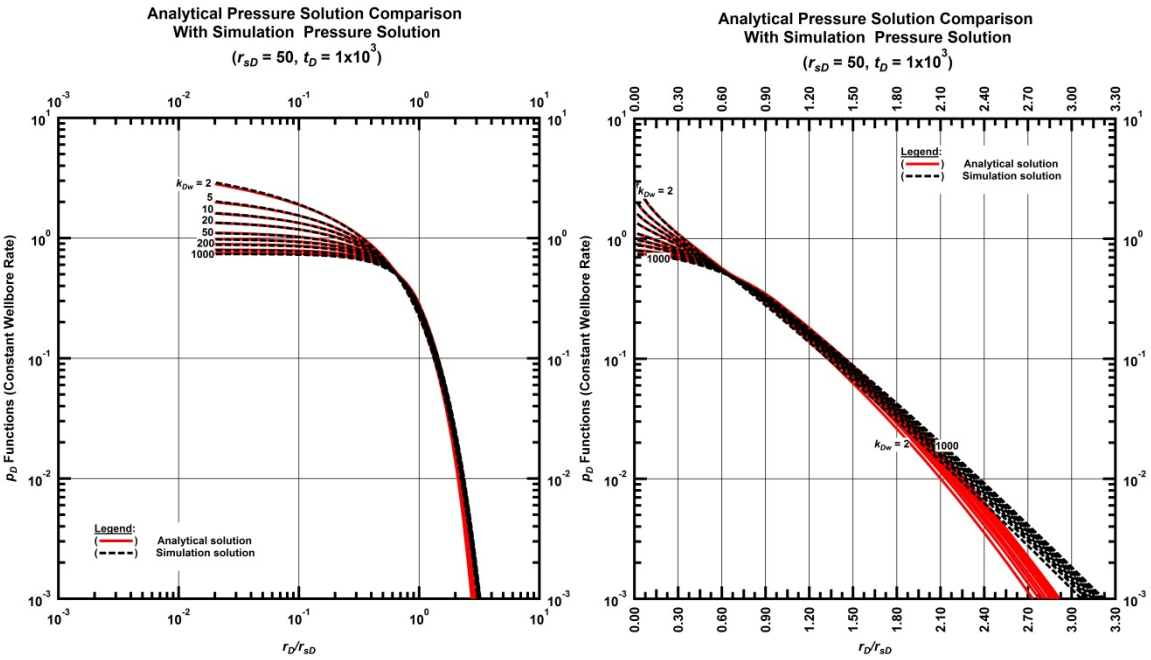

Figure C.19 — Comparison of analytic pressure solution to numerical pressure solution for a reservoir with $r_{sD}=50$ at $t_D=10^3$ (left: log-log, right: semi-log)

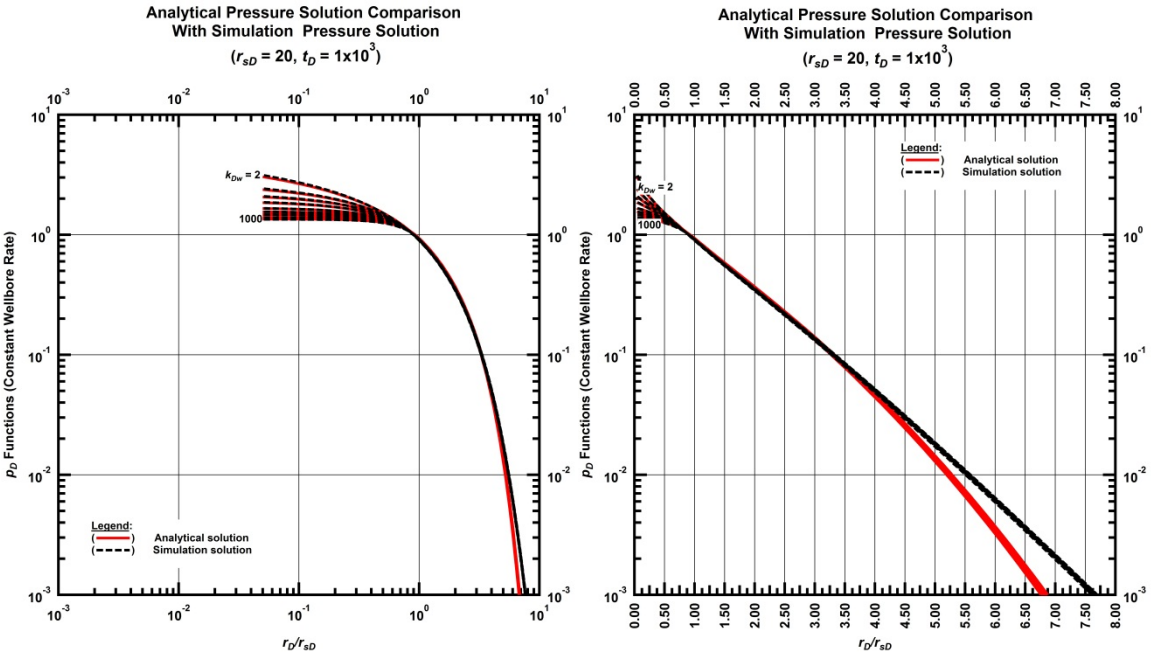

Figure C.20 — Comparison of analytic pressure solution to numerical pressure solution for a reservoir with $r_{sD}=20$ at $t_D=10^3$ (left: log-log, right: semi-log)

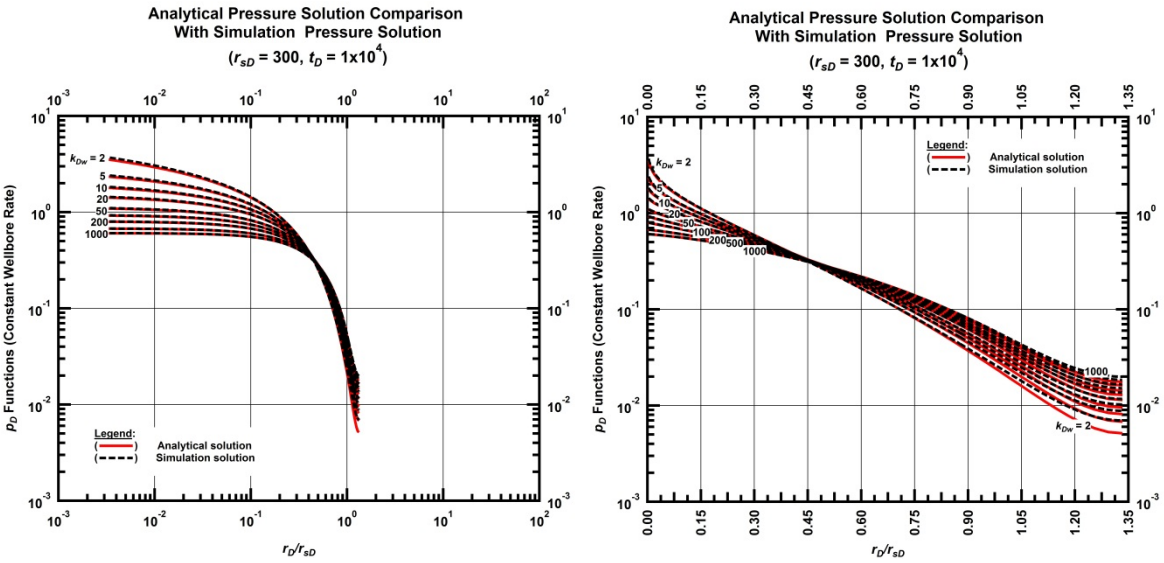

Figure C.21 — Comparison of analytic pressure solution to numerical pressure solution for a reservoir with $r_{sD}=300$ at $t_D=10^4$ (left: log-log, right: semi-log)

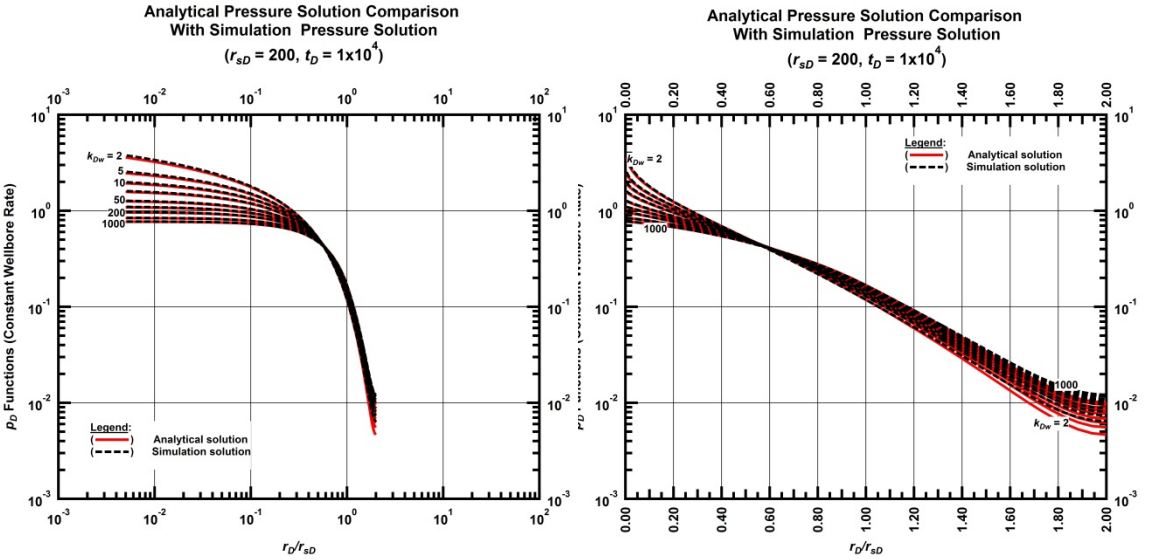

Figure C.22 — Comparison of analytic pressure solution to numerical pressure solution for a reservoir with $r_{sD}=200$ at $t_D=10^4$ (left: log-log, right: semi-log)

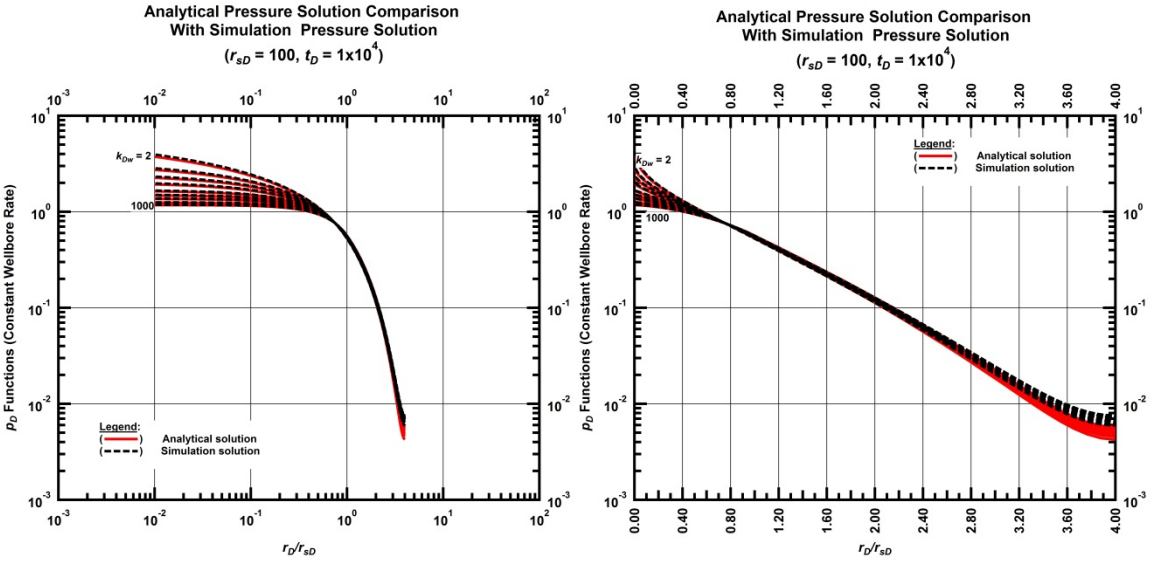

Figure C.23 — Comparison of analytic pressure solution to numerical pressure solution for a reservoir with $r_{sD}=100$ at $t_D=10^4$ (left: log-log, right: semi-log)

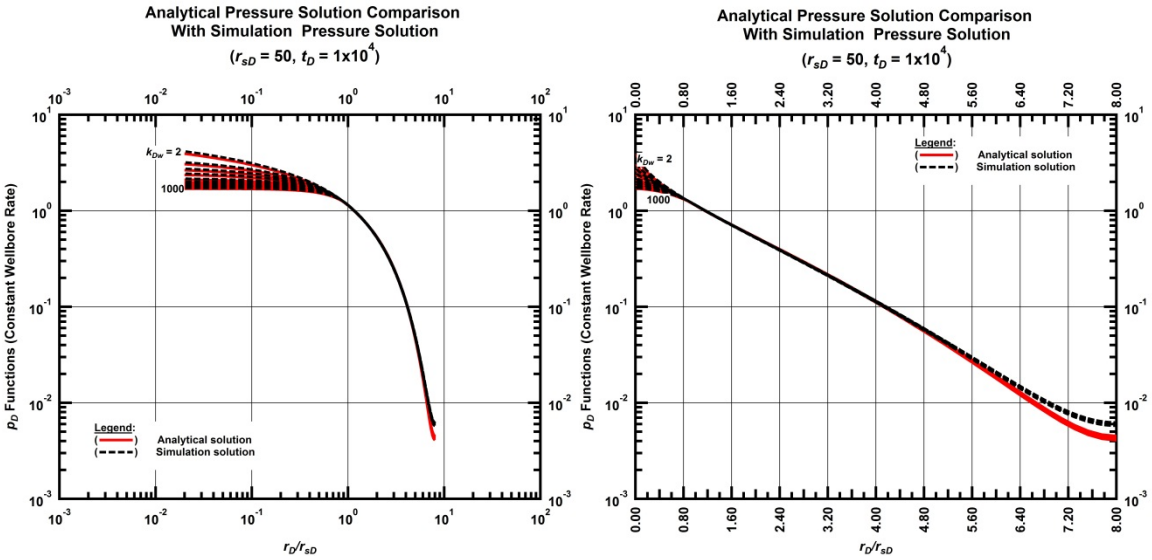

Figure C.24 — Comparison of analytic pressure solution to numerical pressure solution for a reservoir with $r_{sD}=50$ at $t_D=10^4$ (left: log-log, right: semi-log)

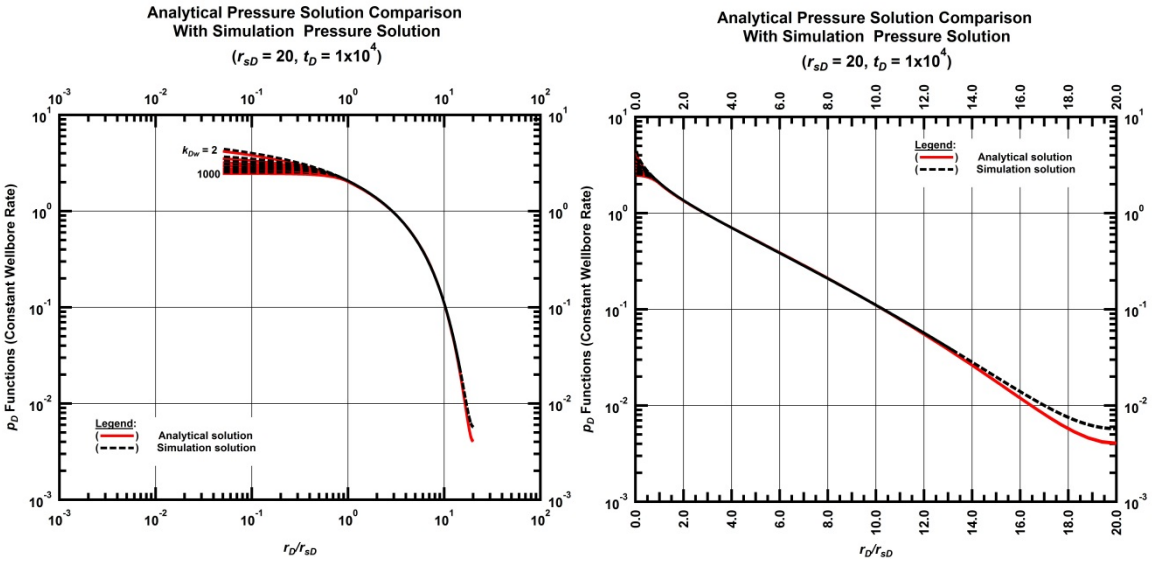

Figure C.25 — Comparison of analytic pressure solution to numerical pressure solution for a reservoir with $r_{sD}=20$ at $t_D=10^4$ (left: log-log, right: semi-log)

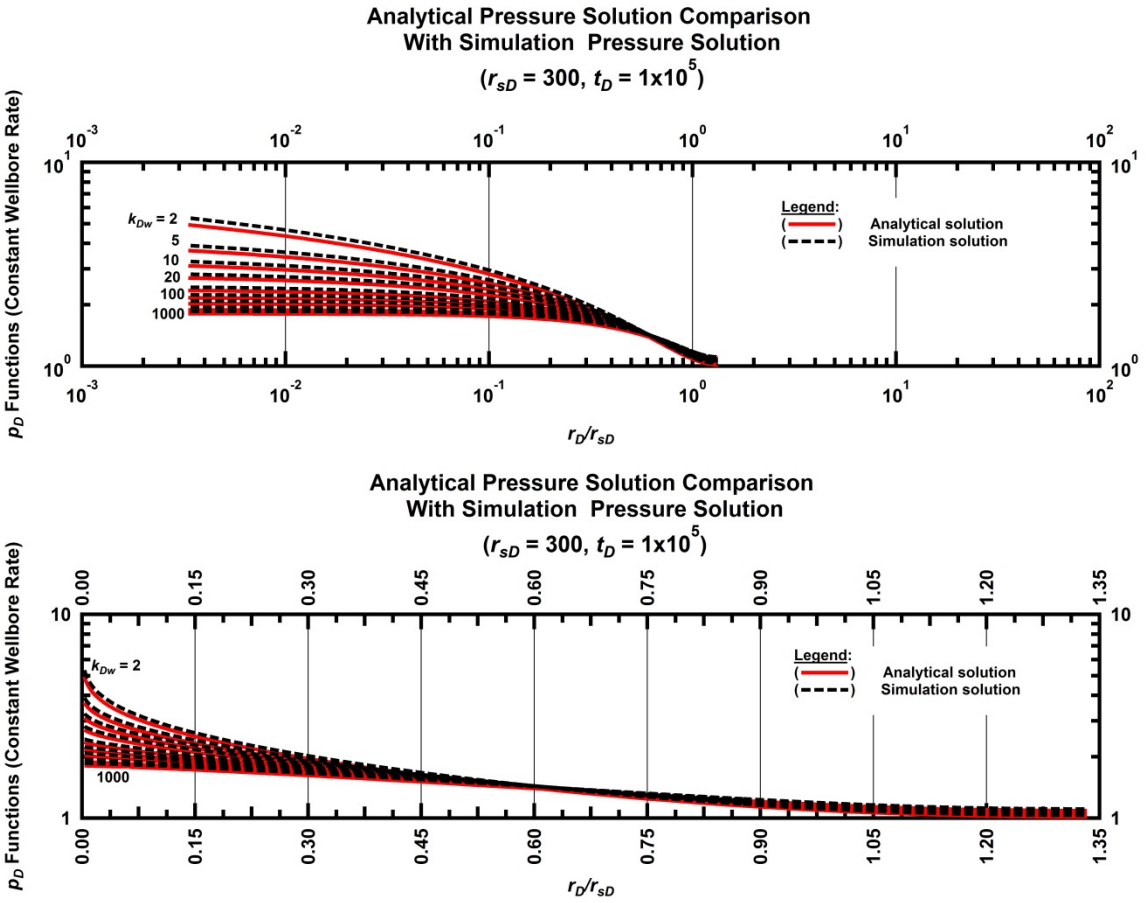

Figure C.26 — Comparison of analytic pressure solution to numerical pressure solution for a reservoir with $r_{sD}=300$ at $t_D=10^5$ (top: log-log, bottom: semi-log)

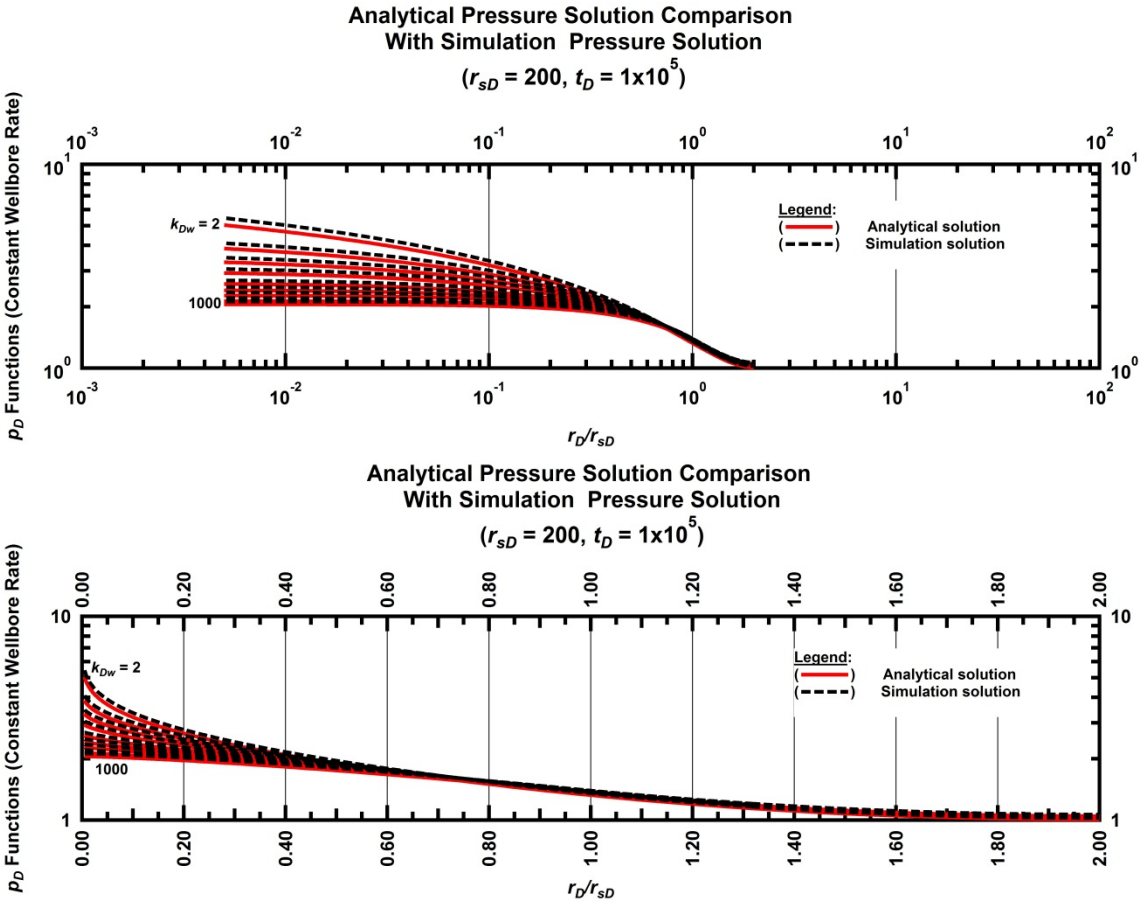

Figure C.27 — Comparison of analytic pressure solution to numerical pressure solution for a reservoir with $r_{sD}=200$ at $t_D=10^5$ (top: log-log, bottom: semi-log)

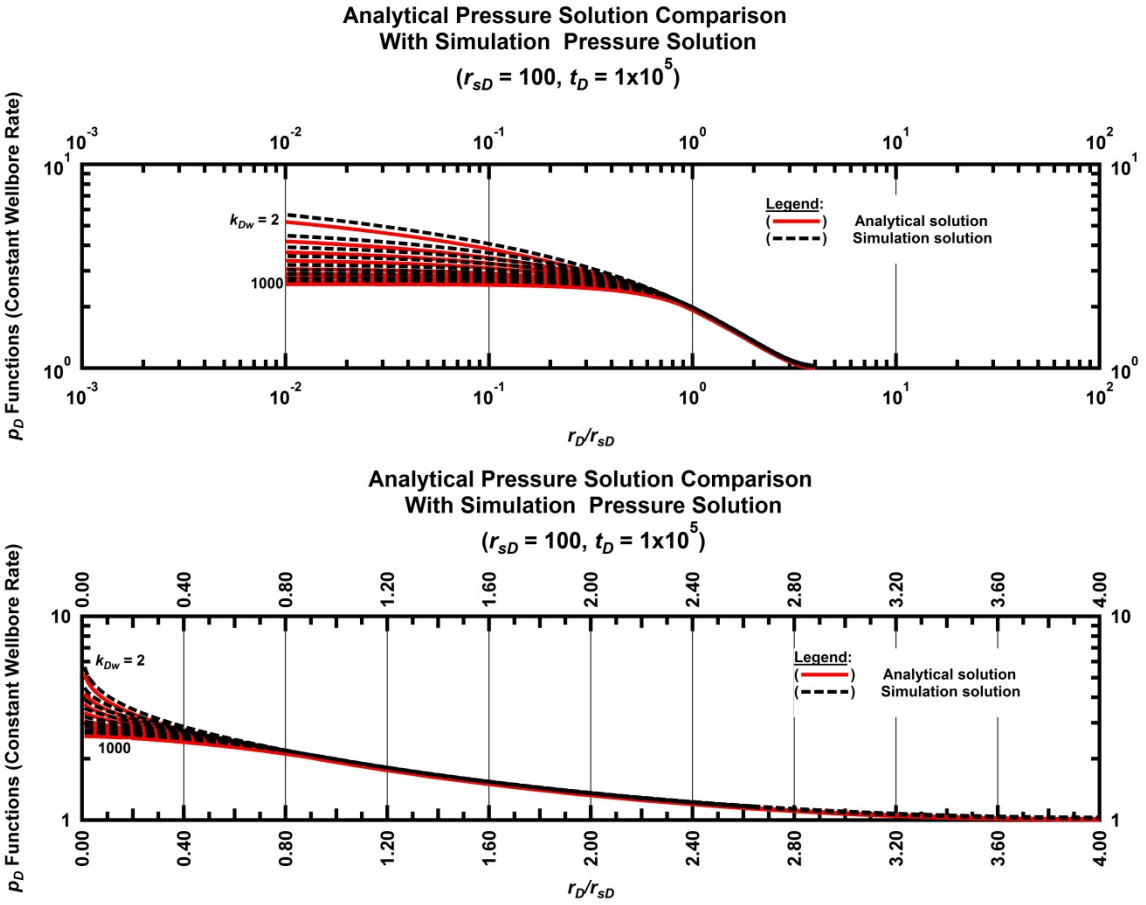

Figure C.28 — Comparison of analytic pressure solution to numerical pressure solution for a reservoir with $r_{sD}=100$ at $t_D=10^5$ (top: log-log, bottom: semi-log)

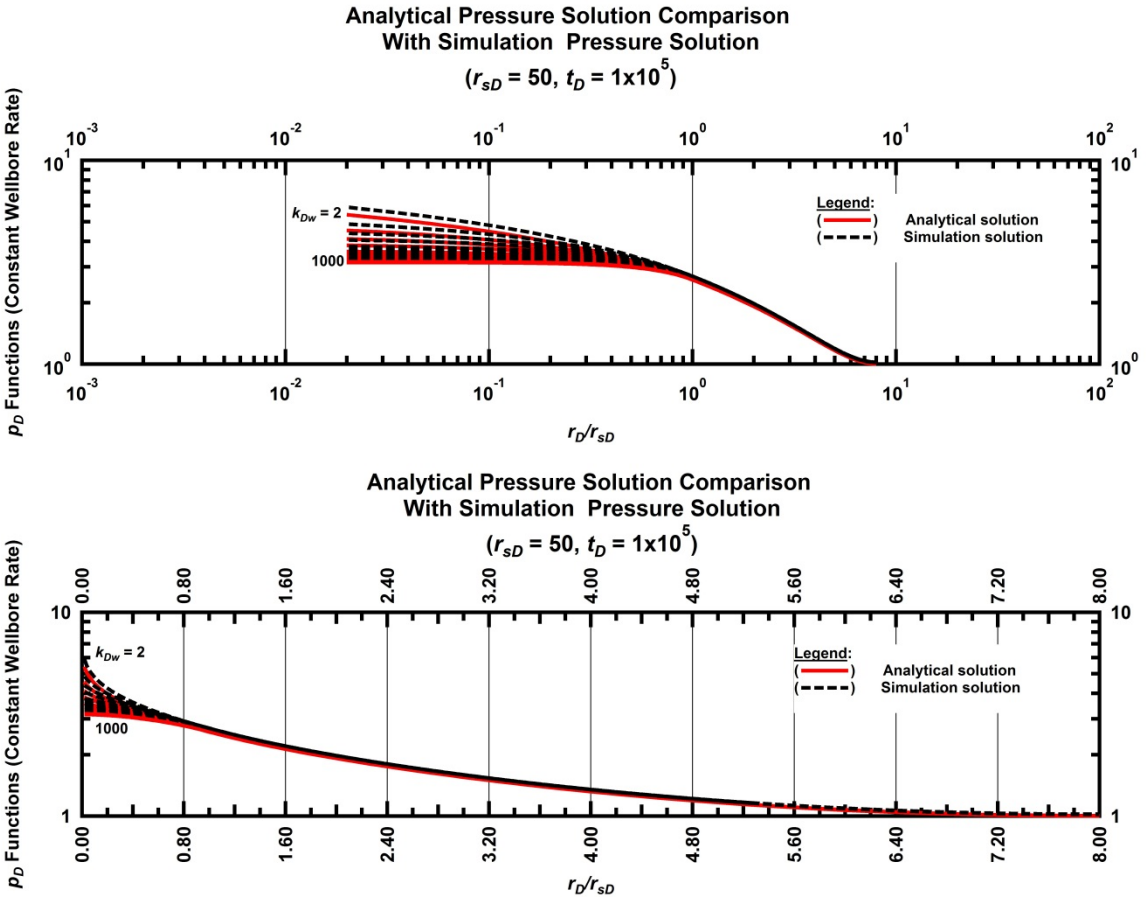

Figure C.29 — Comparison of analytic pressure solution to numerical pressure solution for a reservoir with $r_{sD}=50$ at $t_D=10^5$ (top: log-log, bottom: semi-log)

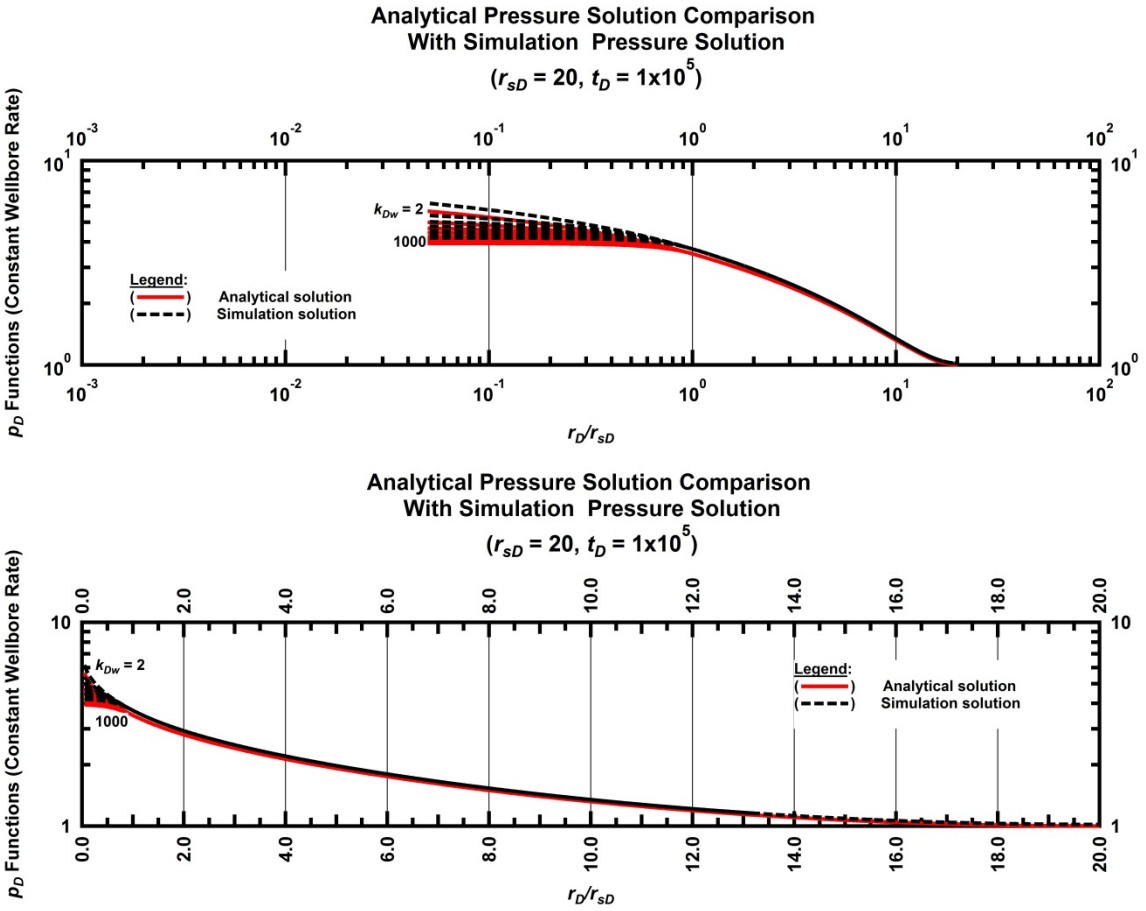

Figure C.30 — Comparison of analytic pressure solution to numerical pressure solution for a reservoir with $r_{sD}=20$ at $t_D=10^5$ (top: log-log, bottom: semi-log)

C.2 Dimensionless Rate Solutions

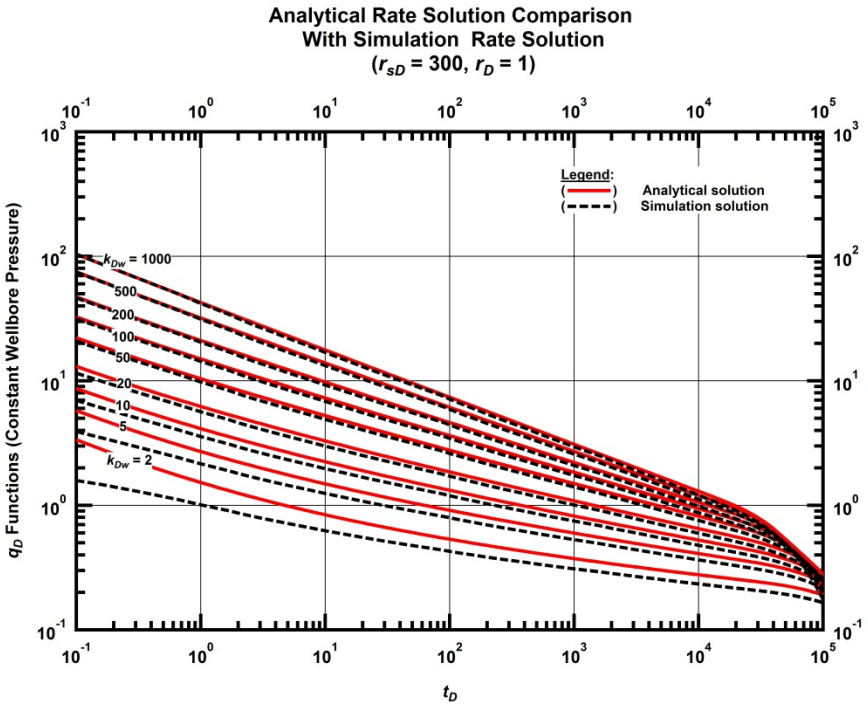

Figure C.31 — Log-log plot comparing the analytic rate solution to numerical rate solution for a reservoir with $r_{sD}=300$ at $r_D=1$.

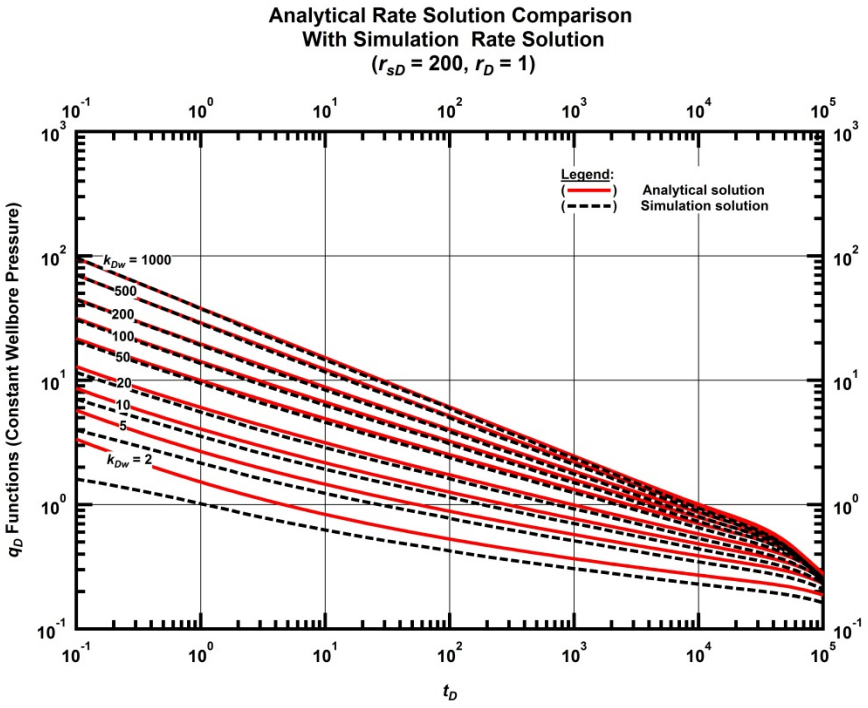

Figure C.32 — Log-log plot comparing the analytic rate solution to numerical rate solution for a reservoir with $r_{sD}=200$ at $r_D=1$.

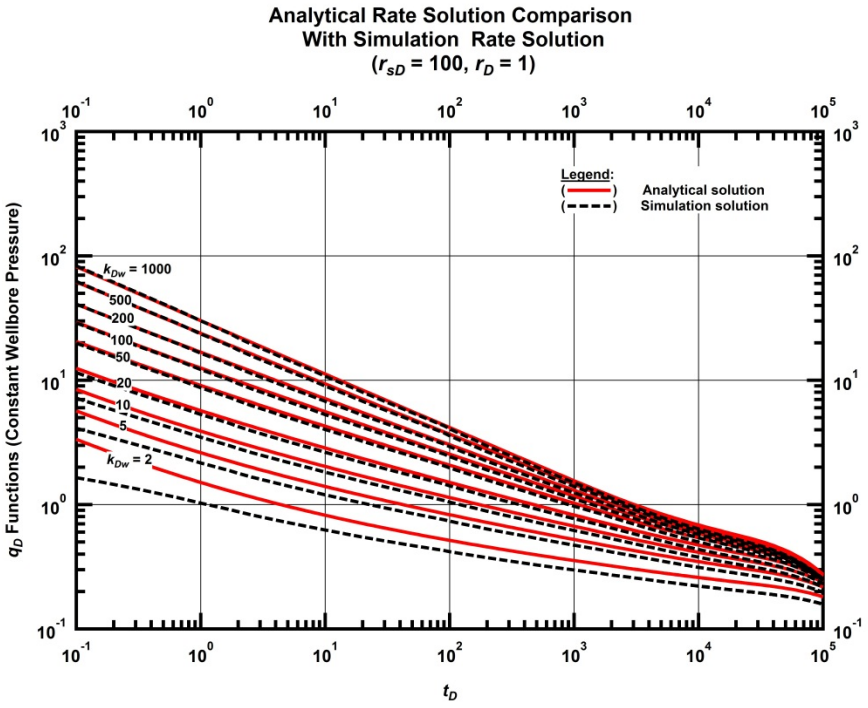

Figure C.33 — Log-log plot comparing the analytic rate solution to numerical rate solution for a reservoir with $r_{sD}=100$ at $r_D=1$.

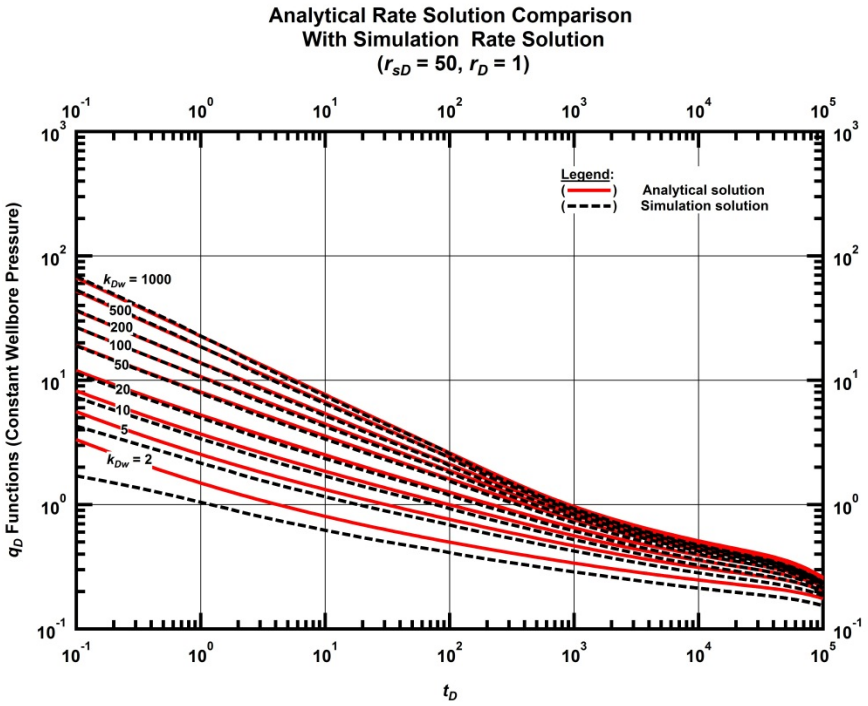

Figure C.34 — Log-log plot comparing the analytic rate solution to numerical rate solution for a reservoir with $r_{sD}=50$ at $r_D=1$.

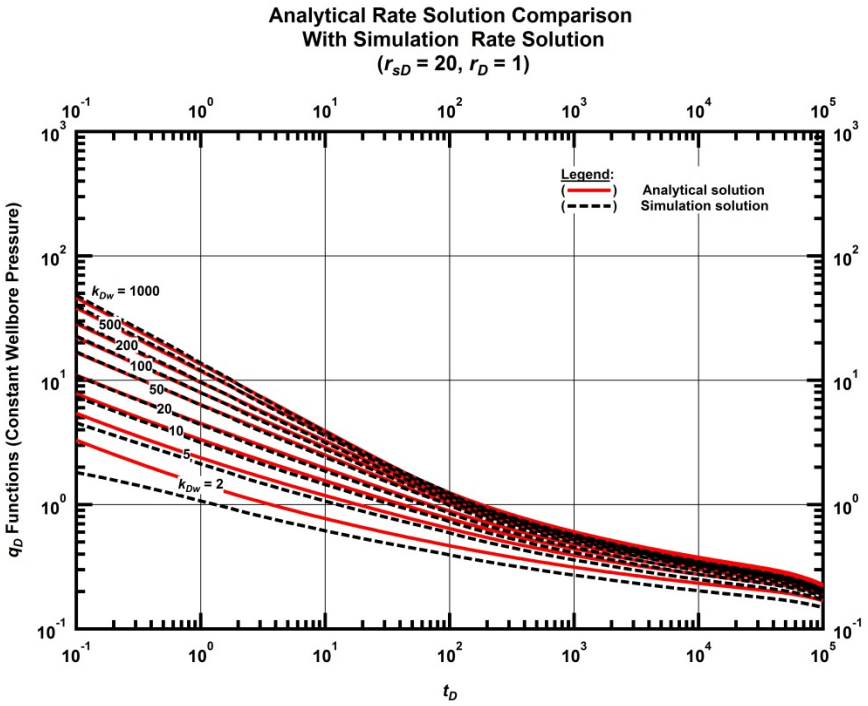

Figure C.35 — Log-log plot comparing the analytic rate solution to numerical rate solution for a reservoir with $r_{sD}=20$ at $r_D=1$.